Hamiltonian formulation of Villain models

LUCCA FAZZA MARCON

FAZZA MARCON, LUCCA (2025) Hamiltonian formulation of Villain models. Doctoral thesis, Durham University.

Hamiltonian formulation of Villain models

Lucca Fazza Marcon

A Thesis presented for the degree of
Doctor of Philosophy

Department of Mathematical Sciences
Durham University
United Kingdom

December 2025

Hamiltonian formulation of Villain models

Lucca Fazza Marcon

Submitted for the degree of Doctor of Philosophy

December 2025

Abstract: Lattice formulations provide essential non-perturbative access to strongly coupled QFTs but often break fundamental continuum symmetries. This violation, particularly concerning topological currents, introduces unphysical artifacts like dynamical vortices or monopoles. This work employs the Villain Hamiltonian framework—using integer-valued auxiliary fields—to systematically restore these symmetries in lattice compact scalar and gauge theories. We apply this to compact U(1) gauge theories in 2D and 3D, demonstrating its ability to enforce microscopic Gauss's law, eliminate spurious topological defects, and replicate continuum symmetry structures. In 3D, the framework yields a natural operator-level electric-magnetic duality. Crucially, we construct fracton-inspired constrained models by coupling compact plaquette variables to higher-form gauge fields, which enforce exact higher-moment conservation laws. A key advance establishes an exact duality between one such fracton model and a transverse-field Ising model with extended interactions. Exploiting this fracton-Ising duality, we perform large-scale Monte Carlo simulations on the dual Ising model to study the fracton model's phase structure. Finite-size scaling provides numerical evidence for a continuous phase transition at a critical coupling, offering new insights into exotic quantum system dynamics. This establishes the Villain Hamiltonian as a powerful tool for capturing topological symmetries and enabling precise lattice studies of confinement, duality, and constrained phenomena.

Declaration

The work in this thesis is based on research carried out in the Department of Mathematical Sciences at Durham University. No part of this thesis has been submitted elsewhere for any degree or qualification.

Acknowledgements

Writing this thesis has been one of the most demanding things I've ever done. There were long periods when I doubted whether I would make it to the end, and I often found myself questioning my abilities and direction. But alongside the challenges, there were also moments of clarity, growth, and quiet determination that kept me moving forward. Finishing this work has been a deeply personal accomplishment, and it would not have been possible without the presence and support of some very important people in my life.

To my partner, Paola Delgado. Your steady support, patience, and belief in me never wavered, even when mine did. You were there through every step of this process, and your presence was a constant reminder of why I kept going. I can't thank you enough.

To my sister, Giulia Marcon. No matter the distance, your presence has always felt close. Our bond is something I carry with me every day, and your strength and care have been a quiet source of inspiration.

To my advisor, Tin Sulejmanpasic. I'm sincerely grateful for your guidance, encouragement, and generosity. Your support went far beyond what I expected, and it made a real difference when I needed it most.

To my friends in Durham, Alistair Chopping, Ryan Cullingham, Richie Dadhley, and Rudolfs Treillis. You made this time not only bearable but enjoyable. I learned a lot from each of you, and the laughs and conversations we shared helped me through more than I can say.

To friendships in distant continents that despite the time, distance, and frequency of contact, remained through. In particular, Rodrigo Gomes Costa, a friend that always grounded down back to earth whenever my mind went off fleeing.

To my therapist Amanda Oliveira. A person of not only utmost professional importance and that not only helped through my duties as a PhD student, but also as a person, for the past 4 years. Without you, it is unlikely that any of this and much more, could ever be accomplished.

And to my parents, Newton Marcon and Cecilia Fazza. I don't have the words to properly express my gratitude. The sacrifices you've made and the care you've shown over the years are at the foundation of everything I've accomplished. This achievement is not mine alone—it belongs to you as well.

I looked up at the mass of signs and stars in the night sky and laid myself open for the first time to the benign indifference of the world.

— from *The Stranger* by Albert Camus

Dedicated to

Paola

Contents

List of Figures

Chapter 1

Introduction

Field Theories (QFTs) are the foundational framework for describing the fundamental interactions of nature. Formulated in the continuum, they provide precise and predictive descriptions of a wide range of phenomena, particularly in the weak-coupling regime where perturbative techniques apply. However, many important physical systems, such as those exhibiting confinement in Quantum Chromodynamics (QCD) or topological phases in condensed matter, lie beyond the reach of perturbation theory. To study these strongly coupled systems, a non-perturbative approach is necessary. Lattice regularization offers a viable framework: by discretizing space-time, one defines well-posed path integrals amenable to numerical techniques such as Monte Carlo simulations, which play a central role in this thesis.

Despite its power, the lattice formulation is not without limitations. Most notably, it can fail to preserve key symmetries present in the continuum theory. A prominent example is chiral symmetry: the Nielsen–Ninomiya theorem [1] demonstrates that lattice theories with local, translationally invariant interactions and chiral symmetry suffer from fermion doubling, complicating the construction of chiral gauge theories. Supersymmetry is similarly difficult to realize exactly on the lattice [2].

Symmetry breaking issues are not confined to fermionic or supersymmetric theories. Even in simpler bosonic theories, such as those involving compact scalar fields or abelian gauge fields, the standard lattice formulations may fail to capture the full global symmetry structure of their continuum counterparts. Consider the 2D XY model, defined by the action

$$S = -J \sum_{\langle x,y \rangle} \cos(\phi_x - \phi_y), \tag{1.0.1}$$

where ϕ_x are angular variables and $\langle x, y \rangle$ denotes nearest-neighbor sites. In the continuum, this model corresponds to a compact free scalar field with Lagrangian $\mathcal{L} = \frac{J}{2}(\partial_\mu \phi)^2$, and both share a global $U(1)$ shift symmetry.

The distinction lies in a second topological symmetry of the continuum theory. The standard $U(1)$ shift symmetry is a rigid transformation, $\phi \to \phi + \alpha$, with a constant parameter α. However, the continuum also possesses a *winding symmetry*, associated with the identically conserved topological current $j^T_\mu = \frac{1}{2\pi}\epsilon_{\mu\nu}\partial^\nu \phi$. This symmetry corresponds to more general shifts that change the field's winding number. The lattice model fails to preserve this specific topological symmetry. This violation manifests as the emergence of dynamical vortices, topological defects absent in the free scalar theory, that lead to a phase transition as J is lowered.

An analogous issue arises in pure $U(1)$ gauge theories. In the continuum, the field strength $F_{\mu\nu} = \partial_\mu A_\nu - \partial_\nu A_\mu$ satisfies the Bianchi identity, implying the conservation of the topological current

$$J^T_{\mu\nu} = \frac{1}{2\pi}\epsilon_{\mu\nu\rho\sigma}F^{\rho\sigma}, \tag{1.0.2}$$

which reflects a global topological symmetry. On the lattice, however, the gauge field is discretized through link variables A_l defined modulo 2π, and the field strength is encoded via periodic functions such as $\cos((dA)_l)$. This construction breaks the Bianchi identity, not because $d^2 \neq 0$, but because the discretized and compactified nature of the lattice gauge field modifies the field strength away from the exact differential form $F = dA$, replacing it with periodic functions such as $\cos((dA)_p)$, for which the identity $dF = 0$, guaranteed in the continuum by the exactness of F, no longer applies. This modification permits nontrivial topological configurations, specifically dynamical monopoles that act as sources or sinks of magnetic flux, thereby violating the conservation of the topological current. These monopoles are point-like in three dimensions and form closed loops in four dimensions, and their presence obstructs a faithful realization of the continuum's global structure.

Such symmetry violations are not mere technical artifacts—they reveal a deeper limitation of standard discretization schemes. While infrared behavior may be correctly captured in specific regimes, essential global features that govern the full dynamics can be lost. To address this, improved formulations such as the modified Villain approach have been developed. By introducing integer-valued auxiliary fields, these constructions can restore certain symmetries that are absent in naive discretizations. In the scalar case, promoting field differences to $(d\phi)_l + 2\pi n_l$ with $n_l \in \mathbb{Z}$ allows the winding current to be recovered, as long as n_l is constrained. For abelian gauge theories, similar modifications replace $\cos((dA)_p)$ with expressions involving $(dA)_p + 2\pi n_p$, where n_p is an integer plaquette variable, establishing a topologically protected conservation law and excluding monopole degrees of freedom.

In this thesis, we apply the Villain Hamiltonian formalism to a variety of systems where the restoration of global symmetries plays a crucial role. We begin by studying compact $U(1)$ gauge theories in two and three spatial dimensions, using integer-valued plaquette variables and their conjugate compact fields to enforce Gauss's law at the microscopic level and eliminate unphysical monopole defects. In two dimensions, this formulation reproduces the correct continuum symmetry structure and yields a well-defined non-perturbative model. In three dimensions, the formalism naturally exhibits electric–magnetic duality: the plaquette variables map onto dual compact fields, and a corresponding Gauss constraint is realized for the magnetic sector. This provides a clean Hamiltonian-level realization of duality and a concrete framework for studying topological features of gauge dynamics.

The framework is then extended to exotic systems inspired by fracton physics, where excitations are constrained by subsystem symmetries and conservation laws. By coupling compact scalar fields on plaquettes to higher-form gauge fields, we construct a modified XY-plaquette model that incorporates exact winding symmetries, enforcing the conservation of higher-moment charges. Introducing an additional symmetric tensor gauge field, we obtain a further generalization which exhibits an exact duality to a transverse-field Ising model with nearest- and next-nearest-neighbor couplings. This dual mapping not only provides analytical insight into the phase structure of the fracton-like system but also connects it to a well-understood class of quantum spin models.

Leveraging this duality, we carry out Monte Carlo simulations of the dual Ising model to study the critical behavior of the underlying fracton-inspired theory. Finite-size scaling analysis confirms the presence of a second-order phase transition at coupling constant $g = 0.5$, supporting our conjecture regarding the model's phase structure. These numerical results offer robust, non-perturbative validation of the duality and provide new insight into the emergent phenomena in constrained quantum systems.

The thesis is organized as follows: we start discussing the preliminaries, i.e. all the underlying theoretical tools needed to perform the analysis used in later chapters. We start discussing naive discretizations of scalar theories, introduce the Villain formulation as an alternative discretization framework, explain the Monte Carlo methods and the error analysis necessary to its correct evaluation. We also show fundamental concepts in finite size scaling which is also important for the analysis and interpretation of later results. Finally, we move to exploring and understanding $U(1)$ gauge theories on the lattice with the modified Villain formulation, specifically studying such theories in 2 and 3 dimensions and exotic theories in 3 dimensions. Further, we perform and expose the results of Monte Carlo simulations of models previously obtained and show novel important results regarding their critical behaviour. Finally, we summarize our work while also looking at possible future venues of expanding the work and understanding the limitations of our results in a conclusion chapter.

Chapter 2

Preliminaries

2.1 Lattice theory

2.1.1 Discretization of scalar fields

Discretizing the free massless scalar field provides a simple yet instructive starting point for understanding quantum field theories on a lattice. This step is essential not only for regularizing the theory—i.e., introducing a well-defined path integral by removing ultraviolet divergences—but also for illustrating how the continuum properties of a field theory are affected by discretization. In particular, issues such as the preservation of symmetries, the approach to the continuum limit, and the formulation of alternative discretizations like the Villain action all emerge naturally in this setting.

We consider a real, massless scalar field $\phi(x)$ defined in two-dimensional Euclidean space [3], with action:

$$S[\phi] = \frac{1}{2} \int d^2x \, (\partial_\mu \phi)^2. \tag{2.1.1}$$

To place this theory on a lattice, we replace the continuous space-time coordinates x by a discrete set of N points spaced by a lattice constant a, such that the total extent of the system is $L = aN$:

$$x \to x_n = na, \quad n = 0, 1, \ldots, N-1. \tag{2.1.2}$$

Accordingly, the field $\phi(x)$ is defined only at lattice sites:

$$\phi(x) \to \phi_n. \tag{2.1.3}$$

Derivatives become finite differences between neighboring sites. For a unit vector $\hat{\mu}$ in the μ-th direction, the derivative is approximated as:

$$\partial_\mu \phi(x) \to \frac{\phi_{x+\hat{\mu}} - \phi_x}{a}. \tag{2.1.4}$$

The integral over space-time is replaced by a sum over the lattice, with the measure $d^2x \to a^2 \sum_x$. Substituting these into the action yields the discretized form:

$$S[\phi] = \frac{a^2}{2} \sum_{x=0}^{N-1} \sum_{\mu=0}^{1} \left(\frac{\phi_{x+\hat{\mu}} - \phi_x}{a} \right)^2. \tag{2.1.5}$$

To prepare for alternative formulations like the Villain action, it is helpful to express the dynamics in Hamiltonian form. The Hamiltonian formulation provides a canonical structure, separating spatial and temporal variables, and introduces conjugate momenta π_x for the fields ϕ_x. This is crucial for adapting to alternative discretizations frameworks, such as Villain-type models, which show in later chapters.

In the Hamiltonian framework, time remains continuous while space is discretized. The kinetic term, which depends on time derivatives of the field, becomes:

$$\frac{1}{2} \int dx \, (\partial_0 \phi)^2 \to \sum_{x=0}^{N-1} \frac{a}{2} \dot{\phi}_x^2 = \sum_{x=0}^{N-1} \frac{a}{2} \pi_x^2, \tag{2.1.6}$$

where $\pi_x = \dot{\phi}_x$ is the conjugate momentum at site x. The spatial derivative term becomes the discrete analog of the gradient squared. Altogether, the Hamiltonian reads:

$$H = \sum_{x=1}^{N-1} \left[\frac{a^3}{2} \pi_x^2 + \frac{1}{2a} \left(\phi_{x+\hat{1}} - \phi_x \right)^2 \right]. \tag{2.1.7}$$

This form is particularly well-suited for later generalization. For example, in the Villain approach, one replaces the quadratic potential term by introducing auxiliary integer fields to better capture topological or gauge-invariant structures.

2.1.2 Discretization of gauge fields

Now we want to perform a similar task to what we just did albeit with a pure abelian gauge field theory in Euclidean spacetime,

$$S[A] = \frac{1}{4} \int d^4x F_{\mu\nu} F_{\mu\nu}, \tag{2.1.8}$$

where the field strength tensor, $F_{\mu\nu}$, is written as,

$$F_{\mu\nu} = \partial_\mu A_\nu - \partial_\nu A_\mu. \tag{2.1.9}$$

If one wanted to obtain a discrete version of this action, one could potentially be tempted to try the same approach as previously, and write the gauge fields $A_\mu(x)$ as living on sites x_i of a hypercubic lattice Λ, with spacing a between sites. This would lead $F_{\mu\nu}$ to be defined via finite differences of gauge fields $A_\mu(x)$,

$$F_{\mu\nu}(x) = \frac{1}{a} \left[A_\nu(x + a\hat{\mu}) - A_\nu(x) \right] - \frac{1}{a} \left[A_\mu(x + a\hat{\nu}) - A_\mu(x) \right]. \tag{2.1.10}$$

This expression is, in fact, gauge invariant under linearized (infinitesimal) $U(1)$ gauge transformations of the form $A_\mu(x) \to A_\mu(x) + \partial_\mu \alpha(x)$ in the continuum limit. However, it fails to capture the full non-perturbative gauge invariance required on the lattice, particularly in the compact $U(1)$ theory. This is because the finite differences do not account for the compact nature of the gauge group and can lead to ambiguities under large gauge transformations.

To formulate a gauge-invariant discretization that remains valid beyond the linear regime and includes the compact structure of $U(1)$, we instead promote the gauge fields $A_\mu(x)$ to link variables.

In particular, one introduces link variables [4]

$$U_\mu(x) = e^{iaA_\mu(x)}, \tag{2.1.11}$$

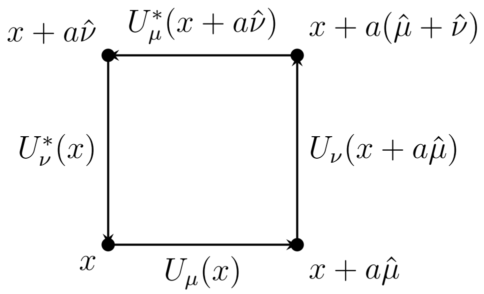

Figure 2.1: Schematic representation of a plaquette

where μ indicates the direction, x is the lattice site from which the link originates, and a is the lattice spacing. Consequently, we create the field strength tensor as a combination of link variables,

$$U_{\mu\nu}(x) = U_\mu(x)U_\nu(x + a\hat{\mu})U_\mu(x + a\hat{\nu})^*U_\nu(x)^*. \tag{2.1.12}$$

this is also called a plaquette, the smallest non-trivial loop of link fields, made of four link variables. A gauge field $A_\mu(x)$ is said to be invariant under $U(1)$ gauge group if,

$$A_\mu(x) \to A_\mu(x)' = A_\mu(x) - \partial_\mu \lambda(x), \tag{2.1.13}$$

where $\lambda(x) \in \mathbb{R}$, and it is clear that $F_{\mu\nu}$ in the continuum is invariant under such transformation. In the lattice however, we introduced the link variables $U_\mu(x)$ and they transform the gauge transformation as [3],

$$U'_\mu(x) = \Omega(x)U_\mu(x)\Omega^*(x + a\hat{\mu}), \tag{2.1.14}$$

where $\Omega(x) = e^{i\alpha(x)} \in U(1)$. We can easily see the gauge invariance of the plaquette by doing the following,

$$U'_{\mu\nu}(x) = U'_\mu(x)U'_\nu(x + a\hat{\mu})U'^*_\mu(x + a\hat{\nu})U'^*_\nu(x) \tag{2.1.15}$$

and using (2.1.14), we get,

$$\begin{aligned} U'_{\mu\nu}(x) = {} & \Omega(x)U_\mu(x)\Omega^*(x + a\hat{\mu})\Omega(x + a\hat{\mu})U_\nu(x + a\hat{\mu})\Omega^*(x + a(\hat{\mu} + \hat{\nu})) \\ & \Omega(x + a(\hat{\mu} + \hat{\nu}))U_\mu^*(x + a\hat{\nu})\Omega^*(x + a\hat{\nu})\Omega(x + a\hat{\nu})U_\nu^*(x)\Omega^*(x) \end{aligned} \tag{2.1.16}$$

and we can see that each gauge transformation of the links cancel each other at each site, resulting in

$$U'_{\mu\nu}(x) = U_\mu(x + a\hat{\nu})U_\nu(x + a\hat{\mu})U^*_\mu(x + a\hat{\nu})U^*_\nu(x), \tag{2.1.17}$$

and we see that the plaquettes are gauge invariant. Writing the plaquette expression (2.1.12) in terms of exponentials of $A_\mu(x)$ we get,

$$U_{\mu\nu}(x) = e^{ia^2 F_{\mu\nu}}. \tag{2.1.18}$$

Taking the real part of this expression allows us to write a lattice version of (2.1.8), known as the Wilson action,

$$S[U] = \beta \sum_x \sum_{\mu<\nu} \left[1 - \text{Re } U_{\mu\nu}(x)\right], \tag{2.1.19}$$

where β is a dimensionless coupling parameter related to the continuum gauge coupling g via $\beta = 1/g^2$. This factor ensures that in the continuum limit $a \to 0$, the lattice action correctly reproduces the standard Yang–Mills action. Expanding the plaquette term,

$$\text{Re } \left[1 - U_{\mu\nu}(x)\right] = 1 - \cos\left(a^2 F_{\mu\nu}(x)\right) \approx \frac{a^4}{2} F^2_{\mu\nu}(x), \tag{2.1.20}$$

we recover (2.1.8). It is important to note that matching the correct continuum limit is necessary but not sufficient. The Wilson action is not only gauge invariant at finite lattice spacing a, but also local, depending only on neighboring links, preserves the correct number of degrees of freedom, and provides a well-defined, non-perturbative regularization of the path integral.

Similarly to the previous section, we now aim to write the Wilson action in a Hamiltonian form. We begin by transitioning to Minkowski spacetime and discretizing space while keeping time continuous. Working in the temporal gauge $U_0(\mathbf{x}, t) = 1$, the dynamical degrees of freedom reduce to the spatial link variables:

$$U_j(\mathbf{x}, t) = e^{iaA_j(\mathbf{x},t)} \quad (j = 1, 2, 3), \tag{2.1.21}$$

where a is the spatial lattice spacing and A_j is the gauge field on the link in the j-th direction.

The Wilson action separates into time-like ($\mu = 0, \nu = j$) and space-like ($\mu = j, \nu = k$) plaquettes:

$$S_M = \frac{1}{2} \int dt \sum_{\mathbf{x}} \left[\sum_j \mathrm{Re}\,(1 - U_{0j}) + \sum_{j<k} \mathrm{Re}\,(1 - U_{jk}) \right]. \tag{2.1.22}$$

To isolate the kinetic and potential terms, we expand the plaquette terms. For time-like plaquettes, the temporal gauge implies

$$U_{0j}(\mathbf{x}, t) = U_j(\mathbf{x}, t + a_0) U_j^\dagger(\mathbf{x}, t) \approx \exp\left(i a a_0 \dot{A}_j(\mathbf{x}, t) \right), \tag{2.1.23}$$

where a_0 is the temporal lattice spacing. Expanding to leading order,

$$\mathrm{Re}\,(1 - U_{0j}) \approx \frac{1}{2} (a a_0 \dot{A}_j)^2. \tag{2.1.24}$$

Summing over all spatial links and taking the continuum limit $a_0 \to 0$, we obtain

$$\sum_{\mathbf{x}} \sum_j \mathrm{Re}(1 - U_{0j}) \approx \frac{1}{2} a^2 a_0^2 \sum_l \dot{A}_l^2, \tag{2.1.25}$$

where the sum is over spatial links l. The kinetic part of the Lagrangian is then

$$\mathcal{L}_{\text{kin}} = \frac{a^2}{4} \sum_l \dot{A}_l^2. \tag{2.1.26}$$

For the spatial plaquettes, we write

$$U_{jk}(\mathbf{x}) = e^{i a^2 F_{jk}}, \quad \text{with} \quad F_{jk} = \partial_j A_k - \partial_k A_j. \tag{2.1.27}$$

Expanding,

$$\mathrm{Re}(1 - U_{jk}) \approx \frac{a^4}{2} F_{jk}^2. \tag{2.1.28}$$

Using the notation of differential co-chains in appendix A,

$$\sum_{\mathbf{x}} \sum_{j<k} \mathrm{Re}(1 - U_{jk}) \approx \frac{a^4}{2} \sum_p F_p^2 = \frac{a^4}{2} \sum_p (dA)_p^2, \tag{2.1.29}$$

where p labels spatial plaquettes. The notation $(dA)_p$ represents the discrete exterior derivative of the gauge field A_l, evaluated on the plaquette p. In the lattice formulation, A_l is defined on links (or edges), while $(dA)_p$ corresponds to the oriented sum of the gauge field around the boundary of plaquette p:

$$(dA)_p = A_{l_1} + A_{l_2} - A_{l_3} - A_{l_4},$$

where $l_1, \ldots, l_4$ are the four links forming the perimeter of plaquette p. The signs arise from the orientation of the plaquette: links whose direction agrees with the chosen circulation (in this case, we choose counterclockwise) contribute with a positive sign, while links opposing it contribute with a negative sign.

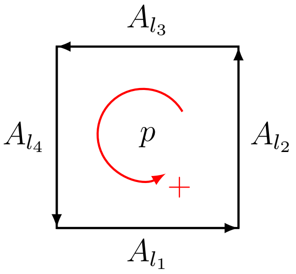

Figure 2.2: Illustration of the plaquette variable $(dA)_p$, defined as the oriented sum of link variables around plaquette p.

The potential part of the Lagrangian is then

$$\mathcal{L}_{\text{pot}} = -\frac{a^4}{4}\sum_p (dA)_p^2. \tag{2.1.30}$$

Combining the kinetic and potential terms, the full Lagrangian becomes

$$\mathcal{L} = \frac{a^2}{4}\sum_l \dot{A}_l^2 - \frac{a^4}{4}\sum_p (dA)_p^2. \tag{2.1.31}$$

From the Wilson action,

$$S[U] = \frac{\beta}{2}\sum_x \sum_{\mu<\nu} \mathrm{Re}\left(1 - U_{\mu\nu}(x)\right), \tag{2.1.32}$$

we obtain the Lagrangian written in terms of temporal and spatial parts,

$$\mathcal{L} = \beta\left(\frac{a^2}{4}\sum_l \dot{A}_l^2 - \frac{a^4}{4}\sum_p (dA)_p^2\right). \tag{2.1.33}$$

The conjugate momentum to A_l is

$$\pi_l = \frac{\partial \mathcal{L}}{\partial \dot{A}_l} = \frac{\beta a^2}{2} \dot{A}_l. \tag{2.1.34}$$

Solving for $\dot{A}_l$ and performing a Legendre transform gives the Hamiltonian:

$$H = \sum_l \frac{1}{2\beta a^2} \pi_l^2 + \frac{\beta}{2a^2} \sum_p (dA)_p^2. \tag{2.1.35}$$

This is the desired Hamiltonian in terms of the conjugate momentum π_l and the field strength encoded by $(dA)_p$.

2.2 Monte Carlo method

Monte Carlo techniques provide a direct way to deal with systems in which the number of possible states grows exponentially with the number of degrees of freedom. It consists on extracting meaningful statements from a small set of configurations compared to overwhelming total number of possible configurations of a certain system. It was first developed by the Stanislav Ulam [5] when confronted with the fact that in order for him to know what was probability of wining in the card game of *Solitaire*, he would have to compute all 52! possible configuration of organizing the set of cards. He realized that one could achieve a very solid estimate of winning if one computed not all possible configurations but a smaller, yet meaningful, subset of those configurations. In other words, if he managed to sample 100 different games, in which the cards were truly shuffled, then with this amount of samples, he could estimate the probability of winning the game. Dubbed after the famous casino, the Monte Carlo method consists in exactly this: a computational technique that uses random sampling to explore a system's possible configurations and estimate statistical properties of said system.

Let's start with a system describe in terms of its statistical partition function,

$$Z = \prod_i \int d\phi_i e^{-S[\phi_i]}, \tag{2.2.1}$$

Where we are labelling the degrees of freedom ϕ with the index i. The weight of each ϕ_i is determined by the action $S[\phi_i]$. If we wanted to measure the value of an observable Q, we would perform the average over all the possible the configurations of the system, such that

$$\langle Q \rangle = \frac{1}{Z} \prod_i \int d\phi_i Q[\phi_i] e^{-S[\phi_i]}. \tag{2.2.2}$$

However, performing this calculation is either extremely impractical or impossible, for most if not all realistic systems. We can instead replace the integral over all possible states by a sum over a finite number of configurations $\phi_{(i)}$, $i = 1, 2, ..., N$. The crux of Monte Carlo lies in randomly selecting these N configurations according to a suitable probability distribution $p[\phi_{(i)}]$, rather than sampling uniformly from the entire configuration space. This leads to an approximation of (2.2.2) in the form

$$\bar{Q} = \frac{\sum_{i=1}^{N} Q[\phi_{(i)}] \frac{e^{-S[\phi_{(i)}]}}{p[\phi_{(i)}]}}{\sum_{i=1}^{N} \frac{e^{-S[\phi_{(i)}]}}{p[\phi_{(i)}]}}, \tag{2.2.3}$$

where $p[\phi_{(i)}]$ is the probability distribution used to generate the configuration $\phi_{(i)}$. As the number of configurations N increases, this estimator becomes increasingly accurate. In the limit $N \to \infty$, we recover the exact expectation value, $\bar{Q} \to \langle Q \rangle$.

Choosing the correct probability distribution is essential for the effectiveness of (2.2.3). The partition function (2.2.1) and expectation value (2.2.2) are primarily influenced by the small number of states with the lowest action values. A good candidate for the probability distribution is the Boltzmann distribution,

$$p[\phi_i] = \frac{1}{Z[\phi]} e^{-S[\phi_i]} \tag{2.2.4}$$

where Z is,

$$Z = \sum_{i=1}^{N} e^{-S[\phi_i]}, \tag{2.2.5}$$

The higher value of the Boltzmann weight, the more influence those states will have on the partition function and expectation value. Biasing the sampling of configurations based on their impact on the system is called ‘importance sampling’ and it is a fundamental aspect of the Monte Carlo method that we employ. Using the Boltzmann factor into (2.2.2), we simplify the result to

$$\bar{Q} = \frac{1}{N}\sum_{i}^{N} Q[\phi_{(i)}], \tag{2.2.6}$$

which is a simple mean of the observables. To explore the system's configuration space, we employ a sequential sampling method guided by the Boltzmann factor. This process generates a sequence of configurations,

$$\phi_{(1)} \to \phi_{(2)} \to ... \to \phi_{(n)} \to \phi_{(n+1)} \to ... \tag{2.2.7}$$

To generate configurations distributed according to the Boltzmann weight $e^{-S[\phi]}$, we employ a Markov chain sampling procedure. This means we construct a sequence of configurations where each new configuration depends only on the previous one. If designed correctly, this Markov chain converges to the target distribution, favoring configurations that have a greater weight in the path integral.

In a Markov chain, the evolution of the system is governed by *transition probabilities*, which define the likelihood of moving from one configuration to another. Formally, the transition probability $P(\phi_{(n)} \to \phi_{(n+1)})$ represents the probability that the system in state $\phi_{(n)}$ at step n will transition to state $\phi_{(n+1)}$ at the next step. These probabilities encode the stochastic dynamics of the chain and determine how configurations are explored during the simulation.

To ensure a well-defined Markov process, the transition probabilities must satisfy the following properties: (i) **Time independence** — the transition probabilities remain constant throughout the evolution; (ii) **Markov property** — the probability of transitioning to $\phi_{(n+1)}$ depends only on the current configuration $\phi_{(n)}$, not on the history of previous states; (iii) **Range** — each transition probability $P(\phi_{(n)} \to \phi_{(n+1)})$ is a real number within the interval $[0, 1]$; and (iv) **Normalization** — for any given configuration $\phi_{(n)}$, the sum of transition probabilities to all possible next states $\phi_{(n+1)}$ equals 1.

For a Markov chain to correctly sample from the target distribution, it must be ergodic, ensuring that all regions of configuration space can be explored. In addition, satisfying the detailed balance condition is often sufficient to guarantee convergence to the desired distribution, although it is not strictly required.

Ergodicity means that it is possible to reach any configuration from any other configuration in a finite number of steps, ensuring that the entire configuration space is eventually explored. Without ergodicity, some regions of the space might remain inaccessible, leading to biased sampling.

Detailed balance ensures that the Markov chain converges to the target distribution—in our case, the Boltzmann distribution. It requires that, at equilibrium, the probability of transitioning from a configuration ϕ to another configuration ϕ' is balanced by the reverse transition. This can be expressed as:

$$\pi(\phi)P(\phi \to \phi') = \pi(\phi')P(\phi' \to \phi), \tag{2.2.8}$$

where $\pi(\phi)$ is the equilibrium probability of configuration ϕ, and $P(\phi \to \phi')$ is the transition probability. This condition ensures that there is no net flow of probability between configurations and that the Markov chain remains in equilibrium once it reaches it.

A widely used method that satisfies detailed balance is the Metropolis–Hastings algorithm [6, 7]. It works as follows:

- Propose a new configuration $\tilde{\phi}$ by making a small random change to the current configuration ϕ.
- Compute the acceptance ratio:

  $$\rho = \frac{p[\tilde{\phi}]}{p[\phi]} \in [0, \infty), \tag{2.2.9}$$

  where $p[\phi]$ is the target probability distribution (i.e., the Boltzmann weight).
- Accept the proposed configuration $\tilde{\phi}$ with probability $\min\{1, \rho\}$. If the move is rejected, keep the current configuration.

By repeating this process, the algorithm generates a sequence of configurations distributed according to $p[\phi]$, satisfying both ergodicity and detailed balance.

The Metropolis-Hastings algorithm isn't the only option of choice for a selection algorithm within Monte Carlo methods. Random-walk, worm, heat-bath, are only a few that can be named [8–13]. The choice of which algorithm to choose should be compatible with the underlying system being simulated. Since we are simulating an Ising model, we will mainly focus on using the Metropolis algorithm, as its simplicity and local update scheme make it particularly well suited for spin systems with nearest-neighbor interactions.

2.3 Statistical and Error analysis

In this section, we discuss how to analyze the data produced by Markov Chain Monte Carlo (MCMC) simulations.

We begin by considering a sequence of measurements $\{Q_1, Q_2, \ldots, Q_N\}$ of an observable Q, obtained from a single MCMC run. These are random variables drawn from a probability distribution governed by the Boltzmann weight. The expectation value of the observable is given by the ensemble average:

$$\langle Q \rangle = \int \mathcal{D}\phi \, Q[\phi] \, p[\phi], \tag{2.3.1}$$

where $p[\phi] \propto e^{-S[\phi]}$ is the target distribution.

In practice, we approximate $\langle Q \rangle$ using the arithmetic mean of the sampled values:

$$\bar{Q} = \frac{1}{N} \sum_{i=1}^{N} Q_i. \tag{2.3.2}$$

If we assume that the Q_i are independent and identically distributed (i.i.d.) random variables with finite variance $\sigma_Q^2 = \langle Q^2 \rangle - \langle Q \rangle^2$, then the expected value of the sample mean $\bar{Q}$ is:

$$\bar{Q} = \langle Q \rangle, \tag{2.3.3}$$

and the variance of $\bar{Q}$ across many independent simulations (i.e., many independent ensembles) is:

$$\sigma_{\bar{Q}}^2 = \langle (\bar{Q} - \langle \bar{Q} \rangle)^2 \rangle = \frac{1}{N}\sigma_Q^2. \tag{2.3.4}$$

Let us now show the steps leading to this result under the i.i.d. assumption. Starting from:

$$\sigma_{\bar{Q}}^2 = \left\langle \left(\frac{1}{N} \sum_{i=1}^{N} (Q_i - \langle Q \rangle) \right)^2 \right\rangle, \tag{2.3.5}$$

we expand the square:

$$\sigma_{\bar{Q}}^2 = \frac{1}{N^2} \sum_{i,j=1}^{N} \langle (Q_i - \langle Q \rangle)(Q_j - \langle Q \rangle) \rangle. \tag{2.3.6}$$

This sum separates into diagonal and off-diagonal terms:

$$\sigma_{\bar{Q}}^2 = \frac{1}{N^2} \left(\sum_{i=1}^{N} \langle (Q_i - \langle Q \rangle)^2 \rangle + \sum_{i \neq j} \langle (Q_i - \langle Q \rangle)(Q_j - \langle Q \rangle) \rangle \right). \tag{2.3.7}$$

If the Q_i are uncorrelated, the cross terms vanish:

$$\langle Q_i Q_j \rangle = \langle Q_i \rangle \langle Q_j \rangle \quad \text{for } i \neq j, \tag{2.3.8}$$

leaving:

$$\sigma_{\bar{Q}}^2 = \frac{1}{N^2} \cdot N \cdot \sigma_Q^2 = \frac{1}{N}\sigma_Q^2. \tag{2.3.9}$$

However, this result relies on the assumption that the measurements Q_i are independent. In the context of MCMC, this is generally not true: the sequence of configurations forms a Markov chain, so consecutive measurements are typically correlated.

These correlations reduce the effective number of independent samples and increase the variance of the sample mean beyond σ_Q^2/N. Therefore, assuming $\langle Q_i Q_j \rangle = \langle Q_i \rangle \langle Q_j \rangle$ for $i \neq j$ is an approximation that only holds in the limit where autocorrelations vanish—that is, when samples are sufficiently far apart in the chain. We will return to the role of autocorrelations in detail later.

The variance of the sample mean, $\sigma_{\bar{Q}}^2$, provides a direct estimate of the statistical uncertainty (or error bar) associated with our Monte Carlo result. To interpret this

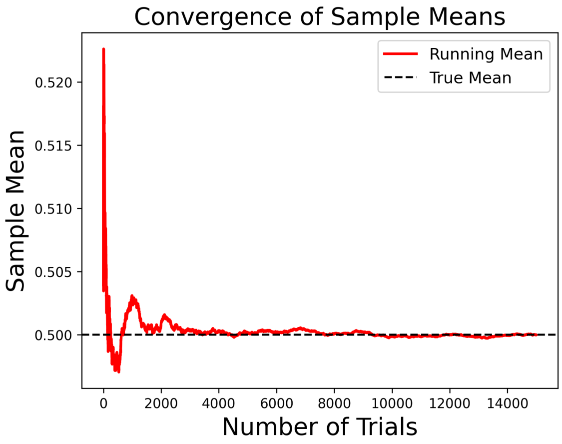

Figure 2.3: Convergence of the value of samples obtained in Monte Carlo. The running mean approaches the true mean of a normal distribution as the number of samples increases.

properly, we must understand how repeated measurements of $\bar{Q}$ fluctuate across many independent runs. This is precisely the setting of the Central Limit Theorem (CLT). The CLT states that, regardless of the underlying distribution of the individual measurements q_i, the distribution of the sample mean $\bar{Q}$ converges to a Gaussian distribution in the limit of large N, provided the samples are uncorrelated. Although a formal proof is accessible and instructive (see, e.g., [14]), we will focus here on the practical implications of the theorem and illustrate them through representative examples.

To illustrate the Central Limit Theorem (CLT) in practice, we implemented a simple Monte Carlo sampling algorithm using a uniform distribution. We generated 15,000 independent estimates of the mean, where each estimate was computed from a sample of 30 uniformly distributed random numbers.

In Fig. 2.3, we show the running average of these Monte Carlo means (red line) compared with the mean of a normal distribution (dashed line). As the number of samples increases, the Monte Carlo average converges toward the expected value, as predicted by the CLT.

In Fig. 2.4, we present a histogram of the 15,000 computed means. The histogram was constructed using 100 bins, which are subintervals dividing the full range of observed values. Each bin counts how many sample means fall within that subinterval,

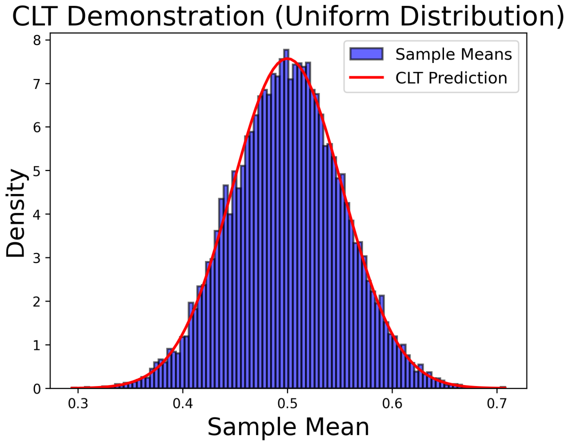

Figure 2.4: Histogram of sample means compared with a Gaussian distribution (in red).

providing a visual approximation of the distribution. Overlaid in red is a Gaussian curve with the same mean and variance. As expected from the CLT, the distribution of sample means closely follows a normal distribution, even though the original data were sampled from a uniform distribution.

The Central Limit Theorem states that, under mild conditions, the distribution of the sample mean $\bar{Q}$ of independent and identically distributed (i.i.d.) random variables q_i approaches a Gaussian as the sample size N increases. If the q_i have finite variance σ_Q^2, then the mean $\bar{Q}$ is normally distributed with mean μ_Q and variance σ_Q^2/N. This result justifies interpreting the standard deviation of the sample mean,

$$\varepsilon_{\bar{Q}} = \sigma_{\bar{Q}} = \frac{\sigma_Q}{\sqrt{N}}, \tag{2.3.10}$$

as the statistical error (or uncertainty) in estimating the expectation value of Q.

In Monte Carlo simulations—and particularly in Markov Chain Monte Carlo (MCMC)—the individual measurements q_i are usually not independent, but correlated due to the nature of the sampling process. Nevertheless, if these correlations decay fast enough (i.e., the Markov chain is ergodic and has a finite autocorrelation time), a generalized version of the CLT still applies. In this case, the variance of the sample mean is larger than σ_Q^2/N and must be corrected to account for these correlations. We now turn to this issue in the next section.

2.3.1 Autocorrelation

The fact is that measurements obtained through Monte Carlo simulations are very unlikely to be statically uncorrelated, specially near the phase transitions. Which means that we result we obtained for errors in the previous section is either wrong or incomplete. In fact we need to take into account what is called the autocorrelation between the measurements, that is, taking into account the neglect term in (2.3.10), resulting in,

$$\sigma_Q^2 = \frac{1}{N}\sigma_Q + \frac{1}{N^2}\sum_{i\neq j}\langle Q_i Q_j\rangle - \langle Q_i\rangle\langle Q_j\rangle. \tag{2.3.11}$$

To simplify things a bit, we are able to perform a few massaging steps on this expression. To do so, we first define the autocorrelation function $A(k)$ as [15],

$$A(k) = \frac{\langle Q_i Q_{i+k}\rangle - \langle Q_i\rangle\langle Q_{i+k}\rangle}{\langle Q_i^2\rangle - \langle Q_i\rangle^2}, \tag{2.3.12}$$

and note that $A(0) = 1$. Let's say a few thing about this expression first. As k increases, $A(k)$ decreases exponentially, and we are allowed to define,

$$A(k) \propto e^{-k/\tau_{Q,\mathrm{exp}}}, \tag{2.3.13}$$

for $k \to \infty$. $\tau_{Q,\mathrm{exp}}$ is called exponential autocorrelation time. Since Markov processes are invariant under time translations, this function is independent of i, thus we can average $A(k)$ over multiple measurements i. The integrated autocorrelation time is defined as,

$$\tau_{Q,\mathrm{int}} = \frac{1}{2} + \sum_{k=1}^{N} A(k)\left(1 - \frac{k}{N}\right). \tag{2.3.14}$$

The term $A(k)$ represents the normalized autocorrelation function. The factor $\left(1 - \frac{k}{N}\right)$ provides a finite-sample correction that reduces bias for limited data. We can also define the error for correlated measurements as,

$$\epsilon = \sqrt{\frac{2\sigma_Q^2}{N}\tau_{Q,\mathrm{int}}}. \tag{2.3.15}$$

In order words, the autocorrelation between measurements decreases the total number of independent measurements we have in our simulation, and increases our estimation of the errors.

This means that, in a Markov process, we need $2\tau_{Q,\text{int}}$ times more measurements to obtain uncorrelated results. To address this, we must either adjust our original expression to account for the autocorrelation time or discard a certain number of Monte Carlo sweeps before recording measurements. Every observable and its derivatives are affected by autocorrelation, leading to systematic under- or over-estimation.

This issue is even more severe near a phase transition, the most interesting regime to study, due to critical slowing down, a computational bottleneck caused by autocorrelation in Monte Carlo simulations. The slowdown is inherently tied to the update algorithm used in the Monte Carlo method: as the system approaches a phase transition, the correlation length ξ diverges as a power law of the distance to the critical point, $\xi \sim |T - T_c|^{-\nu}$. In finite systems, this leads to long-range correlations and dramatically increased equilibration times. Although alternative update strategies, such as cluster algorithms [16, 17], can alleviate this effect, critical slowing down is never entirely eliminated.

Getting back to (2.3.11), we first consider the fact that the expression is invariant under $i \longleftrightarrow j$ and we need only to consider half of the off-diagonal terms,

$$\sigma_{\bar{Q}}^2 = \frac{1}{N}\sigma_Q + \frac{2}{N^2}\sum_{i=1}^{N}\sum_{j=i+1}^{N}\langle Q_i Q_j\rangle - \langle Q_i\rangle\langle Q_j\rangle. \tag{2.3.16}$$

We follow by using the same argument of time translation invariance of Markov process. We can shift the term $\langle Q_i Q_{i+\delta}\rangle$ by any constant δ amount. Fixing $i = 1$ and realizing that the double sum can we rewritten as $\sum_{i=1}^{N}\sum_{j=i+1}^{N} = \sum_{j=2}^{N}$ and changing $l = j - 1$, we get

$$\begin{aligned}\sigma_{\bar{Q}}^2 &= \frac{1}{N}\sigma_Q + \frac{2}{N^2}\sum_{i=1}^{N}\sum_{l=1}^{N}(N-l)\langle Q_1 Q_{l+1}\rangle - \langle Q_1\rangle\langle Q_{l+1}\rangle \\ &= \frac{2\sigma_Q^2}{N}\left[\frac{1}{2} + \sum_{l=1}^{N}\Big(1 - \frac{l}{N}\Big)\frac{\langle Q_1 Q_{l+1}\rangle - \langle Q_1\rangle\langle Q_{l+1}\rangle}{\sigma_Q^2}\right]\end{aligned} \tag{2.3.17}$$

and since $\frac{\langle Q_1 Q_{l+1}\rangle - \langle Q_1\rangle\langle Q_{l+1}\rangle}{\sigma_Q^2} = \frac{\langle Q_1 Q_{l+1}\rangle - \langle Q_1\rangle\langle Q_{l+1}\rangle}{\langle Q_1^2\rangle - \langle Q_1\rangle^2} = A(l)$, we obtain,

$$\sigma_{\bar{Q}}^2 = \frac{2\sigma_Q^2}{N}\left[\frac{1}{2} + \sum_{l=1}^{N} A(l)\left(1 - \frac{l}{N}\right)\right]. \tag{2.3.18}$$

2.4 Fine size scaling theory

In general, a phase transition occurs when a physical system exhibits a non-analytic change in its thermodynamic properties as a control parameter [18], such as temperature or external field, is varied. More specifically, a system can undergo a transition between phases with distinct physical properties, often associated with the spontaneous breaking of a global symmetry. In such cases, the system transitions between a symmetric phase and a symmetry-broken phase as a parameter, such as temperature, crosses a critical value. External fields, such as a magnetic field $h \neq 0$, explicitly break symmetry rather than inducing spontaneous symmetry breaking [19].

A phase transition can often be characterized by an order parameter, a quantity that is zero in the symmetric phase and nonzero in the symmetry-broken phase [20]. For example, in a ferromagnetic system, the magnetization acts as an order parameter: it is zero above the critical temperature (disordered phase) and acquires a nonzero value below it (ordered phase).

Phase transitions can be classified based on the behavior of thermodynamic quantities. A first-order phase transition is characterized by a discontinuity in the first derivatives of the free energy (e.g., latent heat in a liquid-gas transition). A second-order or continuous phase transition, on the other hand, maintains continuity in the first derivatives but exhibits divergences in the second derivatives, such as the heat capacity or susceptibility. This classification is not exhaustive, as there exist transitions that do not fit neatly into this scheme, such as the Berezinskii-Kosterlitz-Thouless (BKT) [21, 22], transition, which is a topological transition characterized by an essential singularity in correlation functions rather than a simple discontinuity in derivatives of the free energy. In the study of phase transitions, the renormalization group (RG)

[23] provides a powerful theoretical framework. The RG approach systematically analyzes how a system's behavior changes across different length scales, particularly useful for continuous phase transitions where long-range correlations emerge. By applying RG techniques, one can identify fixed points that describe critical behavior and universality classes. Some fixed points correspond to critical points governing second-order transitions [24], while others represent stable or unstable phases.

In what follows, we will explore theoretical tools used to study phase transitions and how they provide insight into critical behavior across different physical systems. Finite-size scaling, in particular, will help explain the nature of different phases and the mechanisms driving the transitions between them.

2.4.1 Second order Phase Transition

A phase transition is characterized when a parameter A [25], i.e. temperature, reaches a specific value, a critical point, when all the phases of the system exist simultaneously. We denote this point as A_c and we can define the reduced critical point as,

$$a = \frac{A - A_c}{A_c} \tag{2.4.1}$$

which shows the relative distance to the phase transition. As mentioned before, during second order phase transitions, the correlation length ξ becomes a power law when $A \to A_c$ (and thus $a \to 0$) [24],

$$\xi \sim |a|^{-\nu}, \tag{2.4.2}$$

where ν is a critical exponent. This is a very important quantity that describes the behavior of the system when near the phase transition, along with other critical exponents. If two different theories belong to the same universality class, their critical exponents will be identical. This means that as they approach their respective critical temperatures (T_c), their long-distance behavior becomes increasingly similar and is described by the same scaling laws, even if their underlying Lagrangians (and/or

Hamiltonians) descriptions are fundamentally different. The exponent ν is but one of the critical exponents and it describes the correlation length ξ near the critical point. Other important critical exponents are β, α, γ, and ψ, each of which characterizes a different aspect of the phase transition [18]. In the case of the Ising universality class, the exponent β governs the behavior of the spontaneous magnetization M as the temperature approaches the critical temperature A_c from below. Specifically, near the critical point, the magnetization behaves as

$$M(A) \sim |a|^{\beta}, \quad \text{for } A < A_c. \tag{2.4.3}$$

By convention, all critical exponents are defined to be positive, reflecting the fact that the associated quantities either vanish or diverge in a controlled way near criticality. The exponent γ describes the divergence of the magnetic susceptibility χ as the system approaches A_c, and is defined through the scaling relation

$$\chi(A) \sim |a|^{-\gamma}. \tag{2.4.4}$$

Each of these exponents encodes universal information about the phase transition and plays a central role in finite-size scaling analysis.

During second-order phase transitions, finite-size scaling theory [26] is based on the comparison between the system size L and the correlation length ξ. When $\xi \ll L$, the system is largely unaffected by its boundaries and behaves effectively as infinite. In contrast, when $\xi \gtrsim L$, finite-size effects become dominant. In this regime, the system size L replaces ξ as the relevant length scale controlling the scaling of observables, and a finite system can no longer reproduce the true singular behavior of the infinite system.

Let us now introduce the finite-size scaling hypothesis, following the framework presented in [27]. We begin by considering the free energy density f, which depends on the system's linear size L, a reduced parameter a (defined in Eq. 2.4.1), and an additional parameter b related to the external field or another control parameter. Thus, we write $f = f(a, b, L)$. The free energy density can be decomposed into a singular and a non-singular part:

$$f(a,b,L) = f_s(a,b,L) + f_{ns}(a,L). \tag{2.4.5}$$

Here, the non-singular part $f_{ns}(a,L)$ is assumed to be weakly dependent on b and is often approximated as independent of it. Moreover, when periodic boundary conditions are imposed—which is the case in all simulations discussed later—we can approximate $f_{ns}(a,L) \approx f_{ns}(a,\infty)$, as boundary contributions become negligible in the thermodynamic limit [28]. If non-periodic boundary conditions were used, additional finite-size contributions could arise from f_{ns}. The functional form of the singular part of the free energy density is not derived but postulated based on scaling hypotheses and can be justified more rigorously via renormalization group arguments. It takes the form:

$$f_s(a,b,L) = L^{-d}\mathcal{F}(c_1 a L^{1/\nu}, c_2 b L^{(\beta+\gamma)/\nu}), \tag{2.4.6}$$

where $\mathcal{F}$ is a universal scaling function, and c_1, c_2 are non-universal metric factors. The argument $aL^{1/\nu}$ arises from the scaling of the reduced temperature a with the correlation length exponent ν. The second argument, $bL^{(\beta+\gamma)/\nu}$, combines the effects of the external field (or similar variable) and reflects how quantities like magnetization (β) and susceptibility (γ) scale near the critical point. Higher-order corrections to scaling are neglected in this leading-order expression. This choice is well-suited to our analysis, though it may not be applicable in other contexts. The finite-size scaling forms of thermodynamic observables can be derived from the singular part of the free energy density in equation(2.4.6). These observables include the *specific heat* C, the *order parameter* O (e.g., the magnetization), and the associated *susceptibility* χ_O. Their scaling behavior near the critical point is governed by critical exponents and takes the form:

$$\begin{aligned} C(L,a) &\sim L^{\alpha/\nu}\,\mathcal{C}(aL^{1/\nu}), \\ O(L,a) &\sim L^{-\beta/\nu}\,\mathcal{O}(aL^{1/\nu}), \\ \chi_O(L,a) &\sim L^{\gamma/\nu}\,\mathcal{X}(aL^{1/\nu}), \end{aligned} \tag{2.4.7}$$

where $\mathcal{C}$, $\mathcal{O}$, and $\mathcal{X}$ are universal scaling functions, and a is the reduced parameter defined in equation (2.4.1). These forms arise from the assumption that the leading singular behavior of each observable is determined by appropriate derivatives of the singular part of the free energy. For instance, the susceptibility χ_O is related to the second derivative of f_s with respect to an external field conjugate to O, while C comes from temperature derivatives.

In addition, there exist scaling relations that connect the critical exponents. Two particularly important ones are:

$$\begin{aligned} \nu d &= 2-\alpha, \\ \alpha+2\beta+\gamma &= 2, \end{aligned} \tag{2.4.8}$$

where the first is known as the *hyperscaling relation.* These constraints imply that only two of the exponents $(\alpha,\beta,\gamma,\nu)$ are independent; once any two are known, the others can be determined.

The finite-size scaling (FSS) method allows one to extract critical exponents by analyzing how observables behave near the critical point in systems of finite size. The key idea is that, close to the critical temperature, the correlation length ξ becomes comparable to the linear system size L, and the finite volume limits the growth of long-range correlations. This cutoff modifies the critical behavior and allows one to infer universal properties from finite systems.

Let us focus on the susceptibility χ_O associated with some order parameter O. Near the critical point in the thermodynamic limit, the correlation length diverges as

$$\xi \sim a^{-\nu}, \tag{2.4.9}$$

where a is the reduced temperature, and the susceptibility scales as

$$\chi_O \sim \xi^{\gamma/\nu}. \tag{2.4.10}$$

However, in a finite system of size L, the divergence of ξ is cut off by L itself. When $\xi \gtrsim L$, the system cannot fully develop long-range correlations, and the susceptibility no longer follows the thermodynamic limit scaling. This motivates introducing a finite-size scaling form for χ_O:

$$\chi_O(a, L) = L^{\gamma/\nu}\, \mathcal{X}(aL^{1/\nu}), \tag{2.4.11}$$

where $\mathcal{X}$ is a universal scaling function. This expression tells us how χ_O varies with both temperature and system size in the vicinity of the critical point.

An important consequence of Eq. (2.4.11) is that if we plot $L^{-\gamma/\nu}\chi_O$ as a function of the scaling variable $x = aL^{1/\nu}$ for different values of L, all curves should collapse onto the same universal function $\mathcal{X}(x)$, provided that the correct values of γ, ν, and the critical point are used. This is known as *data collapse* and serves both as a practical tool for determining critical exponents and as a consistency check to confirm the existence of a second-order phase transition [29].

We will use this collapse property as a diagnostic to validate our simulation results and extract critical parameters. In particular, by tuning the exponents and the critical coupling A_c to maximize the overlap of curves for different system sizes, we can estimate the universal behavior of the system from finite-size data.

There is more than one way to determine the transition point, and one these ways is through the 4th order Binder Cumulant [27],

$$U_4 = 1 - \frac{\langle O^4 \rangle}{3\langle O^2 \rangle^2}. \tag{2.4.12}$$

where O is the observable that we obtained (in our case, it will be mainly magnetization M). This quantity can directly show the transition point for the system, through the crossing of multiple curves, since, at such point, the binder cumulant is also size-independent and all curves should collapse on said point, giving us an estimate of critical value.

2.4.2 First order Phase Transition

Another interesting and important category if phase transitions is the first order phase transition [30], which we discuss now.

First-order phase transitions are characterized by discontinuities in the first derivatives of the partition function. At the critical value A_c, the order parameter and energy density exhibit a finite jump, and two phases coexist. Unlike second-order phase transitions, first-order transitions do not exhibit a diverging correlation length, nor do they have a critical region governed by power laws. As a result, there are no critical exponents and no critical slowing down in the traditional sense.

However, Monte Carlo simulations of first-order phase transitions still suffer from significant autocorrelation [28], though for different reasons. Instead of critical slowing down, the dominant issue is phase coexistence, which leads to long-lived metastable states. In simulations, this manifests as the system getting "stuck" in one phase for an extended time before transitioning to the other, increasing autocorrelation times. Additionally, at the transition, observables scale with the system volume [31], reflecting the extensive nature of the latent heat and phase separation,

$$\chi_O \propto V, \tag{2.4.13}$$

where $V = L^d$. However, in finite systems, the sharp discontinuities expected in the thermodynamic limit are smoothed out. Instead of a true jump, Monte Carlo simulations will only detect a pronounced peak in the observables, which grows proportionally to the system volume. Unlike second-order phase transitions, where observables exhibit universal scaling behavior, first-order transitions lack such universality. This difference in scaling properties provides a key way to distinguish between first- and second-order transitions in numerical simulations.

We can use the Binder Cumulant (2.4.12) to investigate the first order transition, according to what we mentioned above. U_4 should vanish during the disordered phase and approach 2/3 in the ordered phase, and at transition point, a minimum should be visible, that scales with

$$U_4 \propto -V, \tag{2.4.14}$$

However, the location of this minimum does not necessarily coincide with the true transition point. Instead, it tends to shift away from the critical point, defining a ‘pseudo’ transition point $A_0(V)$ that scales with the system size. We can then perform a fit, that allows us to estimate the transition point as [32],

$$A_0(V) \approx A_0 + cV^{-1}, \tag{2.4.15}$$

where we neglect higher order corrections, and c is some fitting constant.

Chapter 3

Quantum Villain Hamiltonians

3.1 Introduction

The preceding chapters established the foundations of lattice field theories using the Wilson formulation. This chapter transitions to the *Villain formulation*, a powerful alternative that offers a more faithful and analytically tractable lattice regularization for theories with compact fields and gauge symmetries. The central achievement reported here is the systematic construction and analysis of *quantum Hamiltonians* for a range of theories using this approach, uncovering their deep structural properties.

We begin by demonstrating the advantages of the Villain formulation for the compact scalar field, where it naturally incorporates topological sectors (winding modes) and leads to an exact solution, including the emergence of self-duality. This framework is then extended to $U(1)$ gauge theories in two and three spatial dimensions. A key original contribution is the explicit derivation of the Hamiltonian self-duality in 2D and the electric-magnetic duality in 3D directly within the operator formalism, a perspective that is less common than the Euclidean path integral approach.

The chapter's primary originality lies in its application of this methodology to "exotic" theories with subsystem symmetries, specifically the quantum XY-plaquette model.

We derive its self-duality and, by gauging its subsystem symmetry and taking a strong-coupling limit, establish a novel duality to a transverse-field J_1-J_2 Ising model. This new lattice model features a highly degenerate ground state and a complex phase diagram, setting the stage for future numerical investigation of its phase transitions. Throughout, the work emphasizes the power of the Villain Hamiltonian approach to reveal exact dualities, topological constraints, and unconventional symmetries.

3.2 Compact Free Scalar

Now let's consider that the field $\phi(x)$ from the Hamiltonian (2.1.7) is invariant under $\phi(x) \to \phi(x) + 2\pi$ [33]. The discretization performed does not satisfy this property. Instead, we change the finite difference such that it takes into account the compactness of $\phi(x)$. The traditional modification is to use a cosine function,

$$(\phi_{x+\hat{\mu}} - \phi_x) \to \cos(\phi_{x+\hat{\mu}} - \phi_x), \tag{3.2.1}$$

which respects the periodicity of $\phi(x)$. The action then takes the form,

$$S[\phi] = -\beta \sum_{x,\mu} \cos(\phi_{x+\hat{\mu}} - \phi_x). \tag{3.2.2}$$

where the minus sign ensures that the action is minimized when neighboring field values are similar, thus favoring smooth configurations. The parameter β is a dimensionless coupling constant. In the statistical mechanics interpretation, β plays the role of an inverse temperature. In the spacetime interpretation, however, β is related to the bare coupling constant and controls the stiffness of the field; large β favors small gradients and hence smoother field configurations. This formulation allows for a meaningful continuum limit as $\beta \to \infty$. This is the known lattice regularization of the compact free scalar through the XY-plaquette model [34]. Looking at a single link of the Boltzmann weight,

$$e^{\beta \cos\left(\phi_{x+\hat{\mu}} - \phi_x\right)} \tag{3.2.3}$$

At large coupling β, the cosine interaction is sharply peaked around its infinite set of minima at $\phi_{x+\hat{\mu}} - \phi_x = 2\pi m_x$. A naive approximation replaces the cosine by its quadratic expansion near a central single minimum of $m_x = 0$. This yields a Gaussian action describing a non-compact free scalar field,

$$e^{-\beta\cos\left(\phi_{x+\hat{\mu}}-\phi_x\right)} \approx e^{-\frac{\beta}{2}\left(\phi_{x+\hat{\mu}}-\phi_x\right)^2} \tag{3.2.4}$$

This approximation is only valid for small field differences and neglects the periodicity of the original compact field. Consequently it fails to capture phenomena like vortex excitations and winding sectors. To address these limitations, an alternative regularization is introduced: the Villain formulation [35]. The Villain action replaces the cosine term with a periodic Gaussian potential,

$$S_{\text{Villain}}[\phi] = -\frac{\beta}{2}\sum_{x,\mu}\left(\phi_{x+\hat{\mu}} - \phi_x - 2\pi n_{x,\mu}\right)^2, \qquad n_{x,\mu} \in \mathbb{Z}. \tag{3.2.5}$$

The Villain formulation provides the correct continuum limit when the infinite set of minima of the cosine potential is properly taken into account. As such, the Villain action offers several advantages: it facilitates analytical progress via Poisson resummation and duality transformations and provides a natural framework for describing vortices [36–39]. Importantly, the Villain action reproduces the Gaussian theory for a compact scalar in the appropriate regime, while also enabling a controlled analysis of topological excitations that the Wilson formulation tends to obscure. However, for compact scalars, a well-defined continuum limit is not always guaranteed, due to the nontrivial role of these topological defects, particularly in two dimensions. In this sense, the Villain action provides a more faithful lattice regularization of the continuum compact free scalar field.

Villain Formulation

Villain approach consist in creating a periodic Gaussian approximation [35]. By substituting the cosine function by a $2\pi n$ sum, take into account all minima of the system, rather than prioritizing a central minimum. This formulation can be modified by promoting the integer-valued variables to quantum operators with integer spectra. In this formalism, one can impose gauge constraints that provide control over the topological defects, such as vortices or monopoles, that are typically present in the standard formulation.

Let's look at how the Villain formulation improves the analysis of the XY-model by looking at the Hamiltonian of a free massless scalar that we will regularize through the Villain Approach. Its Hamiltonian is,

$$H = \sum_x \left(\frac{1}{2Ja} \pi_x^2 + \frac{J}{2a} \left(\phi_{x+1} - \phi_x \right)^2 \right), \tag{3.2.6}$$

where x denotes the lattice site, J is dimensionless and a has dimensions of length. The discrete scalar and its conjugate momenta π_x satisfies the usual commutation rules,

$$[\phi_x, \pi_y] = i\delta_{xy}. \tag{3.2.7}$$

We can make ϕ_x a compact scalar if we modify the Hamiltonian to include a 'integer-valued' operator n_x, i.e. an operator that has integer eigenvalues. Hamiltonian (3.2.6) then takes the form,

$$H = \sum_x \left(\frac{1}{2Ja} \pi_x^2 + \frac{J}{2a} \left(\phi_{x+1} - \phi_x - 2\pi n_x \right)^2 \right), \tag{3.2.8}$$

To this operator we naturally associate an angle-valued operator $\tilde{\phi}_x$. They commute according to,

$$\left[\tilde{\phi}_x, n_y \right] = i\delta_{xy}, \tag{3.2.9}$$

while commuting with the other operators, $[\phi_x, n_y] = [\pi_x, n_y] = \left[\tilde{\phi}_x, \phi_y \right] = 0$. Moreover, we expect $\tilde{\phi}_x$ to shift by 2π such as,

$$e^{i2\pi n_x} \tilde{\phi}_x e^{-i2\pi n_x} = \tilde{\phi}_x + 2\pi. \tag{3.2.10}$$

and since this is supposed to be a gauge symmetry of the theory, the Hilbert space must be invariant under the action of $e^{i2\pi n_x}$. This operator also needs to commute with the Hamiltonian itself, which follows naturally, since we assumed that $\tilde{\phi}_x$

commutes with π_x and ϕ_x.

We want to show that the Hamiltonian remains unchanged if ϕ_x is shifted by $2\pi k_x$ where k_x is an integer. We start by proposing a naive operator $e^{i2\pi\sum_x k_x\pi_x}$ acting on Hamiltonian (3.2.8),

$$e^{i2\pi\sum_x k_x\pi_x} H e^{-i2\pi\sum_x k_x\pi_x} = \sum_x \left(\frac{1}{2Ja}\pi_x^2 + \frac{J}{2a}\left(\phi_{x+1} - \phi_x + 2\pi\left(k_{x+1} - k_x + n_x\right)\right)^2\right), \tag{3.2.11}$$

which clearly is not invariant under its action. To remedy that, we shift $n_x \to n_x - (k_{x+1} - k_x)$ using the operator $e^{i\sum_x \tilde{\phi}_x(k_{x+1}-k_x)}$. So, in order to shift ϕ_x by multiples of 2π and let H remain invariant, we need to use,

$$e^{i\sum_x\left(2\pi k_x\pi_x + \tilde{\phi}_x(k_{x+1}-k_x)\right)} \tag{3.2.12}$$

To see this, we expand the exponent in

$$e^{i\sum_x\left(2\pi k_x\pi_x + \tilde{\phi}_x(k_{x+1}-k_x)\right)},$$

which gives

$$i\sum_x 2\pi k_x\pi_x + i\sum_x \tilde{\phi}_x\left(k_{x+1} - k_x\right) = i\sum_x\left(2\pi k_x\pi_x + \tilde{\phi}_x k_{x+1} - \tilde{\phi}_x k_x\right).$$

Given that π_x commutes with $\tilde{\phi}_y$, for any x and y, for any arbitrary integer k_x and shifting the summation index in the term containing k_{x+1}, we can write $\sum_x \tilde{\phi}_x k_{x+1} = \sum_x \tilde{\phi}_{x+1} k_x$, so that the whole exponent becomes

$$i\sum_x k_x\left(2\pi\pi_x + \tilde{\phi}_{x+1} - \tilde{\phi}_x\right).$$

And hence, the operator that shifts ϕ_x by $2\pi k_x$ is

$$e^{i\sum_x k_x\left(2\pi\pi_x + \tilde{\phi}_{x+1} - \tilde{\phi}_x\right)} = \mathbb{1}.$$

Note that we required that the operator to be acting trivially on the Hilbert space for any $k_x \in \mathbb{Z}$. This implies that the exponent of (**??**) satisfies,

$$2\pi\pi_x + \tilde{\phi}_{x+1} - \tilde{\phi}_x = 2\pi\tilde{n}_x \tag{3.2.13}$$

where $\tilde{n}_x$ is another operator with an integer-valued spectrum. Expressing it in terms of π_x, we have

$$\pi_x = \frac{1}{2\pi}\left(\tilde{\phi}_x - \tilde{\phi}_{x+1} + 2\pi\tilde{n}_x\right), \tag{3.2.14}$$

which we will use in a moment. In order to keep the commutations relations consistent, first we impose that $[\phi_x, \tilde{n}_y] = i\delta_{x,y}$ and demand that $[\pi_x, n_y] = 0$. This leads to,

$$\begin{aligned}[\pi_x, n_y] &= \frac{1}{2\pi}\left[\left(\tilde{\phi}_x - \tilde{\phi}_{x+1} + 2\pi n_x\right), n_y\right] \\ &= \frac{i}{2\pi}\left(\delta_{x,y} - \delta_{x-1,y}\right) + [\tilde{n}_x, n_y],\end{aligned} \tag{3.2.15}$$

where we used (3.2.14), and since $[\pi_x, n_y] = 0$ we have that,

$$[\tilde{n}_x, n_y] = \frac{i}{2\pi}\left(\delta_{x,y} - \delta_{x-1,y}\right). \tag{3.2.16}$$

If we go back to the Hamiltonian (3.2.8) and rewrite it using (3.2.14), we get

$$H = \sum_x \left(\frac{1}{2Ja(2\pi)^2}\left(\tilde{\phi}_x - \tilde{\phi}_{x+1} + 2\pi\tilde{n}_x\right)^2 + \frac{J}{2a}\left(\phi_{x+1} - \phi_x - 2\pi n_x\right)^2\right), \tag{3.2.17}$$

which satisfies the following commutations relations,

$$[\phi_x, \tilde{n}_y] = i\delta_{x,y}, \tag{3.2.18}$$

$$[\tilde{\phi}_x, n_y] = i\delta_{x,y}, \tag{3.2.19}$$

and

$$[\tilde{n}_x, n_y] = \frac{i}{2\pi}\left(\delta_{x,y} - \delta_{x-1,y}\right) \tag{3.2.20}$$

Moreover, if one applies the following transformations,

$$J \to \frac{1}{(2\pi)^2 J}, \tag{3.2.21}$$

$$\tilde{\phi}_x \to \phi_{x+1}, \qquad \phi_x \to \tilde{\phi}_x, \tag{3.2.22}$$

$$\tilde{n}_x \to n_x, \qquad n_x \to \tilde{n}_{x+1}, \tag{3.2.23}$$

we see that such transformation is the self-duality transformation, meaning that it maps the theory onto itself by interchanging dual variables without changing the coupling of the system. We comment that at $J = 1/(2\pi)$, applying the self-duality transformation yields a symmetry of the system. However, if you perform the transformation twice, you don't get back to the original configuration directly; instead, you end up with a shift (a translation) on the lattice. This means that at this special coupling, self-duality is not just a standalone symmetry, it combines nontrivially with translation, effectively acting as a square root of translation and enhancing the symmetry structure of the theory.

This lattice self-duality is the discrete analogue of Abelian duality in the continuum, where a scalar field theory with coupling J is dual to another theory with coupling $1/(2\pi)^2 J$. In the continuum limit, this correspondence mirrors T-duality in two-dimensional compactified bosonic theories, where momentum and winding modes are exchanged under the transformation $R \leftrightarrow 1/R$. Thus, the mapping $J \to 1/(2\pi)^2 J$ on the lattice captures the same physical idea of interchanging weak and strong coupling regimes while preserving the overall form of the theory.

The system (3.2.17) is completely solved and the steps to it can be found in the appendix (B). Here, we comment its main aspects. Its spectrum is,

$$H = \frac{J(2\pi)^2}{2a} N \left(\frac{\tilde{\Pi}}{N}\right)^2 + \frac{N}{2Ja}\left(\frac{\tilde{\Pi}}{N}\right)^2 + \sum_p \omega_p \left(B_p B_p^\dagger + B_p^\dagger B_p\right). \tag{3.2.24}$$

Where Π is the (conserved) charge due to the global shift symmetry of ϕ_x. Similarly, $\tilde{\Pi}$ is the conserved charge due to the global shift of the $\tilde{\phi}_x$ operator. Moreover, B_p and $B_p^\dagger$ are time-independent operators that act as annihilation and creation, respectively, operators of the harmonic oscillator solution, and satisfy the usual commutation relations,

$$[B_p, B_{p'}^\dagger] = \delta_{pp'}, \qquad [B_p, B_{p'}] = 0. \tag{3.2.25}$$

Also, the sum over p is only over values multiples of $2\pi/N$, such that $p = \frac{2\pi}{N}, \frac{4\pi}{N}, ..., \frac{2(N-1)\pi}{N}$.

Finally, B_p and $B_p^\dagger$ commute as,

$$[B_p, B_{p'}^\dagger] = i\delta_{p,p'}, \tag{3.2.26}$$

and the dispersion relation is,

$$\omega_p^2 = \frac{4\sin^2\left(\frac{p}{2}\right)}{a^2}. \tag{3.2.27}$$

The exact solution serves as a direct lattice counterpart to the continuum compact scalar theory. A key insight is that the zeromode contributions involving Π and $\tilde{\Pi}$ emerge naturally.

3.3 U(1) Gauge theories

3.3.1 Villain Hamiltonian Formulation of Gauge Fields

Having introduced the Wilson action (2.1.19) as a lattice discretization of the Euclidean action of pure $U(1)$ gauge theory, we now turn to an alternative approach: the Villain formulation.

Starting from the Wilson action introduced in equation (2.1.19),

$$S[U] = \frac{1}{2}\sum_x \sum_{\mu<\nu} \mathrm{Re}\left[1 - U_{\mu\nu}(x)\right], \tag{3.3.1}$$

where $U_{\mu\nu}(x)$ is the plaquette variable built from the link fields $U_\mu(x) = e^{iaA_\mu(x)}$.

In the continuum limit, we may write

$$\mathrm{Re}\left[1 - U_{\mu\nu}(x)\right] \approx 1 - \cos\Big(a^2 F_{\mu\nu}(x)\Big). \tag{3.3.2}$$

Thus, the Wilson action takes the approximate form

$$S[U] \approx \frac{1}{2}\sum_x \sum_{\mu<\nu} \Big(1 - \cos\Big(a^2 F_{\mu\nu}(x)\Big)\Big). \tag{3.3.3}$$

This cosine form reflects the compact nature of $U(1)$ and ensures invariance under large gauge transformations. However, it is analytically cumbersome, especially when performing duality transformations or canonical quantization. To facilitate calculations, one can approximate the cosine potential using a sum over periodic Gaussian weights. This approach introduces a parameter β, which controls the sharpness of the potential around its minima and plays the role of an effective coupling. For large β, the identity

$$e^{\beta\cos(\theta)} = \sum_{n\in\mathbb{Z}} e^{-\frac{\beta}{2}(\theta+2\pi n)^2} + (\text{non-leading terms}) \tag{3.3.4}$$

justifies this replacement: the exponential of the cosine is approximated by a sum over Gaussians centered at $\theta = 2\pi n$. The parameter β thus controls both the accuracy of the approximation and the depth of the potential wells. This motivates us to replace

$$\cos\Big(a^2 F_{\mu\nu}(x)\Big) \to \sum_{n_p\in\mathbb{Z}} \exp\left(-\frac{\beta}{2}(a^2 F_{\mu\nu}(x) + 2\pi n_p)^2\right), \tag{3.3.5}$$

where n_p is an integer-valued field living on plaquettes.

Absorbing a^2 into the coupling constant and simplifying the notation, we are led to the Villain action:

$$S_{\text{Villain}} = \frac{\beta}{2}\sum_p \left(F_p + 2\pi n_p\right)^2. \tag{3.3.6}$$

Here, $F_p = (dA)_p$ is the lattice field strength, a discrete curl of the gauge field A_l over plaquette p and $n_p \in \mathbb{Z}$ is the new integer-valued plaquette field. This form retains the 2π periodicity explicitly, since a shift $F_p \to F_p + 2\pi$ can be absorbed into $n_p \to n_p - 1$.

Moreover, the Villain formulation gives finer control over magnetic monopole configurations. The field $B_p = 2\pi n_p$ can be viewed as a discrete background flux, and demanding that $dB = 0$ enforces the absence of magnetic monopoles. In contrast, monopole configurations are automatically present in the Wilson formulation due to the nontrivial winding of the cosine potential, and cannot be turned off or treated independently.

Following the same steps to arrive in (2.1.35), we can write the Hamiltonian formulation of (3.3.6) as,

$$H = \sum_l \frac{\pi_l^2}{2a^2\beta} + \sum_p \frac{\beta}{2a^2}\left((dA)_p + 2\pi n_p\right)^2, \tag{3.3.7}$$

This Villain Hamiltonian naturally lends itself to formulations involving higher-form symmetries [40]. The quantized flux variables are associated with plaquettes (elementary surfaces) rather than links, meaning they couple to a two-dimensional object in the lattice. Consequently, they are interpreted as conserved charges under a 2-form $U(1)$ magnetic symmetry, whose symmetry operators act on surfaces instead of lines. The monopole operators, which shift B_p by 2π, act as charged objects under this symmetry. This provides a powerful framework for analyzing the phase structure of the theory, including confinement and topological order.

3.3.2 U(1) Gauge theories in 2 spatial dimensions

We now turn to the Villain Hamiltonian formulation of $U(1)$ gauge theory in $(2+1)$ dimensions. This case provides a natural next step after the scalar model: it introduces nontrivial gauge dynamics while remaining tractable enough to explore exact symmetry structures and constraints. In particular, we aim to construct a non-perturbative lattice Hamiltonian that preserves both local gauge invariance and the global topological features present in the continuum, such as magnetic flux conservation and the absence of lattice-artefact monopoles, ensured by not including monopole creation terms (e.g. $\cos\phi$) in the Hamiltonian.[1] This formulation will also serve as a stepping stone toward the richer structure of electric-magnetic duality in three spatial dimensions, explored in the next section.

Consider the Hamiltonian of 2d $U(1)$ gauge theory on a lattice Λ,

$$H = \sum_l \frac{\pi_l^2}{2a^2\beta} + \sum_p \frac{\beta}{2a^2}\left((dA)_p + 2\pi n_p\right)^2, \tag{3.3.8}$$

---

[1] In $(3+1)$ dimensions, one can introduce a dynamical monopole matter field explicitly coupled to the gauge sector. In that case, monopoles are not merely lattice artefacts but become genuine excitations carrying magnetic charge, analogous to how electrically charged matter fields couple to the gauge field.

where the gauge fields A_l lives on the spatial links l, and p denotes the plaquettes on the lattice. π_l is the canonical momentum conjugate to A_l and the exterior derivative acts on the gauge field such that,

$$(dA)_p = \sum_{l \in \partial p} A_l, \tag{3.3.9}$$

The Villain operator is also included as n_p and gives the gauge field A_l its compactness feature, $A_l \to A_l + 2\pi k_l$ where k_l is an integer. The system is also subjected to the Gauss's law,

$$(\delta\pi)_x = \sum_{l \in \hat{\partial} p} \pi_l = 0. \tag{3.3.10}$$

In this expression, the symbol $\hat{\partial}$ denotes the boundary operator acting on elements of the *dual lattice*. Specifically, $\hat{\partial} p$ represents the set of dual links l that form the boundary of a dual plaquette p. The asterisk $\star$ denotes the Hodge dual, which maps an object defined on the original lattice to its corresponding dual object (e.g., a plaquette on the primal lattice maps to a site on the dual lattice). Together, these operations allow the divergence condition $(\delta\pi)_x = 0$ to be expressed geometrically as the vanishing of the net flux through the dual links surrounding a dual site, enforcing a local conservation law.

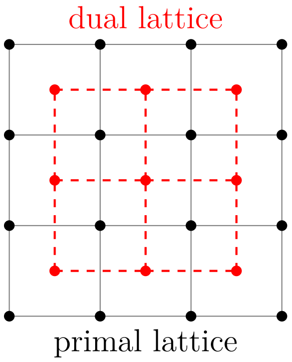

Figure 3.1: Illustration of the primal (black) and dual (red dashed) lattices. Dual lattice sites are centered in the plaquettes of the primal lattice, and dual links intersect primal links orthogonally. The operator $\hat{\partial}$ acts on elements of the dual lattice, while the Hodge dual $*$ maps between corresponding objects on the two lattices.

The system also satisfies two relations, namely

$$\begin{aligned} A_l &\to A_l + 2\pi k_l, \\ n_p &\to n_p - 2\pi (dk)_p, \end{aligned} \tag{3.3.11}$$

and

$$[\phi_{\tilde{x}}, n_p] = i\delta_{\star\tilde{x},p} = i\delta_{\tilde{x},\star p}. \tag{3.3.12}$$

The latter is the commutation relation between the integer valued operator n_p and its conjugate operator $\phi_{\tilde{x}}$, that lives on the dual lattice $\tilde{\Lambda}$. In the former we are only imposing gauge symmetries, and mention that they are generated by the operator $U[k]$, giving by,

$$U[k] = \exp\left(i \sum_l 2\pi\pi_l k_l + i \sum_p (dk)_p \phi_{\star p} \right) = \exp\left(i \sum_l (2\pi\pi_l + (d\phi)_{\star l}) k_l \right). \tag{3.3.13}$$

To show that $U[k]$ generates the gauge symmetry transformation $A_l \to A_l + 2\pi k_l$, we use the BCH formula:

$$U[k] A_l U[k]^{-1} = A_l + i \left[\sum_{l'} \left(2\pi\pi_{l'} + (d\phi)_{\star l'} \right) k_{l'}, A_l \right] + \cdots \tag{3.3.14}$$

Since $[A_l, \pi_{l'}] = i\delta_{ll'}$ and $[A_l, (d\phi)_{\star l'}] = 0$ (as A_l and ϕ are conjugate to n_p and live on different spaces), this simplifies to:

$$U[k] A_l U[k]^{-1} = A_l + 2\pi k_l. \tag{3.3.15}$$

Thus, $U[k]$ implements the desired gauge transformation. The exponential involving $(d\phi)_{\star l}$ ensures that $U[k]$ is gauge-invariant under the dual symmetry generated by the operator $e^{i\phi_{\tilde{x}}}$, enforcing compatibility between the original and dual formulations.

Where in the r.h.s we used the integration by parts rule (A.7). And since every physical state must be invariant under such symmetry, we can obtain the following relation,

$$\pi_l + \frac{(d\phi)_{\star l}}{2\pi} = -m_{\star l}. \tag{3.3.16}$$

The quantity $m_{\star l}$, similarly to n_p is an integer valued operator but lives on the dual lattice links $\tilde{l}$. It acts as conjugate momentum to A_l and satisfies the commutation relation,

$$[m_{\tilde{l}}, A_l] = -i\delta_{l,\star l} = i\delta_{\star l,\tilde{l}} \tag{3.3.17}$$

and we can use (3.3.16) in the first term of (3.3.8), which allows us to rewrite the Hamiltonian as

$$H = \sum_{\tilde{l}} \frac{1}{(2\pi)^2} \left((d\phi)_{\tilde{l}} + 2\pi m_{\tilde{l}}\right)^2 + \sum_{p} \frac{\beta}{2a^2} \Big((dA)_p + 2\pi n_p\Big)^2 \tag{3.3.18}$$

Since n_p commutes with π_l but needs to satisfy (3.3.12), it is fair to take

$$[n_p, (d\phi)_{\tilde{l}} + 2\pi m_{\tilde{l}}] = 0, \tag{3.3.19}$$

and thus,

$$\Big[n_p, m_{\tilde{l}(\tilde{x},\tilde{y})}\Big] = \frac{i}{2\pi} \left(\delta_{\tilde{x},\star p} - \delta_{\tilde{y},\star p}\right), \tag{3.3.20}$$

i.e. n_p satisfy the commutation rule above with an operator $m_{\tilde{l}(\tilde{x},\tilde{y})}$ that lives in a dual link that starts at the dual site $\tilde{x}$ and ends at the dual site $\tilde{y}$. Additionally, the Gauss's law can be written,

$$(dm)_{\tilde{p}} = 0. \tag{3.3.21}$$

This theory is endowed with self-duality. To show that, we perform another a set of transformation, now on the second term of (3.3.8), that is,

$$\Pi_{\tilde{x}} = \frac{1}{2\pi} \left(F_{\star\tilde{x}} + 2\pi n_{\star\tilde{x}}\right), \tag{3.3.22}$$

and note that this operator will act as the conjugate momentum to $\phi_{\tilde{x}}$ and satisfies $[\phi_{\tilde{x}}, \Pi_{\tilde{y}}] = \delta_{\tilde{x},\tilde{y}}$. Furthermore, we note that $\Pi_{\tilde{x}}$ commutes with $m_{\tilde{l}}$. This can be seen as follows,

$$\Big[\Pi_{\tilde{x}}, m_{\tilde{l}(\tilde{z},\tilde{y})}\Big] = \frac{1}{2\pi}\Big[F_{\star\tilde{x}}, m_{\tilde{l}(\tilde{z},\tilde{y})}\Big] + \Big[n_{\star\tilde{x}}, m_{\tilde{l}(\tilde{z},\tilde{y})}\Big] = \frac{1}{2\pi}\Big[F_{\star\tilde{x}}, m_{\tilde{l}(\tilde{z},\tilde{y})}\Big] + \frac{i}{2\pi}\left(\delta_{\tilde{z},\tilde{x}} - \delta_{\tilde{y},\tilde{x}}\right),$$

and,

$$\Big[F_{\star\tilde{x}}, m_{\tilde{l}(\tilde{z},\tilde{y})}\Big] = \sum_{l\in\partial\star\tilde{x}} \Big[A_l, m_{\tilde{l}(\tilde{z},\tilde{y})}\Big] \tag{3.3.23}$$

and taking advantage of the fact that $l \in \partial\star\tilde{x} \equiv \star l \in -\hat{\partial}\tilde{x}$ and that $A_l = -A_{\star(\star l)}$, we get,

$$\left[F_{\star\tilde{x}}, m_{\tilde{l}(\tilde{z},\tilde{y})}\right] = -i \sum_{\tilde{l}'\in\hat{\partial}\tilde{x}} \delta_{\tilde{l}',\tilde{l}(\tilde{x},\tilde{y})} = -i\delta_{\tilde{x},\tilde{y}} + \delta_{\tilde{x},\tilde{z}}, \tag{3.3.24}$$

which results in

$$\left[\Pi_{\tilde{x}}, m_{\tilde{l}(\tilde{z},\tilde{y})}\right] = 0. \tag{3.3.25}$$

With this, we can insert (3.3.22) into (3.3.18), and arrive at

$$H = \sum_{\tilde{x}} \frac{\beta(2\pi)^2}{2}\Pi_{\tilde{x}}^2 + \sum_{\tilde{l}} \frac{1}{\beta(2\pi)^2}\left((d\phi)_{\tilde{l}} + 2\pi m_{\tilde{l}}\right)^2. \tag{3.3.26}$$

which is the Villain Hamiltonian for a compact scalar field defined on the dual lattice. Importantly, there is an additional constraint $d\tilde{n} = 0$, corresponding to a no-vortex condition. The condition $d\tilde{n} = 0$ enforces that the integer-valued field $\tilde{n}$ is locally curl-free on the dual lattice. In geometric terms, $d\tilde{n}$ measures the net circulation of $\tilde{n}$ around an elementary plaquette of the dual lattice. When this quantity vanishes, it implies that there is no topological defects or vortices present in the configuration.

At first glance, this no-vortex constraint may seem unusual. One might consider the Hamiltonian above without imposing it. The integer-valued operator $m_{\tilde{l}}$, defined on dual links, has a natural conjugate momentum that is angle-valued, also residing on the dual links $\tilde{l}$ (or equivalently on the original links l), which we denote by A_l. The constraint $dm = 0$ arises from requiring gauge invariance under transformations $A_l \to A_l + (d\lambda)_l$; in other words, it is a Gauss-law constraint.

Why should we enforce this gauge invariance? It is possible to consider the Villain Hamiltonian for a compact scalar without imposing gauge invariance on the link field A_l. However, the equations of motion for $m_{\tilde{l}}$ are

$$\dot{m}_{\tilde{l}} = 0, \tag{3.3.27}$$

meaning that $m_{\tilde{l}}$ is non-dynamical. Consequently, if a state contains a vortex on a dual plaquette (i.e., $(dm)_{\tilde{p}} \neq 0$), that vortex persists at all times. Thus, the Hilbert space naturally decomposes into superselection sectors labeled by vortex configurations.

One can equivalently impose the no-vortex constraint $(dm)_{\tilde{p}} = 0$, treating other sectors with vortices as arising from temporal Wilson line insertions that select different superselection sectors.

In the continuum, this correspondence mirrors the structure of Abelian duality: the original compact scalar field and the emergent gauge field A_l are dual descriptions of the same degrees of freedom. The constraint $dm = 0$ enforces the absence of monopole (vortex) sources, corresponding to a free "dual photon" in the continuum limit. When this condition is relaxed, monopole events generate a mass for the dual photon, signaling confinement or vortex proliferation in the original scalar description.

3.3.3 U(1) Gauge theories in 3 spatial dimensions

We will now study a 3d $U(1)$ gauge theory and in the same manner as in the last section we will consider some properties, apply some transformation and realise its duality, in this case it is electric-magnetic type duality. First, we consider the Hamiltonian,

$$H = \frac{1}{2\beta}\sum_l (\pi^e_l)^2 + \sum_p \frac{\beta}{2}\left((dA^e)_p + 2\pi n_p\right)^2. \tag{3.3.28}$$

Where e is a superscript to denote electric gauge fields (and their conjugate momenta). m will denote the magnetic gauge fields. Again the Hamiltonian has a Villain variable n_p with an integer spectrum, and its associated with the magnetic gauge field $A^m_{\tilde{l}}$,

$$\left[A^m_{\star p}, n_{p'}\right] = i\delta_{p,p'}. \tag{3.3.29}$$

Such magnetic gauge field is interpreted as the dual gauge field, and we postulate the following gauge invariance,

$$A^m_{\tilde{l}} \rightarrow A^m_{\tilde{l}} + (d\lambda)_{\tilde{l}}, \tag{3.3.30}$$

generated by

$$\exp\left(i\sum_{\tilde{l}} n_{\star l}(d\lambda)_{\tilde{l}}\right) = \exp\left(i\sum_{\tilde{x}}(dn_{\star l})_{\star\tilde{x}}\lambda_{\tilde{x}}\right). \tag{3.3.31}$$

Where the condition $(dn)_c = 0$ is present, following from the gauge invariance of A^m. Because this operator must act as the identity on all physical states of the system, regardless of the choice of $\lambda_{\tilde{x}}$. This requirement enforces the no-monopole constraint, ensuring the conservation of magnetic flux and the validity of the Bianchi identity. While it is possible to consider the insertion of a temporal monopole line operator, doing so requires modifying the constraint to allow for a static monopole located at a dual lattice site $\tilde{x}$.

Before implementing the discrete gauge symmetries, we note that A^e_l satisfies a Gauss's law constraint through $(\delta\pi)_x = 0$. The discrete symmetries are,

$$A^e_l \to A^e_l + 2\pi k_l, \tag{3.3.32}$$

$$n_p \to n_p - (dk)_p, \tag{3.3.33}$$

where the latter is introduced by $\exp\left\{i\sum_l 2\pi k_l \pi_l + i\sum_p (dk)_p A^m_{\star p}\right\}$ that must be an identity operator on the states of the system, thus the following result can be extracted,

$$\pi^e_l = \frac{1}{2\pi}\left(-(dA^m)_{\star l} + 2\pi m_{\star l}\right). \tag{3.3.34}$$

Where $m_{\tilde{p}}$ is an integer-valued operator that lives on the dual lattice plaquettes and it follows that $[A^e_l, m_{\star l'}] = i\delta_{l,l'}$. π^e_l commutes with n_p, and thus, it follows that

$$[\pi^e_l, n_p] = \frac{-1}{2\pi}\left[(dA^m)_{\tilde{p}}, n_p\right] + [m_{\tilde{p}}, n_p] = 0, \tag{3.3.35}$$

since

$$[m_{\tilde{p}}, n_p] = \frac{1}{2\pi}\sum_{\tilde{l}\in\partial\tilde{p}}\left[A^m_{\tilde{l}}, n_p\right] = \frac{1}{2\pi}\sum_{\tilde{l}\in\partial\tilde{p}} i\delta_{\star\tilde{l},p} = \frac{i}{2\pi}L(\partial p, \partial\tilde{p}), \tag{3.3.36}$$

where $L(\partial p, \partial\tilde{p})$ is the linking number between the boundary of plaquettes p and $\tilde{p}$. A discussion regarding $L(\partial p, \partial\tilde{p})$ is reserved to the appendix of [41]. To show that this Hamilton is self-dual, we can define,

$$\pi^m_{\tilde{p}} = \frac{1}{2\pi}\left((dA^e)_{\star\tilde{l}} + 2\pi n_{\star\tilde{l}}\right), \tag{3.3.37}$$

which is the momentum of $A^m_{\tilde{l}}$ and satisfies $\left[A^m_{\tilde{l}}, \pi^m_{\tilde{l}'}\right] = i\delta_{p,p'}$. And it follows that

$\pi^m_{\tilde{l}'}$ commutes with $m_{\tilde{p}}$ and

$$\left[m_{\tilde{p}}, \pi^m_{\tilde{l}}\right] = \frac{1}{2\pi}\left[m_{\tilde{p}}, (dA^e)_{\star\tilde{l}}\right] + \left[m_{\tilde{p}}, n_{\star\tilde{l}}\right]. \tag{3.3.38}$$

And,

$$[m_{\tilde{p}}, (dA^e)_p] = -i\sum_{l\in\partial p}\delta_{\star\tilde{p},l} = -iL(\partial p, \partial\tilde{p}), \tag{3.3.39}$$

and thus $\left[m_{\tilde{p}}, \pi^m_{\tilde{l}}\right] = 0$. Finally, using (3.3.34) and (3.3.37) into (3.3.28) and performing some algebra, with obtain the dual Hamiltonian,

$$H = \sum_{\tilde{l}}\frac{(2\pi)^2\beta}{2}(\pi^m_{\tilde{l}})^2 + \sum_{\tilde{p}}\frac{1}{2\beta(2\pi)^2}\left((dA^m)_{\tilde{p}} + 2\pi m_{\tilde{p}}\right)^2 \tag{3.3.40}$$

Should we consider that Λ is a hypercubic lattice, then we can redefine the operators,

$$\begin{aligned} A'^e_l &= A^m_{g(l)}, \;\; A'^m_{\tilde{l}} = A^e_{g(\tilde{l})}, \\ n'_p &= m_{g(p)}, \;\; m'_{\tilde{p}} = -n_{g(\tilde{p})}. \end{aligned} \tag{3.3.41}$$

where a map g was defined to take the lattice Λ to its dual $\tilde{\Lambda}$ and vice versa. A hypercubic lattice is a regular d-dimensional grid in which each site connects to $2d$ nearest neighbours along orthogonal directions. This structure ensures that both Λ and $\tilde{\Lambda}$ share the same geometry up to a half-lattice translation, allowing a one-to-one correspondence between electric and magnetic variables under g. Consequently, duality transformations—such as interchanging fields and their duals—can be implemented consistently across the entire lattice.[36, 42].

Observe that models of this kind can now be coupled to both magnetic and electric matter in a conventional manner, similar to their space-time analogues [36, 42].

3.4 Exotic Theories

In this section we want to study a version of the XY model [43], which can be seen as analogue of the Minkowski Langrangian,

$$L = \frac{\mu_0}{2}(\dot{\phi})^2 - \frac{1}{\mu_1}(\partial_1\partial_2\phi)^2. \tag{3.4.1}$$

This model is endowed with what is called a momentum subsystem symmetry (which analogue to a compact symmetry), due to the shift that can be made on $\phi(x^1, x^2)$,

$$\phi(x^1, x^2) \to \phi(x^1, x^2) + f(x^1) + g(x^2) \tag{3.4.2}$$

where $f(x^1)$ and $g(x^2)$ are arbitrary functions of x^1, x^2. Like the XY-plaquette model has an emergent symmetry in $(1 + 1)$ dimensions in a particular regime, this model has associated with the charges $Q_1 = \frac{1}{2\pi}\int dx^1(\partial_1\partial_2\phi)$ and $Q_2 = \frac{1}{2\pi}\int dx^2(\partial_1\partial_2\phi)$ [38, 44–53]. In the next sections, we are considering the Hamiltonians version of the models of [44].

3.4.1 XY-plaquette model and winding symmetries

The Hamiltonian of the XY-plaquette model is

$$H = \sum_x \left(\frac{1}{2Ja}\pi_x^2 + \frac{J}{2a}\left(\Delta_1\Delta_2\phi_x + 2\pi n_x\right)^2 \right) \tag{3.4.3}$$

where, as before, x is the position on a 2D lattice, the index $i = 1, 2$ represents the horizontal and vertical directions of the lattice. Δ_i is the finite difference operator, in the $i = 1, 2$ directions, such that $\Delta_1\phi_x = \phi_{x_1+1} - \phi_{x_1}$. The integer operator n_x has a canonical conjugate φ_x,

$$[\varphi_x, n_y] = i\delta_{x,y}. \tag{3.4.4}$$

We propose the following transformation,

$$\phi_x \to \phi_x + 2\pi k_x,$$

$$n_x \to n_x - \Delta_1\Delta_2 k_x,$$

we state this is an invariance, given that k is an integer. To promote this to a gauge symmetry, we need to describe the operator that generates this transformation, which must be an identity operator on the Hilbert space.

$$e^{i\sum_x(2\pi k_x\pi_x) - i\sum_x(\Delta_1\Delta_2 k)_x\varphi_x}, \tag{3.4.5}$$

and rewriting the second term, by use of a "integration" by parts rule,

$$\sum_x (\Delta_i f)_x g_x = \sum_x (f_{x+\hat{i}} - f_x) g_x = \sum_x f_x (g_{x-\hat{i}} - g_x) = -\sum_x f_x (\Delta_i g)_{x-\hat{i}}, \tag{3.4.6}$$

we get,

$$e^{i\sum_x(2\pi k_x \pi_x) - i\sum_x\left(k_x \Delta_1 \Delta_2 \varphi_{x-\hat{1}-\hat{2}}\right)}. \tag{3.4.7}$$

This generator must act as an identity operator on the Hilbert space, thus it follows that,

$$\pi_x = \frac{\Delta_1 \Delta_2 \varphi_{x-\hat{1}-\hat{2}}}{2\pi} + m_x \tag{3.4.8}$$

where m_x is an operator with integer spectrum and must satisfy the following commutation relation

$$[n_x, m_y] = \frac{i}{2\pi}\left(\delta_{x,y} - \delta_{x,y-\hat{2}} - \delta_{x,y-\hat{1}} + \delta_{x,y-\hat{1}-\hat{2}}\right). \tag{3.4.9}$$

Hence, the Hamilton becomes

$$H = \sum_x \left\{ \frac{1}{2Ja(2\pi)^2}\left(\Delta_1\Delta_2\varphi_x + 2\pi m_{x+\hat{1}+\hat{2}}\right)^2 + \frac{1}{2a}\left(\Delta_1\Delta_2\phi_x + 2\pi n_x\right)^2 \right\}, \tag{3.4.10}$$

and it is invariant under the following transformations,

$$\begin{aligned} &\phi_x \to \varphi_x, \quad \varphi_x \to \phi_{x+\hat{1}+\hat{2}}, \\ &n_x \to m_{x+\hat{1}+\hat{2}}, \quad m_x \to n_x. \end{aligned} \tag{3.4.11}$$

and $J \to \left(\frac{1}{2\pi}\right)\frac{1}{J}$. This also implies that these commutation relations are also invariant under the self-dual transformation, which can be easily checked.

There are two winding symmetries that this model possess, $\phi_x \to \phi + f_2(x^1) + f_2(x^2)$ and $\varPhi_x \to \varPhi_x + g_2(x^1) + g_2(x^2)$. We leave the solution to this model to appendix (B.1) and here we comment its main properties. The solution is of the form,

$$\begin{aligned} H = &\frac{1}{2JaN_1^2N_2^2}\sum_x \left(\Pi_0 - N_1\Pi_1(x_1) - N_2\Pi_2(x_2)\right)^2 \\ &+ \frac{J}{2aN_1^2N_2^2}\sum_x \left(\Pi_0 - N_1\tilde{\Pi}_1(x_1) - N_2\tilde{\Pi}_2(x_2)\right)^2 \\ &+ \sum_p \omega_p \left(B_p^\dagger B_p + \frac{1}{2}\right). \end{aligned} \tag{3.4.12}$$

Where, the operators Π_0, $\Pi_1(x_1)$, and $\Pi_2(x_2)$ correspond to the conjugate momenta associated with the zero-mode sector of ϕ_x. Specifically, Π_0 is the momentum conjugate to the spatially constant part of the field, while $\Pi_1(x_1)$ and $\Pi_2(x_2)$ are the momenta conjugate to the components of ϕ_x that depend solely on x_1 or x_2, respectively. These quantities capture the contributions of the winding sectors along each spatial direction and are constrained by $\sum_{x_1} \Pi_1(x_1) = \sum_{x_2} \Pi_2(x_2) = \Pi_0$. Some of the symmetries becomes obvious to notice,

$$J_{0,x} = \pi_{0,x} \tag{3.4.13}$$

$$J^{1,2} = -\frac{J}{a}\left(\Delta_1\Delta_2\phi_{x-\hat{1}-\hat{2}} + 2\pi n_{x-\hat{1}-\hat{2}}\right) \tag{3.4.14}$$

$$\partial_0 J^0_x - \Delta_1\Delta_2 J^{12}_x = 0. \tag{3.4.15}$$

and the chargers associated to these symmetries are,

$$Q_1(x_1) = \sum_{x_2} J_{0,x} \tag{3.4.16}$$

$$Q_2(x_2) = \sum_{x_1} J_{0,x} \tag{3.4.17}$$

3.4.2 Quantum Ising Model Duality

In this section, we show that the gauged variant of the previous model is equivalent to an Ising model. We begin by introducing the gauge symmetries and then take the strong gauge coupling limit. This procedure allows us to reinterpret the operators as Pauli matrices and thereby obtain the dual Ising model.

We start from the Hamiltonian (3.4.10). We want to gauge the tensor symmetry of the currents $J_{0,x}$, $J^{1,2}_x$. We introduce the following gauge symmetries,

$$A_{x,0} \to A_{x,0} + \partial_0\varphi_x \tag{3.4.18}$$

$$A_{x,12} \to A_{x,12} + \Delta_1\Delta_2\varphi_x. \tag{3.4.19}$$

Where we expect the theory to be invariant under $A_{x,12} \to A_{x,12} + 2\pi$. Field strength tensor is defined as

$$F_{x,0,12} = \partial_0 A_{12} - \Delta_1 \Delta_2 A_0, \tag{3.4.20}$$

and the corresponding Lagrangian,

$$L = \sum_x \frac{\beta a}{2} F^2_{x,0,12}. \tag{3.4.21}$$

The related Hamiltonian is then,

$$H = \sum_x \left\{ \frac{1}{2a\beta} \Pi^2_{x,12} + \left(\Delta_1 \Delta_2 A_{x,0}\right) \Pi_{x,12} \right\}, \tag{3.4.22}$$

where $\Pi_{x,12}$ is the conjugate momentum of $A_{x,12}$ and similarly, $\Pi_{x,0}$ is the conjugate momentum of $A_{x,0}$, however, $\Pi_{x,0} = 0$, following Dirac's classification of constraints [54], and thus commutes with H,

$$[H, \Pi_{x,0}] = 0. \tag{3.4.23}$$

If we manipulate the last expression further, we arrive at

$$\Delta_1 \Delta_2 \Pi_{x,12} = 0, \tag{3.4.24}$$

which is the Gauss law constraint. Implementing this into the Hamiltonian,

$$H = \sum_x \frac{1}{2\beta a} \Pi^2_{x,12}, \tag{3.4.25}$$

which actually could have been achieved if we imposed a gauge invariance of $A_{x,12} \rightarrow A_{x,12} + \Delta_1 \Delta_2 \varphi_x$. Such transformation would be generated by an operator of the form

$$e^{i \sum_x \Delta_1 \Delta_2 \phi_x \Pi_{x,12}} = \mathbb{1}. \tag{3.4.26}$$

which leads to (3.4.24). Moreover, $A_{x,12} \rightarrow A_{x,12} + 2\pi k_{x,12}$ for any choice of $k_{x,12}$, resulting in a integer spectrum of the operator $\pi_{x,12}$. Let us introduce a $\theta-$term in the last Hamiltonian,

$$H = \sum_x \frac{1}{2\beta a} \left(\Pi_{x,12} + \frac{\theta}{2\pi} \right)^2. \tag{3.4.27}$$

Which can be solved by diagonalizing $\Pi_{x,12}$. Its ground state is given by integer eigenvalues $m_{x,12}$ of $\Pi_{x,12}$, subject to the constraint,

$$\Delta_1 \Delta_2 m_{x,12} = 0. \tag{3.4.28}$$

If θ takes any value different than π, $m_{x,12}$ is null everywhere. If $\theta = \pi$ than there are two possible values of $m_{x,12}$, $c(x_1)$ and $c(x_2)$ where $c(x_{1,2})$ are constrained to be 1 or 0. The ground state degeneracy is $2^{N_1} + 2^{N_2} - 2$.

This model is also endowed with the symmetry,

$$\partial_0 \Pi_{x,12} = 0, \tag{3.4.29}$$

besides the Gauss's law $\Delta_1 \Delta_2 \Pi_{x,12}$. This 1-form symmetry allows $\Pi_{x,12}$ to be non-constant, depending on x_1 and x_2.

We now gauge the $U(1)$ subsystem symmetry of our model, which leads to coupling the gauge fields in the form of an XY plaquette model,

$$H = \sum_x \frac{1}{2Ja} \pi_x^2 - \frac{J}{a} \cos\left(\Delta_1 \Delta_2 \phi + A_{x,12}\right) + \sum_x \frac{e^2}{2\beta a} \left(\Pi_{x,12} - \frac{\theta}{2\pi}\right)^2 \tag{3.4.30}$$

Let's explore the strong gauge coupling limit, i.e. $e^2 \to \infty$ and assuming $\theta = \pi$. In this scenario, $\Pi_{x,12}$ is constrained to be either 1 or 0. Albeit the energy is still infinity, by constraining $\Pi_{x,12}$ to those two values, we selecting the lowest possible values of the energy. Any other state gets separated by an energy gap of $1/\beta a$. Thus, we can rewrite $\Pi_{x,12}$ in terms of an Pauli matrix,

$$\Pi_{x,12} = \frac{1}{2}\left(\sigma_x^3 + 1\right). \tag{3.4.31}$$

Following from that, π_x gets rewritten as

$$\pi_x = \Delta_1 \Delta_2 \Pi_{x-\hat{1}-\hat{2},12} \to \frac{1}{2} \Delta_1 \Delta_2 \sigma_x^3. \tag{3.4.32}$$

The cosine term can be written as,

$$\cos(\Delta_1 \Delta_2 \phi_x + A_{x,12}) \to \frac{1}{2}\left(\sigma_x^+ + \sigma_x^-\right) = \frac{1}{2}\sigma_x^1. \tag{3.4.33}$$

From the first term,

$$\sum_x \pi_x^2 \to \sum_x \left(\frac{1}{2}\Delta_1\Delta_2\sigma_x^3\right)^2 \tag{3.4.34}$$

we expand the quadratic term into,

$$\sum_x \left(\Delta_1\Delta_2\sigma_x^3\right)^2 = 2\sum_x \left(\sigma_x^3\sigma_{x+\hat{1}+\hat{2}} - 2\sigma_x^3\sigma_{x+\hat{1}}^3 - 2\sigma_x^3\sigma_{x+\hat{2}}^3 + \sigma_{x+\hat{1}}^3\sigma_{x+\hat{2}}^3\right), \tag{3.4.35}$$

and use this expansion on the expression (3.4.30), drop some irrelevant constants and obtain an effective Hamilton of an Ising Model,

$$H_{\text{eff}} = \sum_x \frac{1}{4aJ}\left(\sigma_x^3\sigma_{x+\hat{1}+\hat{2}}^3 - 2\sigma_x^3\sigma_{x+\hat{1}}^3 - 2\sigma_x^3\sigma_{x+\hat{2}}^3 + \sigma_{x+\hat{1}}^3\sigma_{x+\hat{2}}^3\right) - \sum_x \frac{J}{2a}\sigma_x^1. \tag{3.4.36}$$

We can rewrite this expression, grouping its term by neighboring sites,

$$H_{\text{eff}} = -J_1\sum_{\langle xy\rangle}\sigma_x^3\sigma_y^3 + J_2\sum_{\langle\langle xy\rangle\rangle}\sigma_x^3\sigma_y^3 - h\sum_x \sigma_x^1. \tag{3.4.37}$$

Where we rewrote some constants as,

$$J_1 = \frac{1}{2aJ},\quad J_2 = \frac{1}{4aJ}\ \text{ and }\ h = \frac{J}{2a}.$$

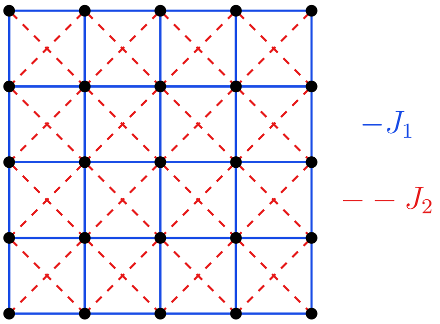

Figure 3.2: Schematic representation of the Lattice structure with nearest-neighbor interactions (J_1 in blue) and next-nearest-neighbor interactions (J_2 in red). Dots indicate lattice sites.

Moreover, $\langle xy\rangle$ symbolizes a sum over the next-neighboring sites, while $\langle\langle xy\rangle\rangle$ the sum runs over the next to next-neighbouring sites. A schematic view os this interactions can be seen in the picture.

We will refer to this as the transverse-field J_1-J_2 Ising model. Since our aim is to study the phase diagram of (3.4.30), and because in the strong gauge coupling limit

($e^2 \to \infty$) the theory lies in the same universality class as this simpler Ising model, it is more practical to investigate its behaviour through Monte Carlo simulations, which is our present goal. We will rewrite this Hamiltonian, using the Suzuki-Trotter decomposition and use the resulting partition function in a Monte Carlo simulation. To do that, we rewrite the partition of this system in terms of eigenvalues instead of operators, i.e. to "transform" this expression into its classical equivalent. Before that though, let's discuss some of the characteristics of Transverse field J_1-J_2 Ising Model

The ground state of this model is rather degenerate, even when the transverse field is non-zero. The reason is as follows: if we consider two slightly different states at $h = 0$, the transition probability between them is proportional to both the value of h and the number of spin sites where they differ. In the thermodynamic limit, when $h \ll 1$, these states have essentially no overlap, so the degeneracy is not fully lifted. As the field strength increases, $h \gg 1$, the spins tend to align with the field direction, leading to a unique polarised ground state and thus lifting the degeneracy. Our conjecture is that the system must undergo a phase transition when evolving from a highly degenerate state to a collinear phase. The central question is then: if such a transition exists, what is its nature?.

The ground-state degeneracy reaches its maximum when $J_1 = 2J_2$ in the limit $h \to 0$. Recall that this model arises from expanding the cross-finite differences in Eq. (3.4.35), and a valid ground state must minimize that contribution. This term originates from π_x^2 and is subject to the Gauss law constraint (3.4.24), which admits a large set of solutions—hence the natural appearance of a highly degenerate ground-state manifold.

When $J_1 < 2J_2$, the system enters an antiferromagnetic phase, whereas for $J_1 > 2J_2$, it adopts a striped phase (see Fig. 3.3). Neither phase, however, fully lifts the ground-state degeneracy.

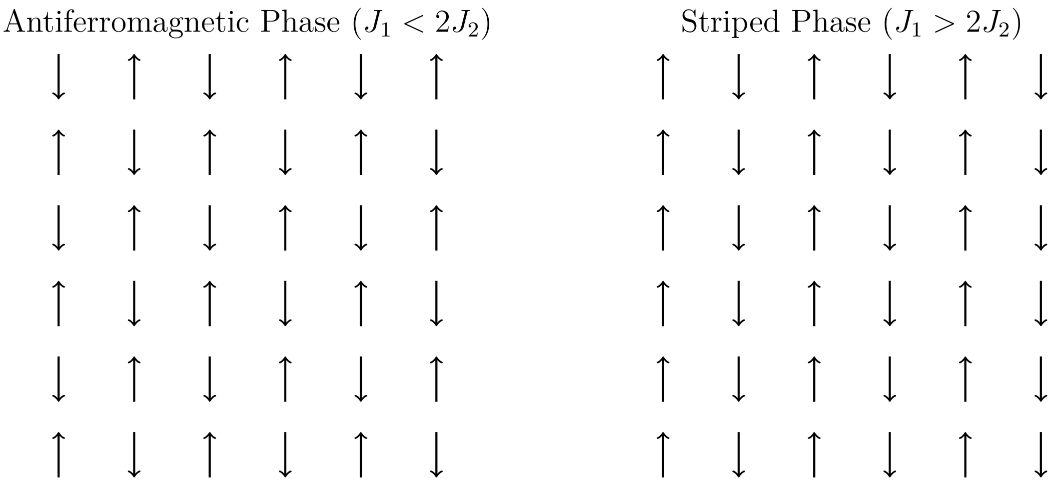

Figure 3.3: Schematic spin configurations. Left: antiferromagnetic phase with alternating up and down spins in a checkerboard pattern. Right: striped phase with alternating columns of spins pointing uniformly up or down.

The phase structure of the J_1–J_2 model reflects the competition between nearest-neighbor (J_1) and next-nearest-neighbor (J_2) interactions. When $J_1 < 2J_2$, the next-nearest-neighbor coupling dominates, favoring an antiferromagnetic ordering where spins alternate in a checkerboard pattern. Conversely, for $J_1 > 2J_2$, the nearest-neighbor interaction becomes stronger, and minimizing its energy requires aligning spins along one direction. However, to reduce the residual frustration from the next-nearest-neighbor term, adjacent rows (or columns) of spins orient oppositely, giving rise to a striped configuration where ferromagnetic chains alternate in sign. The boundary at $J_1 = 2J_2$ marks a highly frustrated regime where the two competing interactions balance, leading to an extensive ground-state degeneracy and enhanced fluctuations between competing spin patterns. At the special point $J_1 = 2J_2$ with $h \to 0$, the degeneracy is particularly large. One source of this is the charge $q_x = \sigma_x^3$, which is odd under charge conjugation, $q_x \to -q_x$. Since q_x can take only the values ± 1, the configurations $\{q_x\}$ and $\{-q_x\}$ are distinct, and both qualify as ground states. More generally, the ground states are labeled by the configurations of the conserved charges $\{q_x\}$, and charge conjugation symmetry ensures that the set $\{-q_x\}$ is also part of the ground-state manifold. This reflects a mixed anomaly between the local charges q_x and the global charge

$$C = \sum_x \sigma_x^1.$$

This observation is consistent with the previous discussion: in both the antiferromagnetic and striped phases, charge conjugation symmetry is spontaneously broken, partially lifting the degeneracy.

Chapter 4

Monte Carlo Simulations

In this chapter, we will perform Monte Carlo simulations of the Fracton-inspired model that we found to be dual to the Frustrated Ising Model. Our goal is to understand the phase transition that this model undergoes, as we postulated in our explanation of the highly degenerate ground state.

To do that, we will first perform a few validation runs with the well-known isotropic 3D Ising Model and the 3D Transverse Field Ising Model. These 'sanity check' simulations allow us to verify that our implementation reproduces established results and provides reliable estimates of critical points. Once validated, we will systematically simulate the Fracton-inspired model across a range of values for the driving parameter, carefully analyzing the Binder cumulant, magnetization, and susceptibility to characterize the phase transition and construct the phase diagram.

4.1 3D Isotropic Ising verification

In this section, we focus on the limit $J_2 \to 0$, where the model reduces to the well-known isotropic three-dimensional Ising model. Our objective here is twofold: first, to verify that our Monte Carlo implementation correctly reproduces established results for this benchmark system, and second, to extract the critical temperature associated with the phase transition. This serves as a consistency check before moving on to more complex cases.

The Hamiltonian in this limit is given by

$$H_{\text{3D-Ising}} = -J \sum_{\{s_{i,j,k}=\pm 1\}} \left(s_{i,j,k}s_{i+1,j,k} + s_{i,j,k}s_{i,j+1,k} + s_{i,j,k}s_{i,j,k+1}\right), \tag{4.1.1}$$

with no external field present.

The statistical weight of a spin configuration C is determined by the Boltzmann distribution,

$$P(C) = \frac{1}{Z} e^{-E(C)/T}, \tag{4.1.2}$$

where Z is the partition function and $E(C)$ is the energy associated with configuration C. The temperature T here is the control parameter governing the competition between ordering and disorder: at low T, the system minimizes its energy and favors aligned spins (ferromagnetic order), whereas at high T, entropy dominates and spins become uncorrelated, leading to the disordered paramagnetic phase. The critical temperature T_c marks the point of phase transition between these regimes.

To simulate this behavior, we employ the Metropolis–Hastings algorithm. The idea is to generate a Markov chain of configurations by proposing local updates—in this case, flipping a single spin $s_{i,j,k}$, and deciding whether to accept the new configuration C' based on the energy change

$$\Delta E = -2J \left(\sum_{\langle i',j',k' \rangle} s_{i',j',k'} \right). \tag{4.1.3}$$

If $\Delta E \leq 0$, the new configuration is always accepted, since it lowers the energy. Otherwise, it is accepted with probability $\exp(-\Delta E/T)$, ensuring detailed balance and convergence to the Boltzmann distribution. Repeated application of this procedure allows us to efficiently sample the configuration space and measure thermodynamic observables across temperatures, from which T_c can be extracted.

For the simulations, we employ 200,000 equilibration steps and 50 decorrelation steps to reduce autocorrelations between measurements. A total of 10^6 statistically independent configurations are collected for each parameter set. The lattice sizes considered are $L = [10, 20, 40, 80]$, while J is fixed to unity to set the energy scale. The temperature is varied in the interval $T \in [2, 8]$, with steps of $dT = 0.5$. Moreover, in all of our simulations—both in this section and in those that follow—statistical uncertainties were estimated using a combination of binning analysis [55] and the jackknife method [56], ensuring a reliable treatment of error bars.

The first observable of interest is the magnetization, which serves as the order parameter of the model. As expected, it shows a sharp drop around the critical temperature T_c, indicating a symmetry-breaking phase transition between the ferromagnetic and paramagnetic regimes. This behavior is displayed in Fig. 4.1. Although error bars were computed and included in the plot, they are not visible due to their negligible magnitude. At low T, the magnetization is close to unity, while at high T, it vanishes, consistent with the restoration of spin-flip symmetry. The exact vanishing of the order parameter occurs only in the thermodynamic limit, while finite lattice sizes yield a smooth crossover.

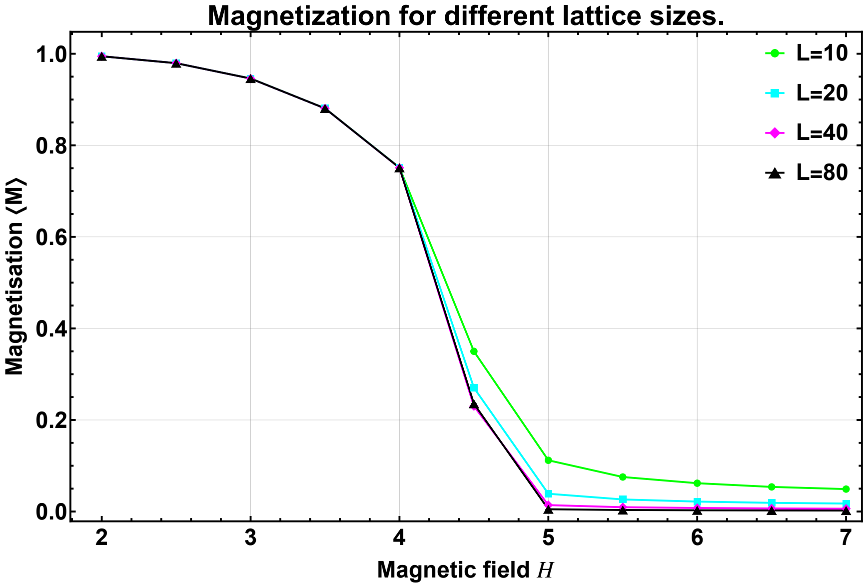

Figure 4.1: Magnetization for lattice sizes 10, 20, 40, and 80. As expected, the order parameter decreases as the temperature increases and approaches zero above the critical temperature.

We next analyze the Binder cumulant, which provides a more reliable determination of the critical temperature. The finite-size scaling analysis of the crossing points yields $T_c \approx 4.5(3)$. To obtain this error, we performed a finite-size scaling analysis with bootstrap resampling. The critical temperature was determined by minimizing a cost function that quantifies the quality of the finite-size collapse of the Binder cumulant curves for different lattice sizes. The uncertainty was estimated through a bootstrap procedure, where synthetic datasets were generated by adding Gaussian noise to the original Binder cumulant data and the minimization was repeated for each resampled dataset. The standard deviation of the resulting distribution of critical temperatures provides the reported error estimate.

The central value is consistent with the established literature value near 4.5 [57]; however, the statistical error is intrinsic to the crossing method with the limited system sizes studied here. This level of precision is satisfactory for our purpose, as this simulation serves primarily as a sanity check to verify that our model implementation correctly reduces to the well-known Ising universality class. The estimate successfully locates the critical region, confirming the validity of our computational framework. A more precise determination would require analysis of larger lattices. The crossing is visualized in Fig. 4.2.

Finally, the magnetic susceptibility is presented in Fig. 4.3. The peak position provides another estimate for the critical temperature, yielding $T_c \approx 4.5(3)$, again consistent with the previous results.

In summary, we have demonstrated that our Monte Carlo implementation reproduces the critical behavior of the 3D Ising model, obtaining results consistent with the literature. Having established the validity of our method in this classical benchmark, we now proceed to study the more involved case of the transverse Ising model through the Suzuki-Trotter decomposition, and the more complex J_1-J_2 Transverse Ising Model.

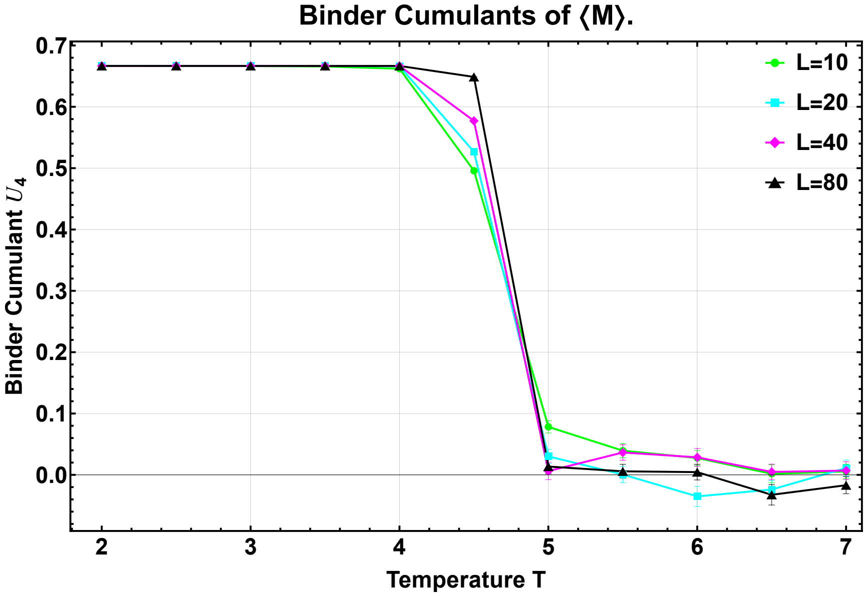

Figure 4.2: Binder Cumulant for lattice sizes 10, 20, 40, and 80. The curves intersect at $T_c \approx 4.5(3)$, consistent with the literature value of the critical temperature. The methodology used for the error consisted in FSS analysis with bootstrap resampling.

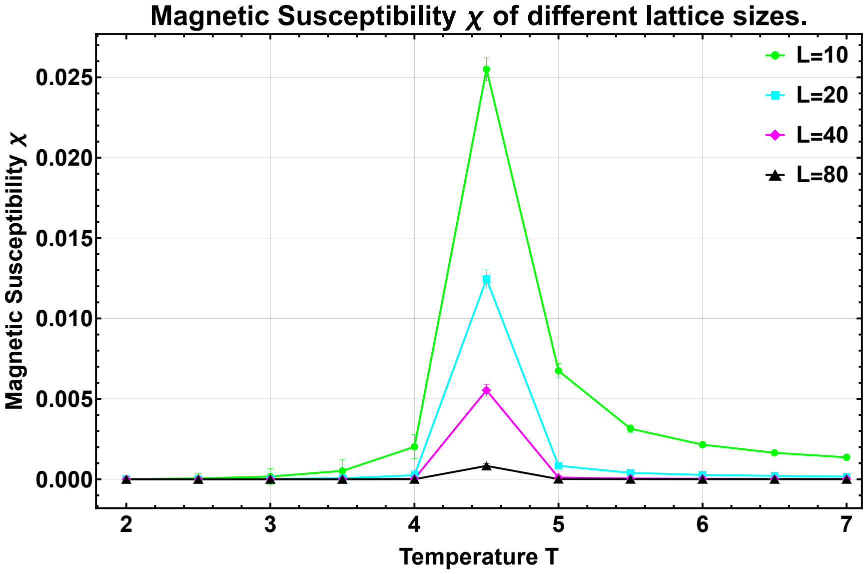

Figure 4.3: Magnetic susceptibility for lattice sizes 10, 20, 40, and 80. The susceptibility peaks around $T_c \approx 4.5(3)$, in agreement with the critical point extracted from the Binder cumulant. The methodology used for the error consisted in FSS analysis with bootstrap resampling.

4.2 From Quantum to Classical Ising

In the last section of the previous chapter, we mentioned that the system (3.4.36) must undergo a phase transition as it evolves from a highly degenerate ground state to an ordered phase. Analytically, characterising such transitions in frustrated and highly degenerate systems is notoriously difficult. For this reason, we resort to Monte Carlo simulations, which provide a non-perturbative and numerically controlled way to probe the properties of the model.

With the goal of explaining the phase transition that the model goes through at the highly degenerate point of $g = \frac{J_2}{J_1} = 0.5$, we use Monte Carlo simulations to explore the behaviour of the system between $g = 0$ and $g = 0.5$. To achieve that, we first perform the Suzuki-Trotter decomposition [13] to find a classical equivalent of (3.4.37). This decomposition is a standard approach for mapping a d-dimensional quantum system at finite temperature to an equivalent $(d+1)$-dimensional classical system. By introducing an extra (imaginary) time dimension, we can apply efficient classical Monte Carlo techniques to study the thermodynamic behaviour of the quantum model without having to directly simulate the full quantum dynamics.

We start by writing the partition function related to this system,

$$Z = \sum_{\{s_j = \pm 1\}} e^{-\beta H_{\text{eff}}}, \tag{4.2.1}$$

where H_{eff} is given by (3.4.36). The appearance of β follows directly from the definition of the canonical ensemble in statistical mechanics. In equilibrium at temperature T, the probability of a given configuration with energy E is proportional to $e^{-\beta E}$. This Boltzmann weight defines the probability of a configuration in the canonical ensemble, ensuring that, at equilibrium, lower-energy configurations are statistically more probable than higher-energy ones. The parameter β controls the balance between energy minimization and thermal fluctuations. Its relationship with temperature can be written as,

$$\beta = \frac{1}{T}. \tag{4.2.2}$$

In this context, we introduce a discretisation of the β by writing

$$\beta \to \varepsilon N, \tag{4.2.3}$$

where N is the number of imaginary-time slices and ε is the imaginary-time step size. Physically, $\beta = \frac{1}{T}$, so ε has the dimension of inverse energy and is directly proportional to the inverse temperature, but scaled by the number of slices:

$$\varepsilon = \frac{\beta}{N} = \frac{1}{NT}. \tag{4.2.4}$$

Thus:

- For fixed T, increasing N decreases ε, meaning each Trotter slice represents a finer resolution in imaginary time.
- For fixed N, lowering T (increasing β) increases ε, which corresponds to each slice covering a larger imaginary-time extent.

From a physical standpoint, ε controls the strength of the coupling between neighbouring Trotter slices in the classical mapping: small ε corresponds to a weak coupling (high T or large N), while large ε implies strong coupling (low T or small N). In the limit $N \to \infty$, $\varepsilon \to 0$ and the Suzuki–Trotter approximation becomes exact, with the product $N\varepsilon$ remaining constant. Introducing this discretisation of β into the partition function, we have

$$Z = \sum_{\{s_x = \pm 1\}} e^{\underbrace{-\varepsilon H_{\text{eff}} - \varepsilon H_{\text{eff}} - \ldots - \varepsilon H_{\text{eff}}}_{N \text{times}}}. \tag{4.2.5}$$

Or simply,

$$\Rightarrow Z = \sum_{\{s_j = \pm 1\}} \Pi_{l=1}^{N} \left(e^{-\varepsilon H_{\text{eff}}} \right). \tag{4.2.6}$$

Next step is to introduce a complete set of states $\{s_j\}$ between each of exponential in (4.2.5), that are eigenstates of σ_x^3, that is $\sigma_x^3 \left|\{s_j\}\right\rangle = s_j \left|\{s_j\}\right\rangle$. We arrive at the expression,

$$Z = \sum_{\{s_j = \pm 1\}} \Pi_{l=1}^{N} \left\langle \{s_j(l+1)\} \right| \left(e^{-\varepsilon H_{\text{eff}}} \right) \left| \{s_j(l)\} \right\rangle. \tag{4.2.7}$$

Now we make the following statement,

$$e^{\varepsilon H_{\text{eff}}} = \mathbb{T}, \tag{4.2.8}$$

where $\mathbb{T}$ is the transfer matrix. The transfer matrix allows us to view the 'spatial' evolution as an analogue to temporal evolution in quantum mechanics, meaning that H_{eff} plays the role of time-evolution operator in quantum mechanics.

Taking $\varepsilon \approx 0$, we can decompose the non-commuting parts of $\mathbb{T}$ into the following,

$$\mathbb{T} = \mathbb{T}_1\mathbb{T}_3 + \mathcal{O}(\varepsilon^2). \tag{4.2.9}$$

where $\mathbb{T}_3$ and $\mathbb{T}_1$, are given by,

$$\mathbb{T}_3 = e^{\sum_x -\frac{\varepsilon}{4aJ}\left(\sigma^3_x\sigma^3_{x+\hat{1}+\hat{2}} - 2\sigma^3_x\sigma^3_{x+\hat{1}} - 2\sigma^3_x\sigma^3_{x+\hat{2}} + \sigma^3_{x+\hat{1}}\sigma^3_{x+\hat{2}}\right)} \tag{4.2.10}$$

and

$$\mathbb{T}_1 = e^{-\frac{J\varepsilon}{2a}\sum_x \sigma^1_x}. \tag{4.2.11}$$

We get,

$$Z = \sum_{\{s_j=\pm 1\}} \Pi_{l=1}^{N} \left\langle \{s_j(l+1)\}\right| (\mathbb{T}_1\mathbb{T}_3) \left|\{s_j(l)\}\right\rangle. \tag{4.2.12}$$

where the higher order terms were discarded.

The result of $\mathbb{T}_3$ acting on the eigenstates $|\{s_x(l)\}\rangle$ is simply,

$$\mathbb{T}_3 \left|\{s_x(l)\}\right\rangle = e^{\sum_x -\frac{\varepsilon}{4aJ}\left(s^3_x s^3_{x+\hat{1}+\hat{2}} - 2s^3_x s^3_{x+\hat{1}} - 2s^3_x s^3_{x+\hat{2}} + s^3_{x+\hat{1}} s^3_{x+\hat{2}}\right)}. \tag{4.2.13}$$

On the other hand, the action of $\mathbb{T}_1$ is not straightforward. To see its result, we look at the relevant term in the partition function,

$$\left\langle \{s_x(l+1)\}\right| e^{-\frac{J\varepsilon}{2a}\sum_x \sigma^1_x} \left|\{s_x(l)\}\right\rangle. \tag{4.2.14}$$

The result of the operator acting on $\mathbb{T}_1$ must be a 2x2 symmetric matrix, since spins can only be aligned or anti-aligned. We can parametrize the result such as,

$$\left\langle \{s_x(l+1)\}\right| e^{-\frac{J\varepsilon}{2a}\sum_x \sigma^1_x} \left|\{s_x(l)\}\right\rangle = e^{b s_x(l) s_x(l+1) + c}. \tag{4.2.15}$$

Expanding the exponential on the LHS into a power series and separating it into its even and odd part, we get,

$$\langle \{s_x(l+1)\}| \Big(\mathbb{1}\cosh(\Delta) - \sigma_x^1 \sinh(\Delta)\Big) |\{s_x(l)\}\rangle = e^{bs_x(l)s_x(l+1)+c}. \tag{4.2.16}$$

Where $\Delta = \frac{J\varepsilon}{2a}$. Since $s_x = \pm 1$, we can write the matrices as,

$$\begin{pmatrix} \cosh(\Delta) & -\sinh(\Delta) \\ -\sinh(\Delta) & \cosh(\Delta) \end{pmatrix} = \begin{pmatrix} e^{b+c} & e^{-b+c} \\ e^{-b+c} & e^{b+c} \end{pmatrix} \tag{4.2.17}$$

We discard c, as it is an overall constant, and solve for b, arriving at,

$$e^{-2b} = \tanh(\Delta) \Rightarrow b = -\frac{1}{2}\ln(\tanh(\Delta)). \tag{4.2.18}$$

With this, we can rewrite (4.2.14) as,

$$\langle \{s_x(l+1)\}| \, \mathbb{T}_1 \, |\{s_x(l)\}\rangle = e^{b\sum_x s_x(l)s_x(l+1)}. \tag{4.2.19}$$

With this, we get our final result, in terms of J_1,J_2 and h,

$$Z = \sum_{\{s_j=\pm 1\}} \Pi_{l=1}^N e^{\sum_{x=1}^L \varepsilon J_2 \left[s_x^3 s^3_{x+\hat{1}+\hat{2}} + s^3_{x+\hat{1}} s^3_{x+\hat{2}}\right] - \varepsilon J_1 \left[s_x^3 s^3_{x+\hat{1}} + s_x^3 s^3_{x+\hat{2}}\right] - b\sum_{x=1}^L s_x(l)s_x(l+1)}, \tag{4.2.20}$$

where $b = -\frac{1}{2}\ln(\tanh(\varepsilon|h|))$. It is important to notice that h can be both positive and negative and we are free to substitute $h \to |h|$. This is due to the spin inversion symmetry that the system has. If we consider the operator below,

$$U = \prod_x e^{i\frac{\pi}{2}\sigma_x^3}, \tag{4.2.21}$$

and applying this to the Hamiltonian, the terms $\sigma_x^3\sigma_y^3$ remain unchanged, since they are eigenvalues of the operator, while the term related to the transverse field will change according to

$$e^{-i\frac{\pi}{2}\sigma_x^3}\sigma_x^1 e^{i\frac{\pi}{2}\sigma_x^3} = -\sigma_x^1. \tag{4.2.22}$$

This means that regardless of the sign of the transverse-field, the system remains unchanged and we take $h \geq 0$.

4.2.1 Preliminaries

Before diving into the main results, we first establish some general aspects that will be used throughout the analysis.

Our strategy begins with reducing the model to simpler, well-known limiting cases that have been extensively studied. This allows us to benchmark our implementation and assess the reasonableness of our results. Specifically, in Section (4.1) and Section (4.2.2) we recover the standard isotropic 3D Ising Model and the 3D Transverse Field Ising Model, respectively. These serve as "sanity check" runs, ensuring that our approach reproduces established physics before addressing the more intricate regimes of the model.

Next, we discuss the algorithm of choice for the Monte Carlo runs. For the sanity check simulations we employ the standard Metropolis–Hastings algorithm, while in the main analysis we make use of a more efficient "row-flipping" variant, which will be described in detail later. As explained in Section (2.2), the Metropolis–Hastings scheme requires an acceptance ratio between the current configuration C and a proposed new configuration C'. The equilibrium distribution is given by the Boltzmann weight,

$$P(C) = \frac{1}{Z}\, e^{-E(C)/T}, \tag{4.2.23}$$

where Z is the partition function (4.2.20), T is the temperature, and $E(C)$ is the energy of configuration C:

$$E(C) = \sum_{x=1}^{L} J_1 \left[s_x(l)s_{x+\hat{1}}(l) + s_x(l)s_{x+\hat{2}}(l)\right] - J_2 \left[s_x(l)s_{x+\hat{1}(l)+\hat{2}}(l) + s_{x+\hat{1}}(l)s_{x+\hat{2}}(l)\right] + b\sum_{x=1}^{L} s_x(l)s_x(l+1). \tag{4.2.24}$$

This expression is obtained directly from (4.2.20). To update the system, we propose flipping a single spin $s_{i,j,k}$, i.e. $s'_{i,j,k} = -s_{i,j,k}$. The associated change in energy is

$$\Delta E = E(C') - E(C), \tag{4.2.25}$$

which evaluates to

$$\begin{aligned}\Delta E = s_{i,j,k}\Big[&\ln(\tanh(\varepsilon h))(s_{i,j,k-1} + s_{i,j,k+1}) \\ &- 2J_1\varepsilon(s_{i,j-1,k} + s_{i,j+1,k} + s_{i-1,j,k} + s_{i+1,j,k}) \\ &+ 2J_2\varepsilon(s_{i-1,j-1,k} + s_{i-1,j+1,k} + s_{i+1,j-1,k} + s_{i+1,j+1,k})\Big].\end{aligned} \tag{4.2.26}$$

or more compactly,

$$\Delta E = s_{i,j,k}\left[\tanh(\varepsilon h) \sum_{k' \in \{k-1,k+1\}} s_{i,j,k'} - J_1\varepsilon \sum_{\langle i',j' \rangle} s_{i',j',k} + J_2\varepsilon \sum_{\langle\langle i',j' \rangle\rangle} s_{i',j',k}\right], \tag{4.2.27}$$

where $\langle\cdot\rangle$ denotes nearest neighbours and $\langle\langle\cdot\rangle\rangle$ next-to-nearest neighbours.

The parameter ε appears here because it originates from the Suzuki–Trotter decomposition, where the quantum partition function is mapped to a classical one by discretizing imaginary time into slices of width ε. Physically, ε controls the resolution of this discretization: smaller values correspond to a finer partition of the imaginary-time direction, which yields a more faithful representation of the underlying quantum model. At the same time, smaller ε increases computational cost because more time slices are needed. In practice, one chooses ε small enough that observables become insensitive to further decreases, ensuring convergence while keeping the simulation efficient.

With this setup, we can now use ΔE as the acceptance ratio of the Metropolis–Hastings algorithm and perform Monte Carlo simulations. In the next section, we turn to another validation of our model through a simpler benchmark model, the 3D Transverse Ising case, to verify the correctness of our approach.

4.2.2 Transverse field Ising Model

We also validate our model by studying the transverse-field Ising model. Setting $J_2 = 0$, the Hamiltonian in equation (4.2.20) reduces to

$$Z = \sum_{\{s_j=\pm 1\}} \prod_{l=1}^{N} \exp\left[\sum_{x=1}^{L} -\varepsilon J_1 \left(s_x^3 s_{x+\hat{1}}^3 + s_x^3 s_{x+\hat{2}}^3\right) - b \sum_{x=1}^{L} s_x(l) s_x(l+1)\right], \tag{4.2.28}$$

which corresponds to the transverse-field Ising model.

In this case, the phase transition is driven by quantum fluctuations induced by the transverse magnetic field h. While the interaction term proportional to J_1 tends to align all spins in the same direction, the transverse field introduces fluctuations that destabilize this order. As a result, a quantum phase transition occurs near the critical value $h_c \approx 3.0$ [58]. The acceptance ratio is also reduced to,

$$\Delta E = s_{i,j,k}\Big[\tanh(\epsilon h) \sum_{k' \in \{k-1,k+1\}} s_{i,j,k'} - J_1 \varepsilon \sum_{\langle i',j' \rangle} s_{i',j',k}\Big]. \tag{4.2.29}$$

To investigate this, we performed simulations with 5,000,000 samples, discarding the first 100,000 steps for equilibration and introducing 50 decorrelation steps between measurements. The lattice sizes considered are $L = [10, 16, 24]$, while J is again fixed to unity. Since we are working at zero temperature, thermal fluctuations are absent and the phase transition is instead driven by quantum fluctuations controlled by the magnetic field h. We therefore vary h in the interval $h \in [2.9, 3.2]$, with steps of $dh = 0.05$.

In this zero-temperature setting, the Suzuki–Trotter decomposition introduced an additional discretization parameter, $\varepsilon = \beta/N$, where β is the inverse temperature and N the number of Trotter slices. Because $\beta \to \infty$ in the ground-state limit, one cannot simultaneously take $N \to \infty$ while keeping ε arbitrarily small in practice. Instead, ε must be fixed to the largest possible value for which physical observables have converged and remain stable. This ensures that the discretization faithfully captures the ground-state physics while keeping the computational cost manageable. In our simulations, we adopt such a fixed value of $\varepsilon = 0.05$, which allows us to consistently probe the zero-temperature regime.

The resulting Binder cumulant is shown in Fig. 4.4. The crossing of the curves yields a critical field of

$$h_c = 3.048(32), \tag{4.2.30}$$

which is in agreement with previously reported results in the literature. As explained for the temperature-driven transition, this value and its uncertainty were determined via a finite-size scaling analysis of the crossing points, with the error estimated through bootstrap resampling of the Binder cumulant data.

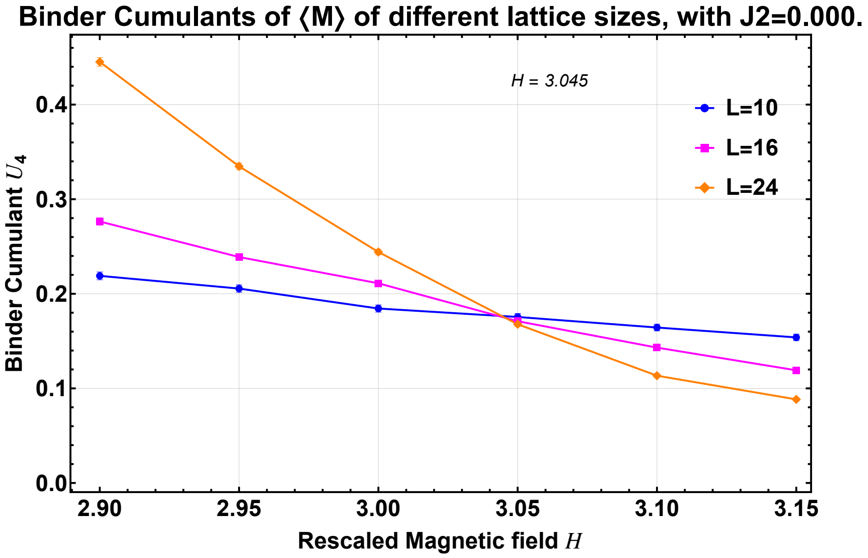

Figure 4.4: Binder cumulant for the transverse-field Ising model. The crossing between different system sizes occurs at $h \approx 3.05$, in agreement with well-established results.

As a consistency check, we perform a finite-size scaling (FSS) analysis of the model to verify that our results are correct and aligned with known theoretical predictions. In particular, we use the well-established critical exponents of the 3D Ising model to fit the location of the critical point. As the external field H is varied, the curves of different observables shift accordingly. Near the critical point, these curves approach each other and eventually collapse onto a single universal curve. This behavior is illustrated in Fig. 4.5, where data from different lattice sizes overlap.

As discussed in section 2.4, we apply finite-size scaling techniques to investigate the phase transition. The relevant rescaled quantities are

$$\mathscr{U}_4(H) = G(L^{1/\nu}, h), \tag{4.2.31}$$

$$\mathscr{M}(H) = L^{-\beta/\nu}\, G(L^{1/\nu}, h), \tag{4.2.32}$$

$$\chi(H) = L^{-\gamma/\nu}\, G(L^{1/\nu}, h), \tag{4.2.33}$$

where $h = (H - H_c)/H_c$ is the reduced magnetic field. Where $\beta = 0.32653$, $\nu =$

0.63012 and $\gamma = 1.2373$, which are the critical exponents of the same universality class the 3D Ising Model [59]. By tuning the rescaled parameter to its critical value, the curves corresponding to different lattice sizes collapse onto each other, as shown in Fig. 4.5. This confirms that the model is consistent with results from the literature. Having established this baseline, we can now proceed to study the more interesting case where $J_2 \neq 0$.

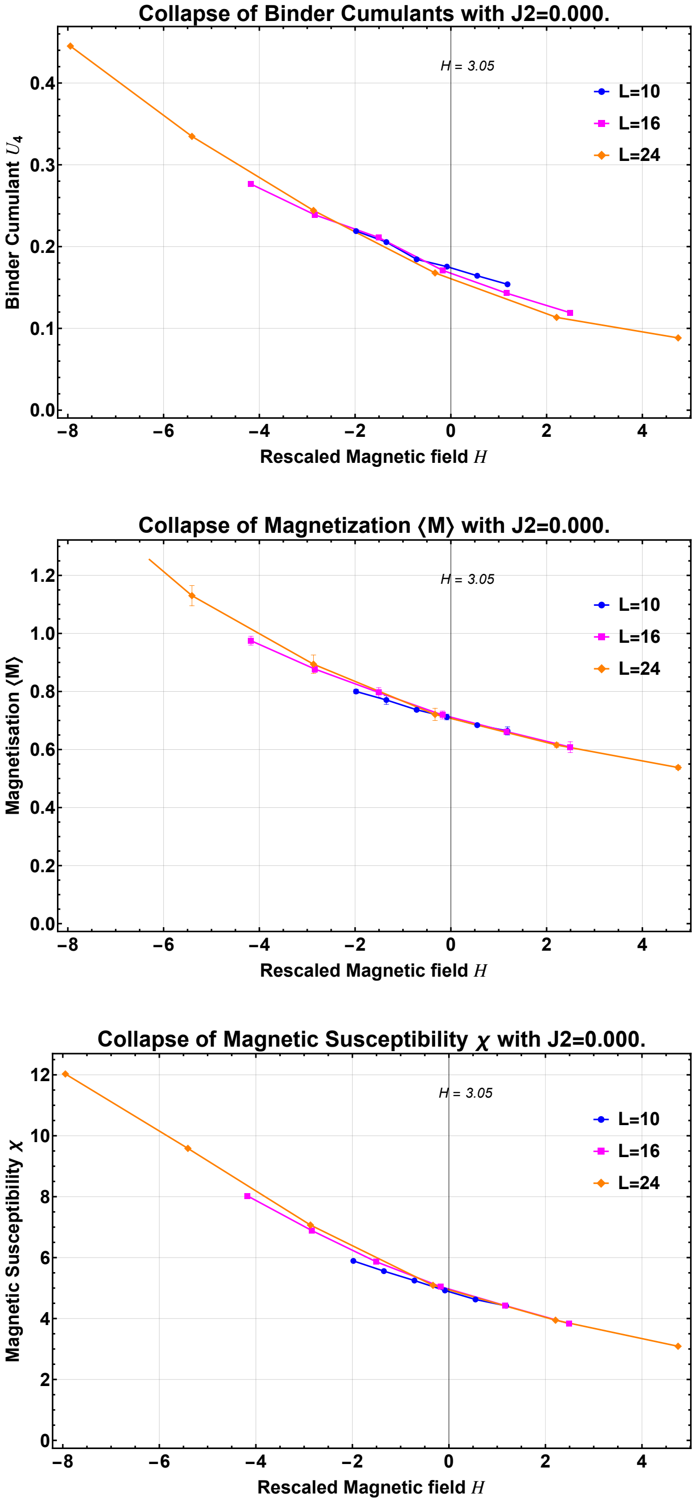

Figure 4.5: Finite-size scaling collapse of (a) the Binder cumulant, (b) the magnetisation, and (c) the magnetic susceptibility. In all cases, the critical magnetic field is found to be $h \approx 3.05$.

4.2.3 $J_2 \neq 0$, Phase transitions and Infinite Degenerate Vacua

We will now look at the (4.2.20), sometimes refered to $J1 - J2$ Ising Model, or Frustrated Transverse field Ising Model. In this model, it is also considered interactions through the diagonals of the sites of the lattice, weighted by the constant J_2 (see figure (3.2)).

Multiple Spin flipping

For a faster simulation and more efficient use of computational resources, we decided to change our update algorithm in the Ising Model. Our implementation of the Metropolis algorithm would only tries to update a single spin during Monte Carlo step. This means that it could take a great amount of sweeps for the system to be completely uncorrelated with itself, thus requiring an even larger amount of sweeps to gather all the necessary data for a meaningful study of its phase transitions and critical phenomena. To avoid these difficulties, we used a multiple-spin update algorithm, i.e. a row of spins is chosen randomly and all of the spins in that row are flipped, according the usual Metropolis-Hastings steps. The main difference comes into the weight (4.2.29), which now should take into account all of the spins that are being considered to be flipped.

To derive this new modified weight, we consider that a number dk of spins can be flipped. That is, if E' is the energy of the configuration with dk spins flipped, the difference between E and E' is then given by

$$\begin{aligned}\Delta E = & \ln(\tanh(\epsilon h))(s_{i,j,k}s_{i,j,k-1} + s_{i,j,k+dk}s_{i,j,(k+dk)+1}) \\ & \sum_{k'=k}^{k+dk} s_{i,j,k'}\Big[-2J_1\epsilon(s_{i,j-1,k'} + s_{i,j+1,k'} + s_{i-1,j,k'} + s_{i+1,j,k'}) \\ & + 2J_2\epsilon(s_{i-1,j-1,k'} + s_{i-1,j+1,k'} + s_{i+1,j-1,k'} + s_{i+1,j+1,k'})\Big],\end{aligned} \tag{4.2.34}$$

where we are summing over all the neighbours of the line of dk spins, and also taking into account the neighbours of the ends points of the line of spins being flipped. This

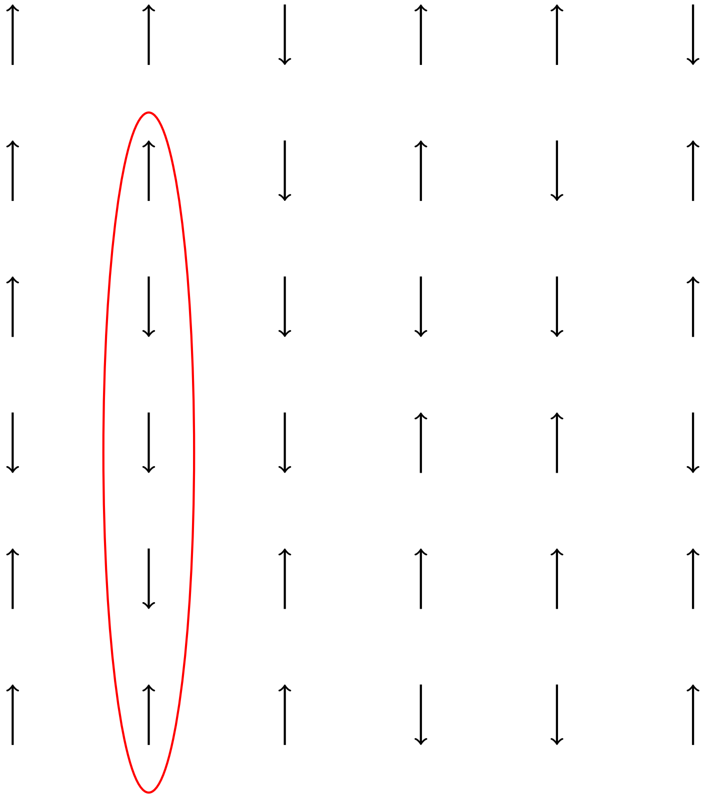

Figure 4.6: Schematic representation of a slice of the lattice. Each arrow represents a spin. The red circling represents the $k + dk$ spins being flipped at once. In this case, $k = 1$, $dk = 4$, thus 5 spins are being flipped.

allows us to perform much faster and efficient simulations.

Simulation Results and the Nature of the Phase Transition

Our goal in this section is to determine the nature of the phase transition that occurs at $g = 0.5$. To this end, we simulate the model for multiple values of the frustration parameter

$$g = \frac{J_2}{J_1},$$

starting from the transverse Ising case ($g = 0.0$) and gradually increasing in steps of 0.05 up to $g = 0.49$. The choice of $g = 0.49$ as the upper limit is deliberate: at $g = 0.5$ the ground state is highly degenerate, and the usual magnetization ceases to be a reliable order parameter, as stripe-ordered states yield $\langle M \rangle = 0$. Thus, $g = 0.49$ represents the closest accessible point to the degenerate case.

For clarity, we present detailed results only for $g = 0.1, 0.2, 0.3, 0.4$, and 0.49, each illustrating the methodology used to extract the critical field h_c. In all simulations, we fixed $J_1 = 1$, and varied the magnetic field h, the system sizes are taken to be $L = [24, 32, 38]$, we sample 25,000,000 different configurations with 500,000 thermalization steps, and 100 decorrelation steps are taken between each measurement. We performed finite-size scaling (FSS) analysis using the known critical exponents of the 3D Ising universality class, as mentioned in the previous sections. The systematic effects associated with ε have not been investigated in this work.

Case $g = 0.10$. We varied h in the interval $[2.65, 2.75]$, with incremental steps of 0.01, while keeping $J_2 = 0.1$ and $\varepsilon = 0.05$. We identified a critical field $h_c \approx 2.7$. Binder cumulants display the expected crossing, and the scaling collapse of the magnetization and susceptibility confirms the second-order character of the transition (see Fig. 4.7).

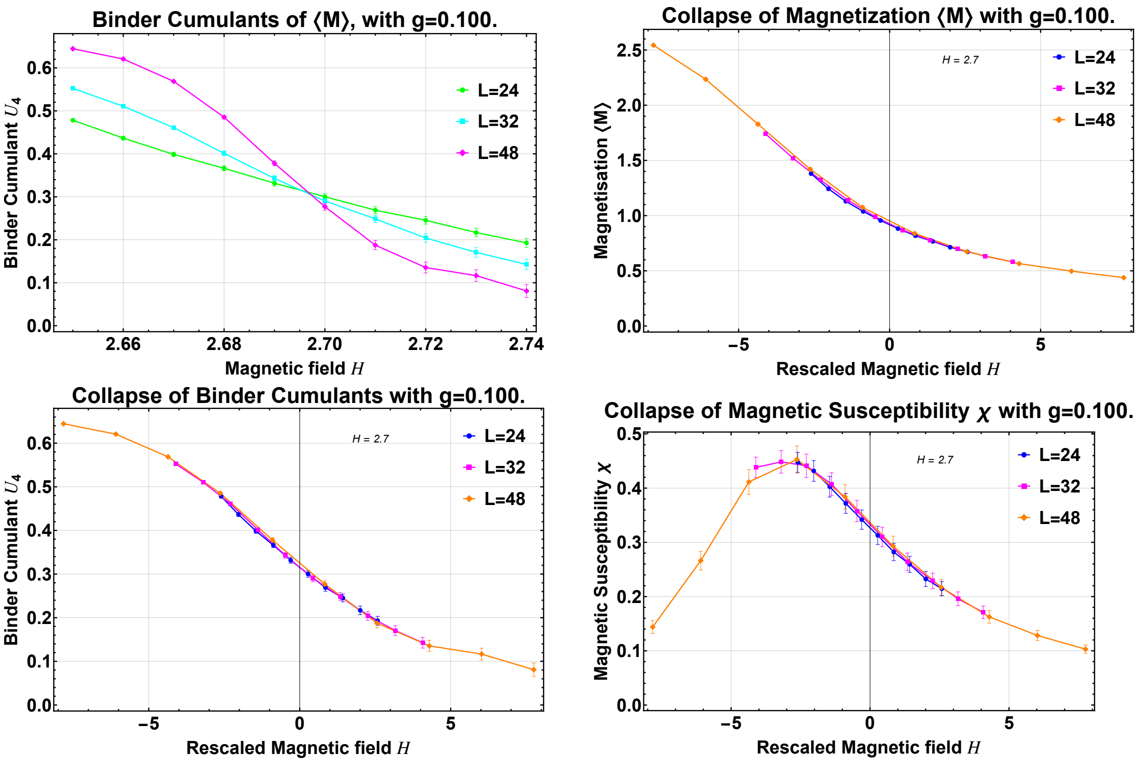

Figure 4.7: Collapse of the Binder cumulant, Magnetisation and Magnetic Susceptibility, respectively, for $g = 0.10$. In all cases, the value of the magnetic field is $h_c \approx 2.7$.

Case $g = 0.20$. Keeping $J_2 = 0.2$ and $\varepsilon = 0.05$, we varied h in the interval $[2.325, 2.350]$, with incremental steps of 0.005. Here the transition occurs at a lower field, $h_c \approx 2.34$, as shown by the consistent collapse in the Binder, magnetization, and susceptibility plots (Fig. 4.8).

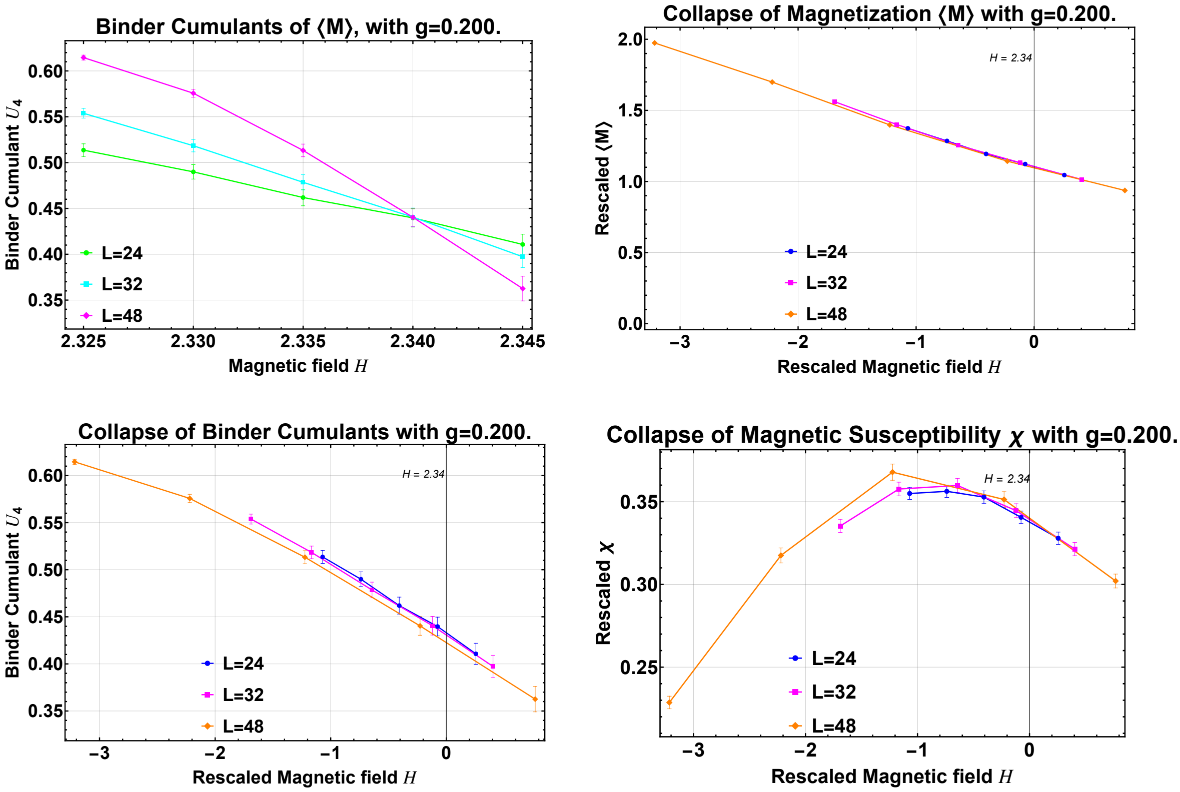

Figure 4.8: Collapse of the Binder cumulant, Magnetisation and Magnetic Susceptibility, respectively, for $g = 0.20$. In all cases, the value of the magnetic field is $h_c \approx 2.34$

Case $g = 0.30$. For $g = 0.3$, we obtain $h_c \approx 1.9$ with similarly robust FSS behavior (Fig. 4.9). In this run, $J_2 = 0.3$ and $\varepsilon = 0.06$, and we varied h in the interval $[1.900, 1.930]$, with incremental steps of 0.003

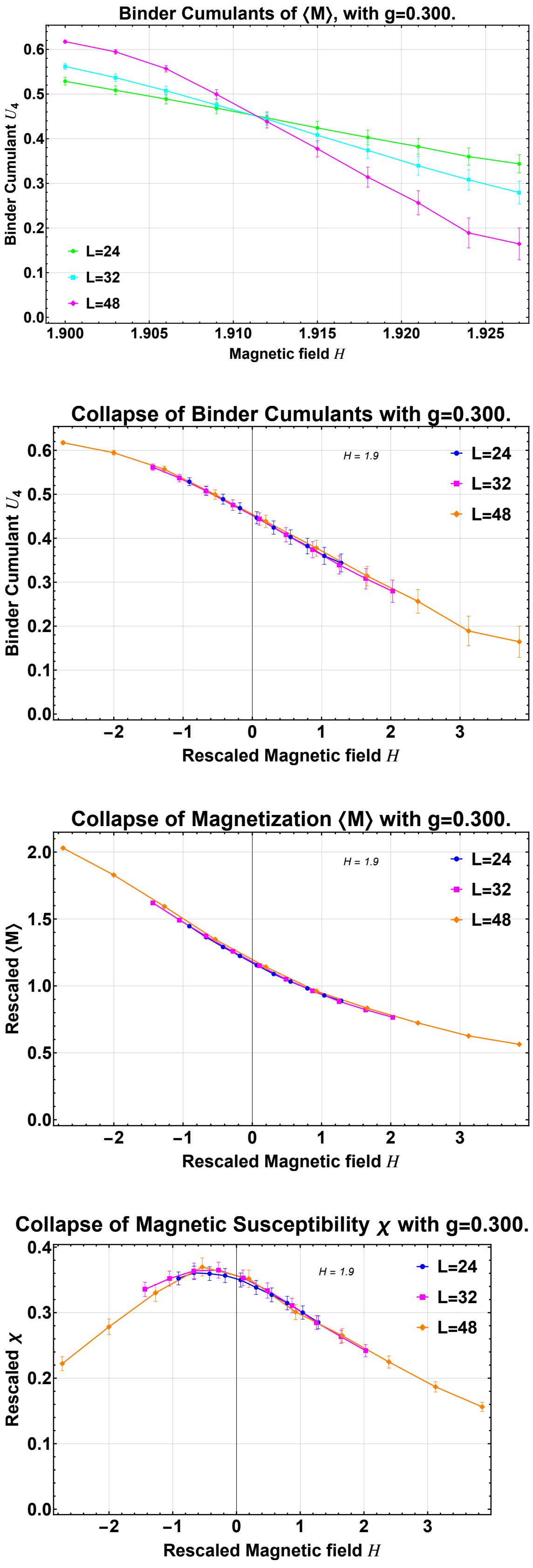

Figure 4.9: Collapse of the Binder cumulant, Magnetisation and Magnetic Susceptibility, respectively, for $g = 0.30$. In all cases, the value of the magnetic field is $h_c \approx 1.9$

Case $g = 0.40$. Choosing $J_2 = 0.4$ and $\varepsilon = 0.06$, and we varied h in the interval $[1.38, 1.40]$, with incremental steps of 0.002. The critical point shifts further to $h_c \approx 1.39$, again with clear evidence of a second-order transition from both Binder crossings and scaling collapses (Fig. 4.10).

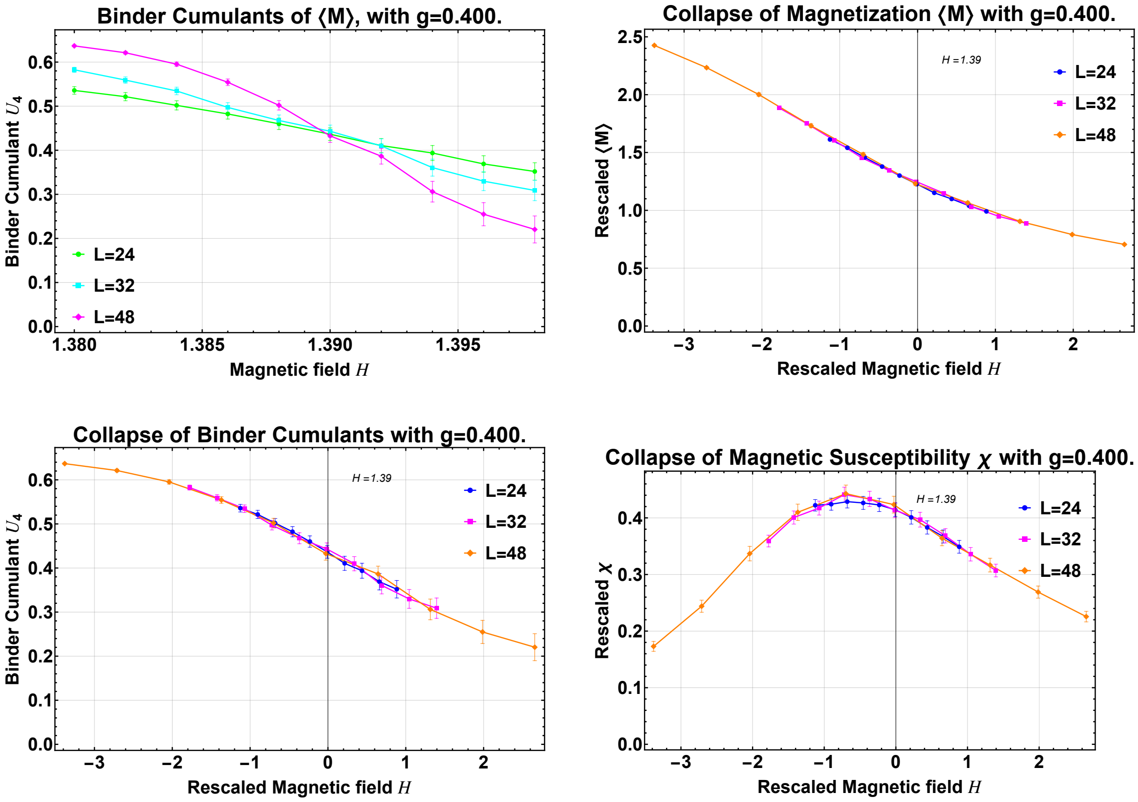

Figure 4.10: Collapse of the Binder cumulant, Magnetisation and Magnetic Susceptibility, respectively, for $g = 0.40$. In all cases, the value of the magnetic field is $h_c \approx 1.39$.

Case $g = 0.49$. Finally, at $g = 0.49$, we identify $h_c \approx 0.85$. Despite the proximity to the degenerate point, the Binder cumulants still exhibit the hallmark crossing of a continuous transition, and FSS analysis confirms consistency with the 3D Ising universality class (Fig. 4.11). In this case, $J_2 = 0.49$ and $\varepsilon = 0.08$, and we varied h in the interval $[0.8, 0.9]$, with incremental steps of 0.01.

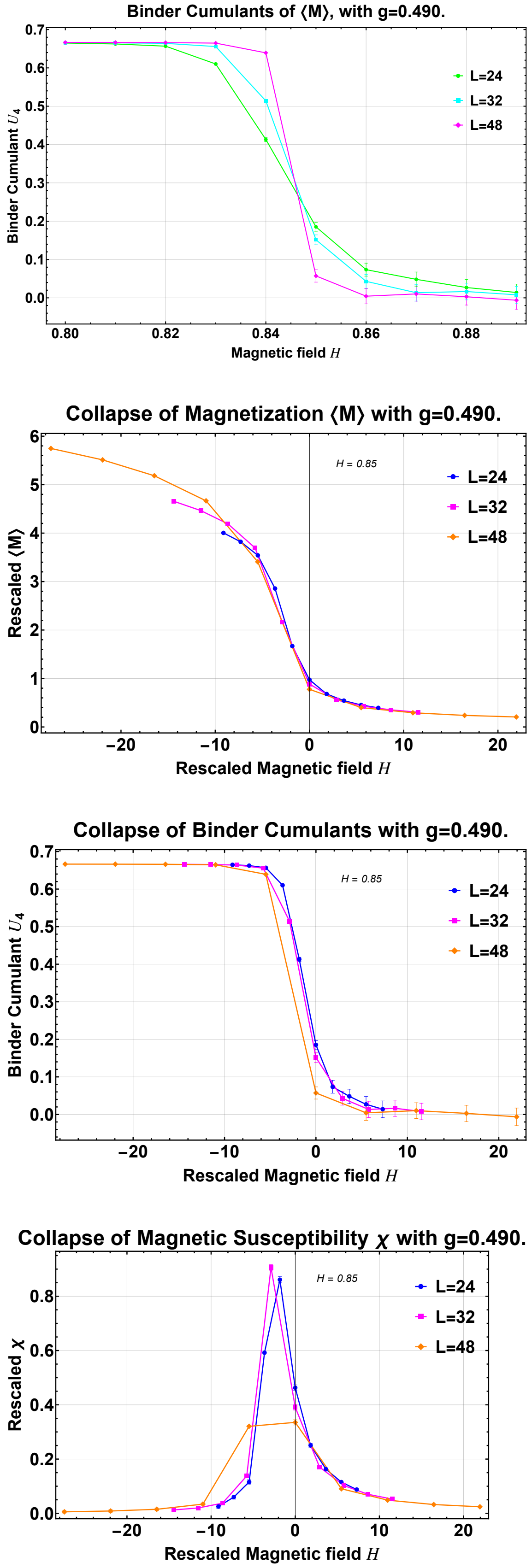

Figure 4.11: Collapse of the Binder cumulant, Magnetisation and Magnetic Susceptibility, respectively, for $g = 0.49$. In all cases, the value of the magnetic field is $h_c \approx 0.85$.

From these results we construct the phase diagram, shown in Fig. 4.12. Each critical point was obtained by finite-size scaling collapse of the magnetic susceptibility using 3D Ising exponents. The phase boundary is smooth, with no indication of a qualitative change in the nature of the transition up to $g = 0.49$.

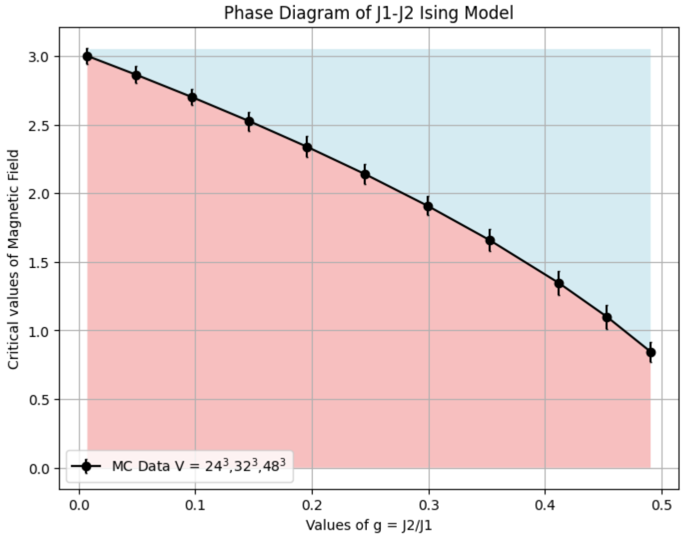

Figure 4.12: Phase diagram of the J_1–J_2 Ising model. The critical magnetic field h_c is plotted as a function of $g = J_2/J_1$.

Taken together, the results up to $g = 0.49$ remain fully consistent with second-order critical behavior. If a change in order were to occur as $g \to 0.5$, it would be expected to manifest through detectable deviations in the Binder crossings or in the FSS trends. Since no such deviations are observed, the data provide reasonable indication that the transition at $g = 0.5$ is also second order. Nonetheless, as extrapolating a second-order line does not strictly guarantee that the endpoint at $g = 0.5$ is itself second order, this conclusion should be interpreted with appropriate caution.

Chapter 5

Conclusion

This thesis revolved around compact scalars, $U(1)$ gauge theories, fracton models and quantum Ising model dualities. We also investigated a new phase transition in which the dual J_1-J_2 Ising model, which was unaccounted for until now.

Our first chapter focused on establishing the fundamental tools used later on. We reviewed a basic discretization of scalar fields, derived the Wilson action for gauge fields, and discussed why the naive discretization introduced earlier fails to preserve gauge invariance. The lattice discretization, combined with the vast number of degrees of freedom in path integrals, suggests that a statistical approach is best suited for computing observables and extracting meaningful information from the system's partition function. Accordingly, we introduced the Monte Carlo method, a set of statistical techniques that relies on sampling a representative subset of all possible system configurations, typically through importance sampling, to estimate relevant physical quantities. This approach, however, introduces certain limitations in data quality, most notably the issue of autocorrelation. Autocorrelation measures the similarity between successive measurements separated by a number of updates in the system's configuration. High autocorrelation implies that more updates are needed to obtain statistically independent samples.

Finite-size scaling analysis is then introduced as a practical method to study finite systems that exhibit signatures of critical phenomena characteristic of infinite systems. At this stage, key observables such as the Binder cumulant and magnetic susceptibility are defined. The Binder cumulant is a dimensionless quantity used to identify phase transitions and estimate critical points. It is constructed from moments of the order parameter and is particularly useful because it becomes independent of system size at the critical temperature, allowing for precise location of critical points via crossing plots. The magnetic susceptibility measures the response of a system's magnetization to an external magnetic field. Near a phase transition, it diverges in the thermodynamic limit, and in finite systems, it exhibits a peak whose height and location can be analyzed through scaling relations to extract critical exponents and critical temperatures.

We also discussed the construction of modified Villain Hamiltonians, which allows models to conserved the correct global symmetries and anomaly structures when written in a lattice formalism with a Villain variable promoted to an operator with an integer spectrum.

We have shown that coupling the compact scalar model in $1+1$ dimensions and the fracton compact scalar model in $2+1$ dimensions to their respective gauge fields (with a $\theta = \pi$ term) and taking the infinite gauge coupling limit yields the quantum Ising model in a transverse field in 1D and 2D, respectively. This is particularly noteworthy for the gauged XY-plaquette model, where its phase structure can be analyzed via the simpler corresponding Ising model.

Once the duality between the fracton-inspired model and the quantum Ising model was established, we leveraged this mapping to analyze the system's critical behavior via standard statistical mechanics techniques. This allowed us to sidestep the complexities inherent to the constrained gauge model by studying a well-understood spin system with known numerical methods. The presence of a phase transition in the dual theory serves as indirect but strong evidence for a similar transition in the original model, providing insight into its non-trivial phase structure. This not only validates the theoretical framework used but also demonstrates the practical power of dualities in extracting meaningful physics from exotic lattice systems.

Finally, we performed Monte Carlo simulations to construct a phase diagram of the J_1-J_2 Ising Model. Using the observables that we defined in the FSS section, we were able to show that such model indeed presents the conjectured phase transition at transition point $g = 0.5$. Such phase transition is actually responsible for lifting the exponential number of degenerates ground states. We were also able to determine the nature of this transition as a 2nd order phase transition, since its behaviour is the same as the system approaches the transition point.

Taken together, the results presented in this thesis illustrate how preserving global symmetries and anomaly structures on the lattice is not only conceptually sound but practically fruitful. The Villain Hamiltonian framework provides a rigorous and flexible toolset for constructing lattice models with exact symmetries, enabling precise theoretical control and access to non-perturbative physics. Moreover, the successful identification of a new phase transition in the dual Ising model emphasizes the utility of duality mappings for understanding complex constrained systems, especially in the context of fracton-like behavior and higher-form gauge theories. These developments open the door for future investigations into lattice models with even richer symmetry and topological structures, as well as their connections to both high-energy and condensed matter physics.

Appendix

A Differential forms and Co-chains notation on a Cubic Lattice

In this section we describe our choice of notation for describing links, plaquettes, cells and their relations on the lattice and the dual lattice, following the convention used in [36]. We consider a d-dimensional lattice Λ and denote the dual lattice as $\tilde{\Lambda}$, with site spacing 1. A site is denoted by x_i where $i = 1, 2, 3, ..., N$, links are denoted with l, and cubes as c, and in general, an r-cell are written $c^{(r)}$, such that if $r = 1$ then $c^{(1)} = x$, $r = 2$ then $c^{(1)} = l$ and so on. We identify the sites, links, and every r-cell periodically, that is, $c^{(r)}_N = c^{(r)}_1$. We define the orientation of a r-cell such that: given $c^{(r)}_1$ and $c^{(r)}_2$ are identical except for their orientation, then $c^{(r)}_1 = -c^{(r)}_2$.

We can also define operators that act on r-cells. The boundary operator $\partial c^{(r)}$ that acts on a r-cell is given by,

$$\partial c^{(r)}(x)_{\mu_1\mu_2\ldots\mu_r} = \sum_{k=1}^{r} (-1)^{r-1} \left[c^{(r-1)}(x+\hat{\mu}_k)_{\mu_1\ldots\overset{\circ}{\mu}_k\ldots\mu_r} - c^{(r-1)}(x)_{\mu_1\ldots\overset{\circ}{\mu}_k\ldots\mu_r} \right]. \tag{A.1}$$

Where $\overset{\circ}{\mu}_k$ means that this index is omitted. We define for sites that $\partial c^{(0)}(x) = \partial x_i = 0$. The co-boundary operator is given as,

$$\begin{aligned} \hat{\partial} c^{(r)}(x)_{\mu_1\mu_2\ldots\mu_r} = \sum_{\nu\neq\mu_1\ldots\mu_r} (-1)^{r+1} \Big[& c^{(r-1)}(x+\hat{\mu}_k)_{\mu_1\ldots\mu_r\nu} \\ & - c^{(r+1)}(x-\hat{\nu})_{\mu_1\ldots\mu_r\nu} \Big]. \end{aligned} \tag{A.2}$$

The boundary operator is seen as the oriented sum of the cell r-cell $c^{(r)}$ in the boundary of $c^{(r)}$, while the co-boundary operator is seen as oriented sum of all $r+1$ cells that contain $c^{(r)}$ in their boundary. We also define the co-boundary operator acting on a 0-cell to be zero, i.e. $\hat{\partial} c^{(0)} = 0$.

Let's comment a few things about the dual lattice $\tilde{\Lambda}$. Its sites lie in the center of the lattice Λ d-cells. Such that $\tilde{x} = x + \frac{1}{2}\left(\hat{1} + \hat{2} + \ldots\ \hat{d}\right)$, and we can construct a transformation between the lattice Λ and $\tilde{\Lambda}$. A transformation between an r-cell $c^{(r)}$

and it's equivalent $\tilde{c}^{(d-r)}$ $(d-r)$-cell on the dual lattice can be described through the $\star$ operator, as follows,

$$\star c^{(r)}(x)_{\mu_1\mu_2\dots\mu_r} = \frac{1}{(d-r)!}\sum_{\mu'_{r+1}\cdots\mu'_d} \epsilon_{\mu_1\dots\mu_r\mu'_{r+1}\dots\mu'_d}\tilde{c}^{(d-r)}\left(\tilde{x}-\hat{\mu}_{r+1}\dots-\hat{\mu}'_d\right)_{\mu'_{r+1}\cdots\mu'_d},$$

and

$$\star\tilde{c}^{(r)}(x)_{\mu_1\mu_2\dots\mu_r} = \frac{1}{(d-r)!}\sum_{\mu'_{r+1}\cdots\mu'_d} \epsilon_{\mu_1\dots\mu_r\mu'_{r+1}\dots\mu'_d}c^{(d-r)}\left(x+\hat{\mu}_{r+1}\dots+\hat{\mu}'_d\right)_{\mu'_{r+1}\cdots\mu'_d}.$$

For even dimensions, $\star^2 c^{(r)} = (-1)^{r(d-r)}c^{(r)}$ and $\star^2\tilde{c}^{(r)} = (-1)^{r(d-r)}\tilde{c}^{(r)}$.

Let's now show some relations between the boundary and co-boundary operator obtained through the $\star$ operator. That is, we have an equivalence between these operator in the sense of

$$\hat{\partial}c^{(r)} = (-1)^{(d-r-1)(r+1)}\star\partial\star c^{(r)}. \tag{A.3}$$

If we take an operator $A_{c^{(r)}}$, we can denote it a r-form operator and define a map from this r-form operator to a $(r+1)$-form operator through a exterior derivative given by,

$$d\left(A\right)_{c^{(r+1)}} = \sum_{c^r\in\partial c^{(r+1)}} A_{c^{(r)}}. \tag{A.4}$$

Similarly, we define the map between a r-form operator to a $(r-1)$-operator through the divergence operator,

$$\delta\left(A\right)_{c^{(r-1)}} = \sum_{c^r\in\hat{\partial}c^{(r-1)}} A_{c^{(r)}}. \tag{A.5}$$

Both the exterior derivative and the divergence operator are nil potent, $d^2 = \delta^2 = 0$.

Either of these operators will satisfy the partial integration rule,

$$\sum_{c^{(r)}}\left(dA\right)_{c^{(r)}}B_{c^{(r)}} = (-1)^{(r)}\sum_{c^{(r-1)}} dA_{c^{(r-1)}}\left(\delta B\right)_{c^{(r-1)}}, \tag{A.6}$$

$$\sum_{c^{(r)}}\left(dA\right)_{c^{(r)}}\tilde{B}_{\star c^{(r)}} = (-1)^{(r)}\sum_{c^{(r-1)}} dA_{c^{(r-1)}}\left(d\tilde{B}\right)_{\star c^{(r-1)}}, \tag{A.7}$$

where in the last formula the fact $d\star = \star\delta$ and $\tilde{B}_{\tilde{c}^{d-r}} = \left(\star B\right)_{c^{(d-r)}}$ were used.

B Solution to the Compact Scalar

In this appendix, we solve the equations of motion for the compact scalar field theory in $(1+1)$ dimensions discretized on a spatial lattice with N sites and lattice spacing a. The system is described by a Hamiltonian (3.2.17), which depends on the scalar field ϕ_x, its canonical momentum π_x, and two sets of integer-valued winding numbers n_x and $\tilde{n}_x$ (to be defined precisely below).

For completeness, the Hamiltonian is given as

$$H = \sum_x \left(\frac{1}{2Ja(2\pi)^2} \left(\tilde{\phi}_x - \tilde{\phi}_{x+1} + 2\pi \tilde{n}_x \right)^2 + \frac{J}{2a} \left(\phi_{x+1} - \phi_x - 2\pi n_x \right)^2 \right), \tag{B.1}$$

The equations of motion derived from the Hamiltonian are:

$$\dot{\phi}_x = i[H, \phi_x] = \frac{\pi_x}{Ja}, \tag{B.2}$$

$$\dot{\pi}_x = i[H, \pi_x] = \frac{J}{a} \left(\phi_{x+1} - 2\phi_x + \phi_{x-1} + 2\pi(n_x - n_{x-1}) \right), \tag{B.3}$$

$$\dot{\tilde{\phi}}_x = i[H, \tilde{\phi}_x] = \frac{2\pi J}{a} \left(\phi_{x+1} - \phi_x + 2\pi n_x \right), \tag{B.4}$$

$$\dot{n}_x = i[H, n_x] = 0, \tag{B.5}$$

$$\dot{\tilde{n}}_x = i[H, \tilde{n}_x] = 0. \tag{B.6}$$

The first two equations combine into a discrete wave equation with a topological winding source:

$$\ddot{\phi}_x = \frac{1}{a^2} \left(\phi_{x+1} - 2\phi_x + \phi_{x-1} + 2\pi(n_x - n_{x-1}) \right). \tag{B.7}$$

We move to momentum space by defining discrete Fourier transforms:

$$\phi_x = \sum_p e^{ipx} a_p, \qquad\qquad n_x = \sum_p e^{ipx} m_p, \tag{B.8}$$

where the allowed momenta are $p = \frac{2\pi k}{N}$ for $k = 0, 1, \ldots, N-1$. The Fourier coefficients satisfy $a_p = a^\dagger_{-p}$ and $m_p = m^\dagger_{-p}$.

The equation of motion for the Fourier mode a_p becomes:

$$\ddot{a}_p + \omega_p^2 a_p = \frac{2\pi}{a^2}(1 - e^{-ip})m_p, \tag{B.9}$$

where the lattice dispersion relation is given by:

$$\omega_p = \frac{2|\sin(p/2)|}{a}, \quad \text{so that} \quad \omega_p^2 = \frac{1}{a^2}(1 - e^{ip})(1 - e^{-ip}). \tag{B.10}$$

Since m_p is time-independent (as $\dot{n}_x = 0$), equation (B.9) can be solved by shifting the inhomogeneous solution and introducing oscillatory modes. Define the oscillator mode $b_p(t)$ (for $p \neq 0$) as:

$$b_p(t) = \sqrt{2aNJ\omega_p}\left(a_p(t) - \frac{1 - e^{-ip}}{\omega_p^2 a^2} 2\pi m_p\right). \tag{B.11}$$

This redefinition leads to a simple harmonic oscillator equation:

$$\ddot{b}_p + \omega_p^2 b_p = 0, \tag{B.12}$$

whose general Hermitian solution is

$$b_p(t) = e^{i\omega_p t} B_p^\dagger + e^{-i\omega_p t} B_{-p}, \tag{B.13}$$

where B_p are time-independent operators. These B_p arise as the mode coefficients in the solution of the harmonic oscillator equation and serve as annihilation operators for the corresponding momentum modes, with $B_p^\dagger$ acting as creation operators. They satisfy the canonical commutation relations

$$[B_p, B_{p'}^\dagger] = \delta_{pp'}, \qquad [B_p, B_{p'}] = 0. \tag{B.14}$$

In this basis, the Hamiltonian becomes diagonal in terms of the $B_p^\dagger B_p$

For $p = 0$, the mode evolves linearly in time:

$$a_0(t) = \Phi + \frac{1}{Ja}\Pi t, \tag{B.15}$$

where Φ and Π are constant operators representing the zero mode of the field ϕ_x and its conjugate momentum, respectively. The operator Π is the conserved charge associated with the global shift symmetry $\phi_x \to \phi_x + \text{const}$, corresponding to the Noether charge of this symmetry. As expected for canonically conjugate variables, they satisfy the commutation relation $[\Phi, \Pi] = i$.

We can now write the field ϕ_x and its conjugate momentum π_x as:

$$\phi_x = \Phi + \frac{1}{Ja}\frac{\Pi t}{N} + \sum_{p\neq 0}\sqrt{\frac{1}{2NaJ\omega_p}}\left(B_p^\dagger e^{i\omega_p t + ipx} + B_p e^{-i\omega_p t - ipx}\right) + \sum_{p\neq 0}\frac{2\pi m_p e^{ipx}}{1-e^{ip}}, \tag{B.16}$$

$$\pi_x = \frac{\Pi}{N} + \sum_{p\neq 0}\sqrt{\frac{J\omega_p}{2Na}}i\left(B_p^\dagger e^{i\omega_p t + ipx} - B_p e^{-i\omega_p t - ipx}\right). \tag{B.17}$$

To satisfy the canonical commutation relations $[\phi_x, \pi_y] = i\delta_{xy}$, we require:

$$[\Phi, \Pi] = i, \qquad [B_p, B_{p'}^\dagger] = \delta_{pp'}, \qquad [B_p, B_{p'}] = 0, \qquad [\Pi, B_p] = 0. \tag{B.18}$$

The expression $\phi_{x+1} - \phi_x + 2\pi n_x$ appears naturally in the dynamics. Evaluating this gives:

$$\begin{aligned}\phi_{x+1} - \phi_x + 2\pi n_x &= \sum_p \left((e^{ip}-1)a_p + 2\pi m_p\right)e^{ipx} \\ &= 2\pi\frac{\tilde{\Pi}}{N} + \sum_{p\neq 0}\sqrt{\frac{1}{2NaJ\omega_p}}\left((e^{ip}-1)B_p^\dagger e^{i\omega_p t + ipx} + (e^{-ip}-1)B_p e^{-i\omega_p t - ipx}\right),\end{aligned} \tag{B.19}$$

where $\tilde{\Pi} = \sum_x n_x$ is a spatial winding number, interpreted as the momentum conjugate to the dual field zero mode $\tilde{\Phi}$. This identification comes from:

$$\tilde{\Pi} = \frac{1}{2\pi}\sum_x \left(\phi_{x+1} - \phi_x + 2\pi n_x\right), \tag{B.20}$$

which is a lattice version of $\tilde{\Pi} = \frac{1}{2\pi}\int dx\, \partial_x \phi$.

The Hamiltonian in terms of the mode expansions becomes:

$$\begin{aligned}H &= \frac{1}{2Ja}\sum_x \pi_x^2 + \frac{J}{2a}\sum_x(\phi_{x+1} - \phi_x + 2\pi n_x)^2 \\ &= \frac{J(2\pi)^2}{2a}\frac{\tilde{\Pi}^2}{N} + \frac{1}{2Ja}\frac{\Pi^2}{N} + \frac{1}{2}\sum_{p\neq 0}\omega_p\left(B_p B_p^\dagger + B_p^\dagger B_p\right).\end{aligned} \tag{B.21}$$

Using the equation $\dot{\tilde{\phi}}_x = \frac{2\pi J}{a}(\phi_{x+1} - \phi_x + 2\pi n_x)$, we find:

$$\pi_x = \frac{1}{2\pi}(\tilde{\phi}_x - \tilde{\phi}_{x-1} + \hat{K}_x), \tag{B.22}$$

where $\hat{K}_x$ is a constant operator. Imposing the compactness constraint implies $\hat{K}_x = 2\pi\tilde{n}_x$, with $\tilde{n}_x \in \mathbb{Z}$. Define the dual field mode expansion:

$$\tilde{\phi}_x = \sum_p \tilde{a}_p e^{ipx}, \qquad \tilde{n}_x = \sum_p \tilde{m}_p e^{ipx}. \tag{B.23}$$

Then,

$$\tilde{\phi}_x - \tilde{\phi}_{x-1} + 2\pi\tilde{n}_x = 2\pi\tilde{m}_0 + 2\pi\sqrt{J}\sum_{p\neq 0}\frac{1-e^{-ip}}{\sqrt{2Na\omega_p}}\tilde{b}_p e^{ipx}, \tag{B.24}$$

with

$$\tilde{b}_p = \frac{2\pi\sqrt{J}}{\sqrt{2Na\omega_p}}\left(\tilde{a}_p + \frac{2\pi\tilde{m}_p}{1-e^{-ip}}\right). \tag{B.25}$$

From the equation $\pi_x = aJ\dot{\phi}_x$, and matching with the above expansion, we identify:

$$\tilde{m}_0 = \frac{\Pi}{N}, \qquad \tilde{b}_p = \frac{1}{1-e^{-ip}}\dot{b}_p. \tag{B.26}$$

Hence, $\tilde{b}_p$ also satisfies:

$$\ddot{\tilde{b}}_p = -\omega_p^2 \tilde{b}_p, \tag{B.27}$$

and has the solution:

$$\tilde{b}_p(t) = \tilde{B}_p e^{-i\omega_p t} + \tilde{B}_{-p}^\dagger e^{i\omega_p t}, \tag{B.28}$$

with

$$\tilde{B}_p = \frac{-i\omega_p}{1-e^{ip}}B_p, \qquad [\tilde{B}_p, \tilde{B}_{p'}^\dagger] = \delta_{pp'}. \tag{B.29}$$

To complete the quantization, we show that the zero mode $\tilde{a}_0$ evolves as:

$$\dot{\tilde{a}}_0 = \frac{(2\pi)^2}{JN}\tilde{\Pi}, \tag{B.30}$$

which integrates to:

$$\tilde{a}_0(t) = \tilde{\Phi} + \frac{(2\pi)^2}{JN}\tilde{\Pi}t. \tag{B.31}$$

Moreover, $\tilde{\Phi}$ is canonically conjugate to the winding number operator $\tilde{\Pi}$:

$$[\tilde{a}_0, \tilde{\Pi}] = \frac{1}{N} \sum_{x,y} [\tilde{\phi}_x, n_y] = i. \tag{B.32}$$

This confirms that $\tilde{\Pi}$ is the dual momentum to the zero mode $\tilde{\Phi}$ of the dual field $\tilde{\phi}_x$.

B.1 Solution of the 2+1d XY-plaquette compact scalar fracton model

We now analyze the Hamiltonian in Eq. (**??**). The equations of motion take the form

$$\dot{\phi}_x = i[H, \phi_x] = \frac{1}{aJ}\pi_x \ , \tag{B.33}$$

$$\dot{\pi}_x = i[H, \pi_x] = -\frac{J}{a}\left(\Delta_1^2\Delta_2^2\phi_{x-\hat{1}-\hat{2}} + 2\pi\,\Delta_1\Delta_2 n_{x-\hat{1}-\hat{2}}\right) \ , \tag{B.34}$$

$$\dot{\varphi}_x = i[H, \varphi_x] = -\frac{2\pi J}{a}\left(\Delta_1\Delta_2\phi_x + 2\pi n_x\right) \ , \tag{B.35}$$

$$\dot{n}_x = 0 \ . \tag{B.36}$$

Following the same strategy used for the 2d compact scalar, we expand the fields in Fourier modes:

$$\phi_x = \sum_p a_p e^{ix\cdot p} \ , \tag{B.37}$$

$$n_x = \sum_p q_p e^{ix\cdot p} \ . \tag{B.38}$$

Combining the equations for $\dot{\phi}_x$ and $\dot{\pi}_x$ yields

$$\ddot{\phi}_x + \frac{1}{a^2}\left(\Delta_1^2\Delta_2^2\phi_{x-\hat{1}-\hat{2}} + 2\pi\,\Delta_1\Delta_2 n_{x-\hat{1}-\hat{2}}\right) = 0 \ , \tag{B.39}$$

from which we obtain the mode equation

$$\ddot{a}_p + \omega_p^2 a_p = -\frac{2\pi q_p}{a^2}(1-e^{-ip_1})(1-e^{-ip_2}) \ , \tag{B.40}$$

where

$$\omega_p = \frac{4}{a}\left|\sin\frac{p_1}{2}\right|\left|\sin\frac{p_2}{2}\right| \ .$$

For modes with $p_1 \neq 0$ and $p_2 \neq 0$, it is convenient to define

$$b_p = c_p\left(a_p + \frac{2\pi}{(1-e^{ip_1})(1-e^{ip_2})}q_p\right) \ , \tag{B.41}$$

where c_p are constants. The new variables satisfy

$$\ddot{b}_p + \omega_p^2 b_p = 0 \,, \tag{B.42}$$

whose general solution is

$$b_p = B_p^\dagger e^{i\omega_p t} + B_{-p} e^{-i\omega_p t} \,. \tag{B.43}$$

When either $p_1 = 0$ or $p_2 = 0$, the equation of motion for ϕ_x depends only on x_1 or only on x_2, respectively. In such cases, the solution takes the form

$$\begin{aligned}
\phi_x &= \Phi_0 + \Phi_1(x_1) + \Phi_2(x_2) + \frac{-\Pi_0/(N_1 N_2) + \Pi_1(x_1)/N_2 + \Pi_2(x_2)/N_1}{aJ} t \\
&\quad + \sum_{\substack{p_1 \neq 0 \\ p_2 \neq 0}} \frac{1}{c_p} \left(B_p^\dagger e^{i\omega_p t + ix\cdot p} + B_p e^{-i\omega_p t - ix\cdot p} \right) \\
&\quad - \sum_{\substack{p_1 \neq 0 \\ p_2 \neq 0}} \frac{2\pi e^{ix\cdot p}}{(1-e^{ip_1})(1-e^{ip_2})} q_p \,, \qquad \text{(B.44)} \\
\pi_x &= \frac{-\Pi_0}{N_1 N_2} + \frac{\Pi_1(x_1)}{N_2} + \frac{\Pi_2(x_2)}{N_1} \\
&\quad + \sum_{\substack{p_1 \neq 0 \\ p_2 \neq 0}} \frac{J a \omega_p i}{c_p} \left(B_p^\dagger e^{i\omega_p t + ix\cdot p} - B_p e^{-i\omega_p t - ix\cdot p} \right) \,. \qquad \text{(B.45)}
\end{aligned}$$

The zero-mode sector is parametrized by three contributions: one constant term, one depending solely on x_1, and one depending solely on x_2. This decomposition is not unique—since the constant part can be absorbed into the x_1- or x_2-dependent terms—but keeping all three will be convenient for later manipulations.

Imposing the canonical commutation relations $[\phi_x, \pi_y] = i\delta_{x,y}$ leads to

$$[\Phi_1(x_1), \Pi_1(y_1)] = i\,\delta_{x_1,y_1} \,, \quad [\Phi_2(x_2), \Pi_2(y_2)] = i\,\delta_{x_2,y_2} \,, \tag{B.46}$$

$$[\Phi_0, \Pi_0] = i \,, \quad [B_p, B_{p'}^\dagger] = \frac{c_p^2}{2 N_1 N_2 a J \omega_p}\, \delta_{p,p'} \,, \tag{B.47}$$

with all remaining commutators vanishing. Choosing $c_p = \sqrt{2 N_1 N_2 J a \omega_p}$ simplifies the last expression to $[B_p, B_{p'}^\dagger] = \delta_{p,p'}$.

The decomposition (Φ_0, Φ_1, Φ_2) is subject to the redundancy

$$\Phi_0 \to \Phi_0 + \delta \ , \quad \Phi_1 \to \Phi_1 + \delta_1 \ , \quad \Phi_2 \to \Phi_2 + \delta_2 \ , \tag{B.48}$$

with $\delta + \delta_1 + \delta_2 = 0$, implying the constraint

$$\sum_{x_1} \Pi_1(x_1) = \sum_{x_2} \Pi_2(x_2) = \Pi_0 \ . \tag{B.49}$$

Similarly, the shifts

$$\Pi_0 \to \Pi_0 + N_1 N_2 \Lambda \ , \quad \Phi_1 \to \Phi_1 + N_2 \Lambda_1 \ , \quad \Phi_2 \to \Phi_2 + N_1 \Lambda_2 \ , \tag{B.50}$$

with $-\Lambda + \Lambda_1 + \Lambda_2 = 0$ enforce

$$N_2 \sum_{x_1} \Phi_1(x_1) = N_1 \sum_{x_2} \Phi_2(x_2) = -N_1 N_2 \Phi_0 \ . \tag{B.51}$$

The lattice double derivative is then

$$\begin{aligned}\Delta_1 \Delta_2 \phi_x = \sum_{\substack{p_1 \neq 0 \\ p_2 \neq 0}} \frac{1}{\sqrt{2 N_1 N_2 J a \omega_p}} \Big[&(e^{ip_1} - 1)(e^{ip_2} - 1) B_p e^{ip\cdot x + i\omega_p t} \\ &+ (e^{-ip_1} - 1)(e^{-ip_2} - 1) B_p^\dagger e^{-ip\cdot x - i\omega_p t} \Big] - 2\pi \sum_{\substack{p_1 \neq 0 \\ p_2 \neq 0}} e^{ix\cdot p} q_p \ . \end{aligned} \tag{B.52}$$

Using

$$\sum_{\substack{p_1 \neq 0 \\ p_2 \neq 0}} q_p e^{ix\cdot p} = n_x - \frac{1}{N_1} \sum_{x_1} n_x - \frac{1}{N_2} \sum_{x_2} n_x + \frac{1}{N_1 N_2} \sum_x n_x \ , \tag{B.53}$$

the Hamiltonian becomes

$$\begin{aligned} H = \frac{1}{2 J a N_1^2 N_2^2} \sum_x \Big(\Pi_0 - N_1 \Pi_1(x_1) - N_2 \Pi_2(x_2) \Big)^2 \\ + \frac{J}{2 a N_1^2 N_2^2} \sum_x \Big(\tilde{\Pi}_0 - N_1 \tilde{\Pi}_1(x_1) - N_2 \tilde{\Pi}_2(x_2) \Big)^2 \\ + \sum_p \omega_p \left(B_p^\dagger B_p + \frac{1}{2} \right) \ . \end{aligned} \tag{B.54}$$

Diagonalizing Π_0, $\Pi_{1,2}(x_{1,2})$ (and their tilded versions) together with the number operators $B_p^\dagger B_p$ yields the full spectrum.

Finally, the model exhibits a tensor symmetry. The associated currents are

$$J_{0,x} = \pi_x \ , \quad J_x^{12} = -\frac{J}{a}\left(\Delta_1\Delta_2\phi_{x-\hat{1}-\hat{2}} + 2\pi n_{x-\hat{1}-\hat{2}}\right) \ , \tag{B.55}$$

and satisfy

$$\partial_0 J_x^0 - \Delta_1\Delta_2 J_x^{12} = 0 \tag{B.56}$$

by virtue of the equations of motion. The conserved charges are

$$Q_1(x_1) = \sum_{x_2} J_{0,x} \ , \tag{B.57}$$

$$Q_2(x_2) = \sum_{x_1} J_{0,x} \ , \tag{B.58}$$

and using Eq. (B.45) together with $\sum_{x_i} \Pi_i(x_i) = \Pi_0$ shows that $\sum_{x_i} J_{0,x} = \Pi_i(x_i)$, confirming their conservation.

Bibliography

[1] H. B. Nielsen and M. Ninomiya. ‘A no-go theorem for regularizing chiral fermions’. *Physics Letters B* 105.2–3 (Oct. 1981), pp. 219–223.

[2] David B. Kaplana. ‘Recent developments in lattice supersymmetry’. *Nuclear Physics B - Proceedings Supplements* 129–130 (Mar. 2004), pp. 109–120.

[3] Heinz J. Rothe. *Lattice Gauge Theories: An Introduction.* World Scientific, Nov. 2011.

[4] Kenneth G. Wilson. ‘Confinement of quarks’. *Physical Review D* 10.8 (Oct. 1974), pp. 2445–2459.

[5] Nicholas Metropolis and S. Ulam. ‘The Monte Carlo Method’. *J. Am. Statist. Assoc.* 44.247 (1949), pp. 335–341.

[6] Nicholas Metropolis, Arianna W. Rosenbluth, Marshall N. Rosenbluth, Augusta H. Teller and Edward Teller. ‘Equation of State Calculations by Fast Computing Machines’. *The Journal of Chemical Physics* 21.6 (June 1953), pp. 1087–1092.

[7] W. K. Hastings. ‘Monte Carlo Sampling Methods Using Markov Chains and Their Applications’. *Biometrika* 57.1 (1970), pp. 97–109.

[8] N. V. Prokof’ev, B. V. Svistunov and I. S. Tupitsyn. ‘“Worm” algorithm in quantum Monte Carlo simulations’. *Physics Letters A* 238.4–5 (Feb. 1998), pp. 253–257.

[9] Michael Creutz. ‘Microcanonical Monte Carlo Simulation’. *Physical Review Letters* 50.19 (May 1983), pp. 1411–1414.

[10] Naoki Kawashima and Kenji Harada. *Recent developments of world-line Monte Carlo methods*. June 2004. [cond-mat/0312675].

[11] N. Kawashima and J. E. Gubernatis. 'Loop Algorithms for Monte Carlo Simulations of Quantum Spin Systems'. *Phys. Rev. Lett.* 73 (9 Aug. 1994), pp. 1295–1298.

[12] H. G. Evertz. 'The Loop algorithm'. *Adv. Phys.* 52 (2003), p. 1. [cond-mat/9707221].

[13] M. Suzuki. *Quantum Monte Carlo Methods in Condensed Matter Physics.* World Scientific, Dec. 1993.

[14] Don Lemons. *An Introduction to Stochastic Processes in Physics.* Johns Hopkins University Press, 2003.

[15] Ulli Wolff. 'Monte Carlo errors with less errors'. *Computer Physics Communications* 156.2 (Jan. 2004), pp. 143–153. [hep-lat/0306017].

[16] Ulli Wolff. 'Collective Monte Carlo Updating for Spin Systems'. *Phys. Rev. Lett.* 62 (4 Jan. 1989), pp. 361–364.

[17] Robert H. Swendsen and Jian-Sheng Wang. 'Nonuniversal critical dynamics in Monte Carlo simulations'. *Phys. Rev. Lett.* 58 (2 Jan. 1987), pp. 86–88.

[18] H. Eugene Stanley. *Introduction to phase transitions and critical phenomena.* en. International Series of Monographs on Physics. New York, NY: Oxford University Press, July 1987.

[19] J. J. Binney, N. J. Dowrick, A. J. Fisher and M. E. J. Newman. *The theory of critical phenomena.* en. Oxford, England: Clarendon Press, June 1992.

[20] J. M. Yeomans. *Statistical mechanics of phase transitions.* en. Oxford, England: Clarendon Press, May 1992.

[21] V. L. Berezinsky. 'Destruction of long range order in one-dimensional and two-dimensional systems having a continuous symmetry group. I. Classical systems'. *Sov. Phys. JETP* 32 (1971), pp. 493–500.

[22] J. M. Kosterlitz and D. J. Thouless. ‘Ordering, metastability and phase transitions in two-dimensional systems’. *Journal of Physics C: Solid State Physics* 6.7 (Apr. 1973), pp. 1181–1203.

[23] Kenneth G. Wilson. ‘The renormalization group: Critical phenomena and the Kondo problem’. *Reviews of Modern Physics* 47.4 (Oct. 1975), pp. 773–840.

[24] John Cardy. *Scaling and Renormalization in Statistical Physics*. Cambridge University Press, Apr. 1996.

[25] Kerson Huang. *Statistical Mechanics*. en. 2nd ed. Nashville, TN: John Wiley & Sons, Apr. 1987.

[26] V. Privman. *Finite Size Scaling and Numerical Simulation of Statistical Systems*. World Scientific, Jan. 1990.

[27] K. Binder. ‘Finite size scaling analysis of ising model block distribution functions’. en. *Z. Physik B - Condensed Matter* 43.2 (June 1981), pp. 119–140.

[28] David P. Landau and Kurt Binder. *A Guide to Monte Carlo Simulations in Statistical Physics*. Cambridge University Press, Sept. 2005.

[29] M. E. J. Newman and G. T. Barkema. *Monte Carlo methods in statistical physics*. en. Oxford, England: Clarendon Press, Dec. 1998.

[30] K. Binder. ‘Theory of first-order phase transitions’. *Reports on Progress in Physics* 50.7 (July 1987), pp. 783–859.

[31] M. S. Challa, D. P. Landau and K. Binder. ‘Finite-size effects at temperature-driven first-order transitions’. en. *Phys. Rev. B Condens. Matter* 34.3 (Aug. 1986), pp. 1841–1852.

[32] Kurt Binder and Dieter W. Heermann. *Monte Carlo Simulation in Statistical Physics: An Introduction*. Springer Berlin Heidelberg, 2010.

[33] Alexander M. Polyakov. *Gauge Fields and Strings*. Vol. 3. 1987.

[34] Jorge V. José, Leo P. Kadanoff, Scott Kirkpatrick and David R. Nelson. ‘Renormalization, vortices, and symmetry-breaking perturbations in the two-dimensional planar model’. *Physical Review B* 16.3 (Aug. 1977), pp. 1217–1241.

[35] J. Villain. ‘Theory of one-dimensional and two-dimensional magnets with an easy magnetization plane. 2. The Planar, classical, two-dimensional magnet’. *J. Phys. (France)* 36 (1975), pp. 581–590.

[36] Tin Sulejmanpasic and Christof Gattringer. ‘Abelian gauge theories on the lattice: θ-Terms and compact gauge theory with(out) monopoles’. *Nucl. Phys. B* 943 (2019), p. 114616. [1901.02637].

[37] Daniel Göschl, Christof Gattringer and Tin Sulejmanpasic. ‘The critical endpoint in the 2-d U(1) gauge-Higgs model at topological angle $\theta = \pi$’. *PoS* LATTICE2018 (2018), p. 226. [1810.09671].

[38] Nathan Seiberg and Shu-Heng Shao. ‘Exotic $U(1)$ symmetries, duality, and fractons in 3+1-dimensional quantum field theory’. *SciPost Phys.* 9 (2020), p. 046. [2004.00015].

[39] David J. Gross and Igor Klebanov. ‘One-dimensional string theory on a circle’. *Nuclear Physics B* 344.3 (Nov. 1990), pp. 475–498.

[40] Davide Gaiotto, Anton Kapustin, Nathan Seiberg and Brian Willett. ‘Generalized Global Symmetries’. *JHEP* 02 (2015), p. 172. [1412.5148].

[41] Lucca Fazza and Tin Sulejmanpasic. ‘Lattice Quantum Villain Hamiltonians: Compact scalars, $U(1)$ gauge theories, fracton models and Quantum Ising model dualities’ (Nov. 2022). [2211.13047].

[42] Mariia Anosova, Christof Gattringer, Nabil Iqbal and Tin Sulejmanpasic. ‘Phase structure of self-dual lattice gauge theories in 4d’. *JHEP* 06 (2022), p. 149. [2203.14774].

[43] Arun Paramekanti, Leon Balents and Matthew P. A. Fisher. ‘Ring exchange, the exciton Bose liquid, and bosonization in two dimensions’. *Phys. Rev. B* 66 (5 Aug. 2002), p. 054526.

[44] Nathan Seiberg and Shu-Heng Shao. ‘Exotic $\mathbb{Z}_N$ symmetries, duality, and fractons in 3+1-dimensional quantum field theory’. *SciPost Phys.* 10 (2021), p. 003. [2004.06115].

[45] Pranay Gorantla, Ho Tat Lam, Nathan Seiberg and Shu-Heng Shao. ‘A modified Villain formulation of fractons and other exotic theories’. *Journal of Mathematical Physics* 62.10 (Oct. 2021), p. 102301. [2103.01257].

[46] Fiona J. Burnell, Trithep Devakul, Pranay Gorantla, Ho Tat Lam and Shu-Heng Shao. ‘Anomaly inflow for subsystem symmetries’. *Physical Review B* 106.8 (Aug. 2022). [2110.09529].

[47] Pranay Gorantla, Ho Tat Lam, Nathan Seiberg and Shu-Heng Shao. ‘More exotic field theories in 3+1 dimensions’. *SciPost Phys.* 9 (2020), p. 073. [2007.04904].

[48] Pranay Gorantla, Ho Tat Lam, Nathan Seiberg and Shu-Heng Shao. ‘fcc lattice, checkerboards, fractons, and quantum field theory’. *Physical Review B* 103.20 (May 2021).

[49] Pranay Gorantla, Ho Tat Lam, Nathan Seiberg and Shu-Heng Shao. ‘Low-energy limit of some exotic lattice theories and UV/IR mixing’. *Physical Review B* 104.23 (Dec. 2021). [2108.00020].

[50] Pranay Gorantla, Ho Tat Lam, Nathan Seiberg and Shu-Heng Shao. ‘Global dipole symmetry, compact Lifshitz theory, tensor gauge theory, and fractons’. *Physical Review B* 106.4 (July 2022). [2201.10589].

[51] Pranay Gorantla, Ho Tat Lam, Nathan Seiberg and Shu-Heng Shao. ‘2+1d Compact Lifshitz Theory, Tensor Gauge Theory, and Fractons’ (2022). [2209.10030].

[52] Jacques Distler, Andreas Karch and Amir Raz. ‘Spontaneously broken subsystem symmetries’. *Journal of High Energy Physics* 2022.3 (Mar. 2022). [2110.12611].

[53] Han Ma and Michael Pretko. ‘Higher-rank deconfined quantum criticality at the Lifshitz transition and the exciton Bose condensate’. *Physical Review B* 98.12 (Sept. 2018). [1803.04980].

[54] Paul Dirac. *Lectures on Quantum Mechanics*. Dover Books on Physics. Mineola, NY: Dover Publications, Mar. 2001.

[55] Vinay Ambegaokar and Matthias Troyer. ‘Estimating errors reliably in Monte Carlo simulations of the Ehrenfest model’. *Am. J. Phys.* 78 (2010), pp. 150–157. [0906.0943].

[56] Bradley Efron. *The jackknife, the bootstrap and other resampling plans*. Society for Industrial and Applied Mathematics, Jan. 1982.

[57] A. F. Sonsin, M. R. Cortes, D. R. Nunes, J. V. Gomes and R. S. Costa. ‘Computational Analysis of 3D Ising Model Using Metropolis Algorithms’. *J. Phys. Conf. Ser.* 630.1 (2015), p. 012057.

[58] A. F. Sonsin, M. R. Cortes, D. R. Nunes, J. V. Gomes and R. S. Costa. ‘Computational Analysis of 3D Ising Model Using Metropolis Algorithms’. *Journal of Physics: Conference Series* 630.1 (July 2015), p. 012057.

[59] Cyuan-Han Chang, Vasiliy Dommes, Rajeev S. Erramilli, Alexandre Homrich, Petr Kravchuk, Aike Liu, Matthew S. Mitchell, David Poland and David Simmons-Duffin. ‘Bootstrapping the 3d Ising stress tensor’. *JHEP* 03 (2025), p. 136. [2411.15300].